Title of Grant / Cooperative Agreement:	The Fusion Driven Rocket: Nuclear Propulsion through Direct Conversion of Fusion Energy
Type of Report:	Summary of Research
Name of Principal Investigator:	John Slough
Period Covered by Report:	9/10/2012 - 3/10/2015
Name and Address of recipient's institution:	8551 154th Avenue NE, Redmond, WA 98052
NASA Grant / Cooperative Agreement Number:	NNX12AQ61G

Reference 14 CFR § 1260.28 Patent Rights *(abbreviated below)*
The Recipient shall include a list of any Subject Inventions required to be disclosed during the preceding year in the performance report, technical report, or renewal proposal. A complete list (or a negative statement) for the entire award period shall be included in the summary of research.

Subject inventions include any new process, machine, manufacture, or composition of matter, including software, and improvements to, or new applications of, existing processes, machines, manufactures, and compositions of matter, including software.

Have any Subject Inventions / New Technology Items resulted from work performed under this Grant / Cooperative Agreement?	No ◯	Yes ◯
If yes a complete listing should be provided here: Details can be provided in the body of the Summary of Research report.		

Reference 14 CFR § 1260.27 Equipment and Other Property (abbreviated below)
A Final Inventory Report of Federally Owned Property, including equipment where title was taken by the Government, will be submitted by the Recipient no later than 60 days after the expiration date of the grant. Negative responses for Final Inventory Reports are required.

Is there any Federally Owned Property, either Government Furnished or Grantee Acquired, in the custody of the Recipient?	No ◯	Yes ◯
If yes please attach a complete listing including information as set forth at § 1260.134(f)(1).		

Attach the Summary of Research text behind this cover sheet.

Reference 14 CFR § 1260.22 Technical publications and reports (December 2003)
Reports shall be in the English language, informal in nature, and ordinarily not exceed three pages (not counting bibliographies, abstracts, and lists of other media).

A Summary of Research (or Educational Activity Report in the case of Education Grants) is due within 90 days after the expiration date of the grant, regardless of whether or not support is continued under another grant. This report shall be a comprehensive summary of significant accomplishments during the duration of the grant.

Summary:

The future of manned space exploration and development of space depends critically on the creation of a dramatically more efficient propulsion architecture for in-space transportation. A very persuasive reason for investigating the applicability of nuclear power in rockets is the vast energy density gain of nuclear fuel when compared to chemical combustion energy. The Fusion Driven rocket (FDR) represents a revolutionary approach to fusion propulsion where the power source releases its energy directly into the propellant, not requiring conversion to electricity. It employs a solid lithium propellant that requires no significant tankage mass. The propellant is rapidly heated and accelerated to high exhaust velocity (> 30 km/s), while having no substantial physical interaction with the spacecraft thereby avoiding damage to the rocket and limiting both the thermal heat load and radiator mass.

The key to achieving this stems from research at MSNW and the UW on the magnetically driven implosion of metal foils onto a magnetized plasma target to obtain fusion conditions. A logical extension of this work leads to a method that utilizes these metal shells (or liners) to not only achieve fusion conditions, but to serve as the propellant as well. Several low-mass, magnetically-driven metal liners are inductively driven to converge radially and axially and form a thick blanket surrounding the target plasmoid and compress the plasmoid to fusion conditions. Virtually all of the radiant, neutron and particle energy from the plasma is absorbed by the encapsulating, thick metal blanket thereby isolating the spacecraft from the fusion. This energy, in addition to the intense Ohmic heating at peak magnetic field compression, is adequate to vaporize and ionize the metal blanket. The expansion of this hot, ionized metal propellant through a magnetically insulated nozzle produces high thrust at the optimal Isp. The energy from the fusion process, along with the waste heat, is thus utilized at very high efficiency.

The basic scheme for FDR is illustrated and described in the report (see Fig. 2) The two most critical issues in meeting challenges introduced employing magneto-inertial fusion as the power source is driver efficiency and “stand-off” – the ability to isolate and protect fusion and thruster from the resultant fusion energy. By employing metal shells for compression, it is possible to produce the desired convergent motion inductively by inserting the metal sheets along the inner surface of cylindrical or conically tapered coils. Both stand-off and energy efficiency issues are solved by this arrangement.

This two year effort focused on achieving three key criteria for the Fusion Driven Rocket to move forward for technological development: (1) the physics of the FDR must be fully understood and validated, (2) the design and technology development for the FDR required for its implementation in space must be fully characterized, and (3) an in-depth analysis of the rocket design and spacecraft integration as well as mission architectures enabled by the FDR need to be performed. A subscale, laboratory liner compression test facility was assembled at the University of Washington Plasma Dynamics Laboratory with sufficient liner kinetic energy (~ 0.5 MJ) to reach conditions required for fusion breakeven conditions. Detailed experimental studies of the dynamic behavior of the driven liners as well as liner convergence and magnetic compression were performed. The development of both the 1D liner dynamics code and the full 3D ANSYS® liner calculations was achieved. The characterization of both the FDR and spacecraft as well as a design architecture analysis was conducted that included an examination of a wide range of mission architectures and destinations for which this fusion propulsion system would be enabling or critical. In particular a rapid, single launch manned Mars mission was developed.

Nomenclature

A = cross sectional area of liner

A_s = surface area of liner

β = ratio of plasma pressure to magnetic pressure

B = magnetic field

B_e = external magnetic field

B_{in} = internal magnetic field

B_0 = internal field at peak compression

C = capacitance

δ = liner thickness

δ_{gap} = initial gap between driver coil and liner

ε = FRC elongation ratio ($l_s/2r_s$)

E_B = magnetic field energy

E_{fus} = fusion energy

E_L = liner kinetic energy

F = force on liner

FRC = *field reversed configuration*

G_{Al} = action constant for aluminum

g_M = action constant for material m

G = fusion gain

I = current

Isp = specific Impulse

L = inductance

L_{gap} = inductance of coil-liner gap

l_0 = FRC length at peak compression

l_s = FRC length

M_L = liner mass

n_0 = plasma density at peak compression

μ_0 = free space permeability

P_B = magnetic pressure

ρ_m = density of material m

r = radius variable

r_c = coil radius

r_0 = liner radius at peak compression

r_s = FRC separatrix radius

R = object radius

r_L = liner radius

Δr = liner radial displacement from magnetic force

$\langle \sigma v \rangle$ = D-T fusion cross section

dt = time step

T_e = electron temperature in eV

T_i = ion temperature in eV

T_0 = plasma total temperature at peak compression

τ_D = liner dwell time

v_L = liner velocity

v_{max} = maximum liner velocity

V_C = initial voltage on capacitors

w = liner width

I. Introduction

The future of manned space exploration and development of space depends critically on the creation of a dramatically more efficient propulsion system for in-space transportation. This has been recognized for many years. Not as well recognized is the need for high power, high Isp propulsion in Low Earth Orbit (LEO) as it relates to several unmanned orbital maneuvers that are quite costly or not feasible with current chemical propulsion rockets. Of particular value to both military and commercial interests would be a high power orbital tug that can shuttle numerous payloads of several metric tons (MT) from LEO to GEO.

A very persuasive reason for investigating the applicability of nuclear power for these missions is the vast energy density gain of nuclear fuel when compared to chemical combustion energy. The combustion of hydrogen and oxygen has an energy release of 13 MJ/kg, whereas the fission of ^{235}U yields approximately 8×10^7 MJ/kg and the fusion of deuterium and tritium has a 3.6×10^8 MJ/kg yield. So far, the use of fission energy represents the nearest term application of nuclear power for propulsion. Several fission based propulsion schemes have been proposed for in-space transportation, including pulsed nuclear explosions and the Nuclear Thermal Rocket[1] (NTR). In the NTR a cooling fluid or propellant is passed through a core of material that has been heated by fission. This makes the NTR effectively a heated gas rocket. With the present limitations of materials, NTR gas temperatures cannot exceed chemical propulsion gas temperatures. The use of hydrogen provides for an increase in Isp to 900 s. With $\Delta V \sim 9$ km/sec the propellant mass is reduced by an order of magnitude for a given spacecraft mass. Unfortunately, this is considerably offset by increased spacecraft mass (payload, structure, shielding, tankage etc.). A significant mass is required for the low mass density propellant (H_2) as the specific gravity of liquid hydrogen is around 0.07, compared to 0.95 for an O_2-H_2 chemical engine. The net result then is a propulsion system that is better than chemical, but not enough to really be a “game changer”. Proposed Nuclear Electric Propulsion (NEP) systems employ high Isp thrusters like the ion and Hall thrusters which solves the propellant Isp issue. The problem for NEP is the inherent inefficiency of the electrical power generation. Shedding the excess reactor heat requires an enormous radiator mass. The large reactor and power conversion masses just add to this problem making for too low a specific power (ratio of jet power to system mass) for rapid space transport.

Invoking nuclear fusion for space propulsion, at least as it has been envisioned up till now, does not significantly alter this picture as it has been developed primarily as an alternate source for electrical grid power. This endeavor is far from completion, and even if nuclear fusion were to be eventually developed for terrestrial power generation, the resulting power plant would be unlikely to have any role in space propulsion for all the same reasons that trouble NEP - but worse. Past efforts in this regard have all come to be dismissed, and rightfully so, primarily for the following two reasons. The first has been alluded to already. The propulsion system is reactor based. The straightforward application of a reactor-based fusion-electric system creates a colossal mass and heat rejection problem for space application. In a detailed analysis for the most compact tokamak concept, the spherical torus, spacecraft masses of 4000 metric tons (mt) were projected.[2] The maximum launch mass would need to be less than 150 MT if current chemical rockets are used for launch to LEO. The second is the use of the fusion plasma and/or the fusion products as propellant. Due to the resultant high exhaust velocities, the enormous mismatch from the appropriate exhaust velocity leaves the spacecraft with either insufficient thrust or enormous power requirements. Exotic fuels (^{3}He) or fuels with marginal fusion reaction efficiencies (e.g. P-^{11}B) with large circulating powers are also required.

If one were to imagine the optimal solution to this predicament, it would be a fusion propulsion system where *(*1) the power source releases its energy directly into the propellant, not requiring conversion to electricity. (2) It would employ a solid propellant that would require no significant tankage mass. (3) The propellant is readily heated and accelerated to high exhaust velocity (> 20 km/s), and where the propellant (4) has no significant physical interaction with the spacecraft thereby limiting thermal heat load, spacecraft damage, and radiator mass. The Fusion Driven rocket to be detailed in this paper represents an attempt to incorporate all four of these attributes, and in so doing, lead to a practical propulsion system that is capable of taking full advantage of the promise that fusion energy represents.

II. Fusion Driven Rocket

In this section the physics and method for achieving the compressional heating required to reach fusion gain conditions based on the compression of a Field Reversed Configuration plasmoid (FRC) is elucidated. In brief, an inductive technique is employed to accelerate an array of thin, predominantly lithium metal bands radially inward to create a three dimensional compression of the target FRC in a manner compatible with application in space.

A. Background

As first demonstrated at Trinity site (fission) and then at Eniwetok Atoll (fusion), the ignition of nuclear fuels have certainly confirmed the ability to produce copious energy yields from nuclear energy, dwarfing that of the Atlas V by many orders of magnitude. The challenge is how to have the release of nuclear energy occur in such a manner as to be a suitable match to that desired for manned planetary transportation or high power orbital maneuvers: multi-megawatt jet power, low specific mass (~ 1 kg/kW) at high Isp (> 2,000 s). It would appear that for at least nuclear fission, there is no real possibility of scaling down to an appropriately low yield as a certain critical mass (scale) is required to achieve the supercritical chain reaction needed for high energy gain. Fission nuclear pulse propulsion then, such as that envisioned in the Orion project, ends up with a thrust in the millions of megatons which would only be suitable for spacecraft on the order of 107 million MT - the mass of over 100 aircraft carriers!

Fortunately, the critical mass/scale for fusion ignition can be much smaller. The criteria to achieve D-T fusion ignition, at a nominal fuel (plasma) temperature of 10 keV, is the attainment of a density-radius product of $\rho \cdot R \sim 0.1$ g/cm.[2,3] This can be accomplished with a three dimensional compression of a spherical cryogenic fuel pellet of millimeter scale. Here it is assumed that the inertia of the small pellet is sufficient to confine the plasma long enough for the burn to propagate through the pellet and thereby produce an energy gain G ~ 200 or more (G = fusion energy/initial plasma energy). This Inertial Confinement Fusion (ICF) approach has been actively pursued for decades as it represents essentially a nano-scale version of a fusion explosive device. Because of the small scale and tiny masses, the energy delivery system required to heat the pellet to fusion temperature must be capable of doing so on the nanosecond timescale. It appeared that the most promising solution to accomplish this is with a large array of high power pulsed lasers focused down on to the D-T pellet. While the anticipated energy yield

is in the range appropriate for propulsion (E ~ 20-100 MJ), the scale and mass of the driver (lasers and power supplies) is not, as it requires an aerial photograph to image the full system.

There have been however three breakthrough realizations in the last several years that have provided the keys to achieving inertial fusion at the right scale in an efficient and appropriate manner for space propulsion. They primarily concern the enhanced confinement provided by significant magnetization of the target plasma which considerably eases the compressive requirements for achieving fusion gain and even fusion ignition. This new approach to fusion is aptly referred to as Magneto-Inertial Fusion (MIF), and will now be briefly described.

B. Magneto Inertial Fusion

The notion of using means other than an array of high power lasers to compress the target to fusion conditions goes back as far as the 1950's. Heavy ions and metal shells (liners) were two of the most promising. They all had in common the basic approach of ICF, i.e. the outer shell or

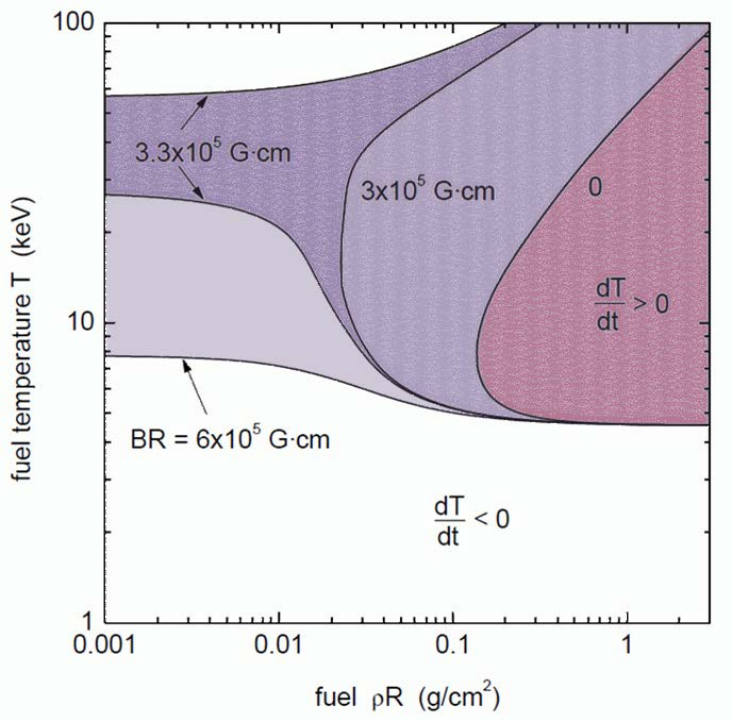

Figure 1. The BR form of the Lindle-Widner diagram. Ignition curves for different product BR (taken from Ref. 4). *When the BR parameter exceeds the threshold value, the dT/dt > 0 region extends to infinitely small ρR and ignition becomes possible at any ρR.*

liner is driven directly or indirectly inward compressing the inner target to fusion conditions. Regardless of method, this compression must be uniform, intense and accomplished with great precision resulting in large, high voltage and expensive driver systems. By the mid-nineties it was realized that the presence of a large magnetic field in the target would substantially suppress the thermal transport, and thus lower the imploding power needed to compress the target to fusion conditions. With more time before the target plasma thermal energy was dissipated, a much more massive confining shell could be employed for direct compression, with the dwell time of the confining (metal) shell now providing for a much longer fusion burn time. The liner does not need to be propelled inward by ablation but could be driven by explosives or even magnetic fields. In a seminal paper by Drake et al.[4] it was shown that with a fully three dimensional imploding shell on to the magnetized target, fusion gain could be achieved on a small scale with sub-megajoule liner (shell) kinetic energy. There was no known way to accomplish this at that time, but it was feasible at least in theory.

The second major theoretical result was obtained by Basko et al.[3] who showed that for a sufficiently magnetized target plasma, fusion ignition would occur even when the restrictive condition that $\rho \cdot R > 0.1$ g/cm^2 was far from being met. Ignition was now possible as long as the magnetic field-radius product, $B \cdot R > 60$ T-cm. Thus fusion ignition could be obtained for MIF targets with much lower compression than required for ICF as Fig. 1 indicates. The final critical element to enable fusion energy to be utilized for space propulsion was a practical method to directly channel the fusion energy into thrust at the appropriate Isp. It is believed that such a method has been determined that is supported by both theory and experiment. A description of the operating principles of the Fusion Driven Rocket will now be given.

C. Fusion Propulsion Based on Inductively-Driven Metal Shell Compression of a Magnetized Plasmoid

It was clear that fusion ignition conditions could be achieved at small scale by transferring the kinetic energy of a significantly more massive metal shell than the target plasma to compress it to high density and temperature. The question now becomes: (1) how to do this without invoking a massive and complex driver (2) how to do it in a manner that is efficient and capable of repetitive operation (3) how to create a suitable magnetized plasma target, and (4) how to transfer the fusion energy into a suitably directed propellant at optimal exhaust velocities and

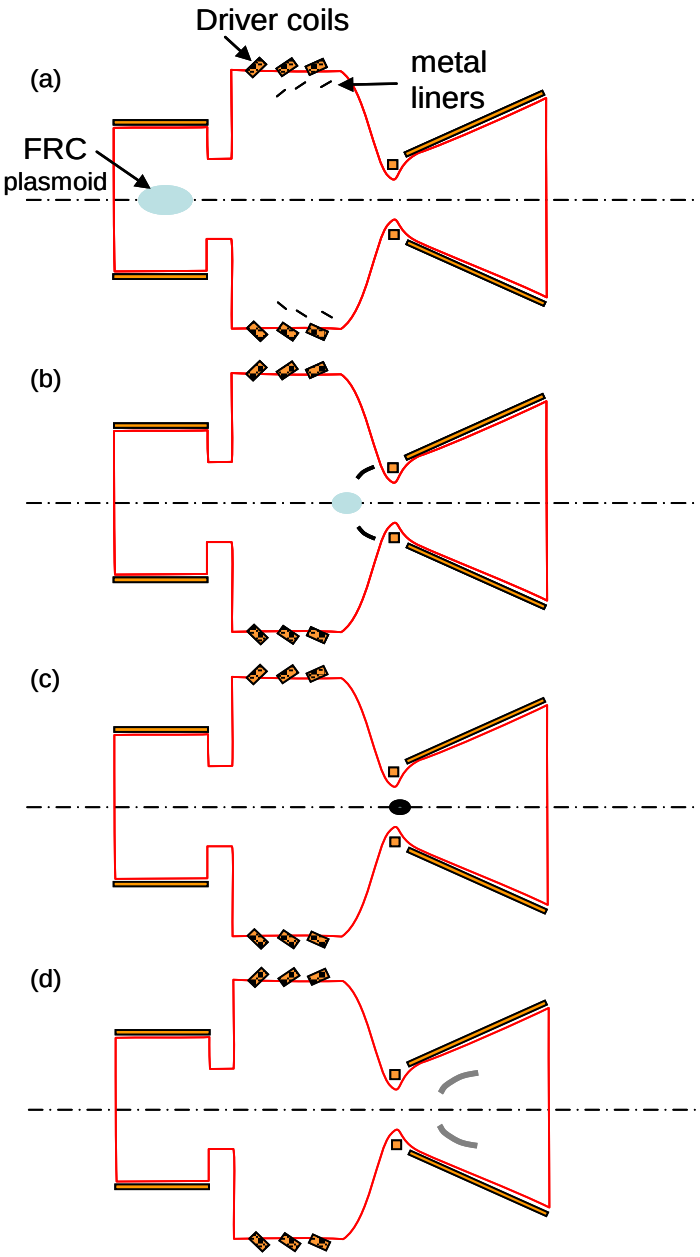

Figure 2. Schematic of the inductively driven metal propellant compression of an FRC plasmoid for propulsion. *(a) Thin hoops of metal are driven at the proper angle and speed for convergence onto target plasmoid at thruster throat. Target FRC plasmoid is created and injected into thruster chamber. (b) Target FRC is confined by axial magnetic field from shell driver coils as it translates through chamber eventually stagnating at the thruster throat. (c) Converging shell segments form fusion blanket compressing target FRC plasmoid to fusion conditions. (d) Vaporized and ionized by fusion neutrons and alphas, the plasma blanket expands against the divergent magnetic field resulting in the direct generation of electricity from and the back emf and a directed flow of the metal plasma out of the magnetic nozzle.*

powers for the missions mentioned earlier. The key to answering all four "hows" is based on

previous experimental work employing inductively driven liners to obtain megabar magnetic pressures[5,6], and magnetic compression of Field Reversed Configuration (FRC) plasmoids to fusion conditions.[7-9] A logical extension based on these results leads to a propulsion method that utilizes these metal shells to not only achieve fusion conditions, but then to become the propellant as well. The basic scheme for Fusion Driven Rocket (FDR) is illustrated and described in Fig. 2. The two most critical matters in meeting challenges (1) and (2) for MIF, and all ICF concepts for that matter, is driver efficiency and "stand-off" – the ability to isolate and protect driver and thruster from the resultant fusion energy release. By employing metal shells for compression, it is possible to produce the desired convergent motion inductively by inserting the metal shells along the inner surface of cylindrical or conically tapered coils. Both stand-off and energy efficiency issues are solved by this arrangement. The metal shell can be positioned up to a meter or more from the target implosion site with the coil driver both physically and electrically isolated from the shell. The driver efficiency can be quite high as the coil driver is typically the inductive element of a simple oscillating circuit where resistive circuit losses are a small fraction of the energy transferred. Even though there is essentially no magnetic field within the liners initially, there is enough flux leakage during the inward acceleration that at peak compression the axial magnetic field that is trapped inside the now greatly thickened wall can reach as high as 600 T.[6] As will be seen this field is considerably higher than that required for the compression of an FRC to achieve ignition and substantial fusion gain.

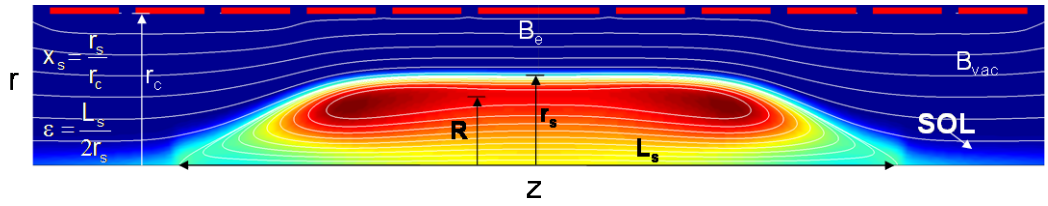

Figure 3. Elongated Field Reversed Configuration (FRC) Equilibrium Magnetic Field lines and Pressure Contours. *R is the radius to the FRC magnetic null, L_s and r_s are the FRC separatrix length and radius respectively.*

The next challenge to be considered is the magnetized plasma to be used as the fusion target.

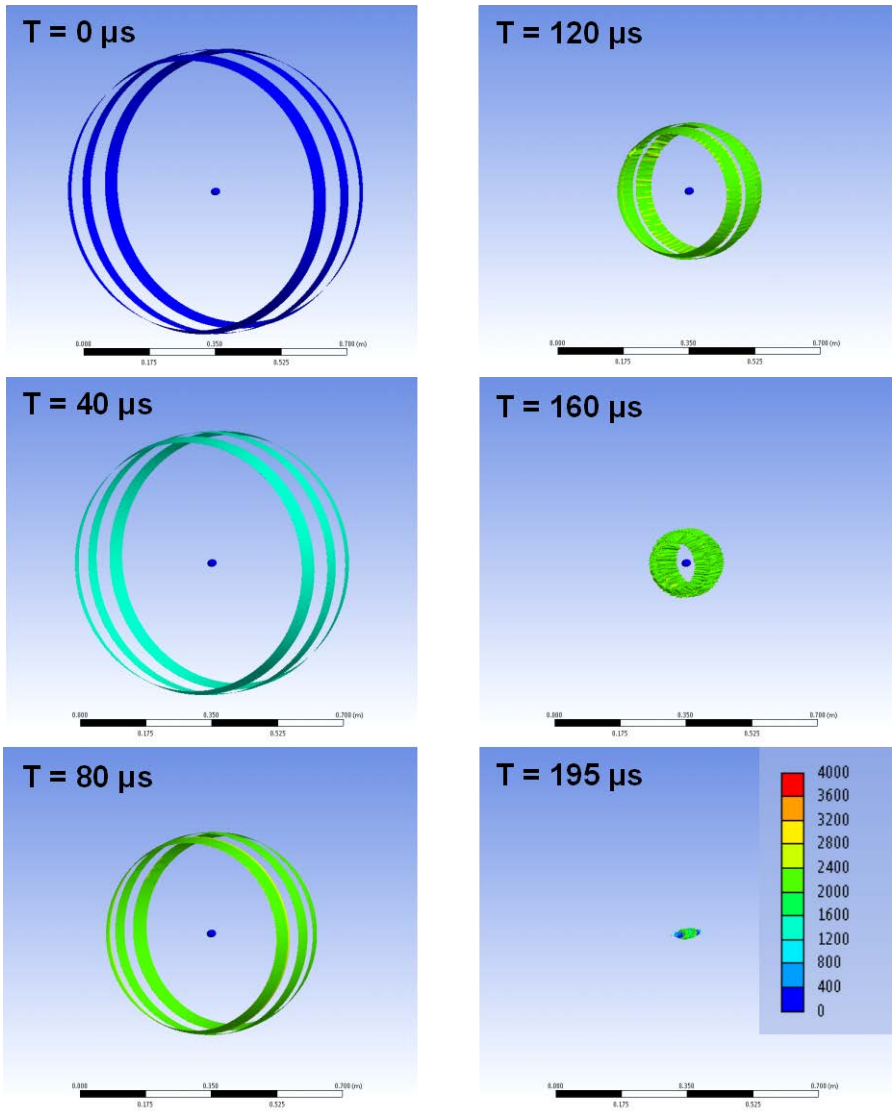

Figure 4. AEDS calculation of the 3D behavior of three 40 cm radius, 5 cm wide, 0.2 mm thick Aluminum liners converging onto a stationary test target. *The scale of the ellipsoid target (1×3.5 cm) is that anticipated for an initially 20 cm radius FRC compressed to 1 megabar energy density (410 T field).*

Spaced-based fusion demands a much lower system mass. The lowest mass system by which fusion can be achieved, and the one to be employed here, is based on the very compact, high energy density FRC (see Fig. 3).[9] It is of paramount advantage to employ a closed field line plasma that has intrinsically high β (plasma/magnetic pressure ratio), and that can be readily

translated and compressed, for the primary target plasma for MIF. Of all fusion reactor embodiments, only the FRC plasmoid has the linear geometry, and sufficient closed field confinement required for MIF fusion at high energy density. Most importantly, the FRC has already demonstrated both translatability over large distances[8] as well as the confinement scaling with size and density required to assure sufficient lifetime to survive the timescale required for compression. FRCs can, and have been generated with enough internal flux to easily satisfy the B·R ignition criteria at peak compression. At a nominal liner converging speed of 3 km/s, a 0.2 m radius FRC typical of operation on the LSX FRC device[7] would be fully compressed in 67 μs which is only a fraction of the lifetime that was observed for these FRCs (~ 1 msec).[9]

Finally, to complete the fourth challenge, a straightforward way to convert the fusion energy into propulsive energy must be devised. It is accomplished by employing an inductively driven thin metal liner to compress the magnetized plasma. As the radial and axial compression proceeds, this liner coalesces to form a thick (r > 5 cm) shell that acts as a fusion blanket that absorbs a large fraction of the fusion energy as well as the radiated plasma energy during the brief fusion burn time. This superheated blanket material is subsequently ionized and rapidly expands inside the divergent magnetic field of the nozzle. Here the thermal energy of the plasma is converted into directed propulsive thrust much like in a conventional nozzle but with the crucial difference being that the isolation provided by the magnetic field protects the chamber wall from bombardment by the energetic plasma ions. It would be possible to also derive the electrical energy required for the driver system from the back emf experienced by the conical magnetic field coil circuit via flux compression.[10] It was found however that the power required for recharging the energy storage modules for the metal liner driver coils could readily be obtained from conventional solar electric power. For very rapid, high power missions, the flux compressor/generator option could be adopted. For a near-term manned mars mission, solar electric requires the least technology development, lowest cost, and is already at the highest TRL level.

D. Physics of the Fusion Driven Rocket

The analysis of the liner implosion was carried out for both the subscale validation experiment now being performed at the University of Washington (UW), as well as what would be required for a full scale FDR prototype. For the purposes of the analysis given here, a very

conservative estimate of the liner kinetic energy that could be achieved is based on both modeling and what other inductive liner compression experiments have attained.[6,11] For concreteness, assumptions for the subscale tests were chosen to correspond to existing equipment at MSNW and the Plasma Dynamics Laboratory (PDL) at the University of Washington. The dynamics of the liner implosion are governed by the equation:

$$M_L \frac{d^2 r}{dt^2} = \left(\frac{B_{in}^2}{2\mu_0} - \frac{B_e^2}{2\mu_0} \right) 2\pi r w , \qquad (1)$$

where M_L is the liner mass, and w the liner width. During the rapid liner acceleration very little flux can diffuse through the liner (i.e. $B_{in} << B_e$). Due to the inertia of a solid metal liner, it is possible to sustain the magnetic field pressure (i.e. maintain a constant amplitude B_e) during this time by continually increasing the flux in the gap between the coil and liner to counter the increasing gap cross-sectional area as the liner moves inward. This occurs naturally for a simple L-C discharge circuit with an appropriately large capacitance. The near constant magnetic field during this time is observed experimentally and was confirmed by 3D modeling with the Maxwell® 3D electromagnetic code. With this approximation Eq. (1) is readily integrated to obtain the liner velocity v_L. B_e, is then determined by the stored capacitor energy minus liner kinetic energy, E_L. In a variant of the virial theorem, the maximum transfer of the stored energy, E_s, (= ½ CV_c^2) into liner kinetic energy is found when half of this energy is expended in the driving magnetic field energy, E_B. By employing a circuit design with low stray inductance, E_B will be concentrated primarily in the annular gap volume between the liners and the driving coils. One can thus derive an expression for the compression magnetic field during the short distance Δr over which the main liner acceleration is produced:

$$E_B = \frac{B_e^2}{2\mu_0} 2\pi r_L \Delta r w = \frac{1}{4} C V_C^2 \quad \Rightarrow \quad B_e = 7.8x10^{-4} \left(\frac{C}{w} \right)^{1/2} \frac{V_C}{r_L} , \qquad (2)$$

where B_e can be expressed as a function of only the initial liner physical dimensions and circuit parameters. Here r_L is the liner initial radius. The radial distance over which the compression field remains large as the liner moves inward, i.e. Δr, was taken to be equal to $r_L/6$.

This approximation was obtained from both experimental results and analytical circuit calculations. Equating the remaining stored energy with the liner kinetic energy (Ohmic losses in the liner and coil are calculated to be negligible here), one has then for the liner velocity:

$$v_L = \left(\frac{C}{\pi r_L w \delta \rho_m} \right)^{1/2} \frac{V_C}{2} \tag{3}$$

where the liner mass, $M_L = 2\pi r_L \cdot w \cdot \delta \cdot \rho_m$ with δ being the liner thickness, and ρ_m the density of the liner material.

The key process of the dynamical behavior of the convergent aluminum foil liners was analyzed by both a one dimensional analytic model that contains all of the relevant electrical circuit equations to provide for the calculation of the liner motion and heating due to changing magnetic fluxes and fields. The most accurate accounting of the liner dynamic behavior was obtained with the ANSYS Explicit Dynamics® Solver (AEDS). Here the full three dimensional non-linear behavior of the aluminum liners was modeled based on the magnetic pressure profile in time and space similar to that predicted by Eq. (1) and ANSYS Maxwell®. The result of a calculation with a physical setup similar in scale to the FDR prototype is shown in Fig. 4.

As mentioned, the FRC has been selected as the target plasmoid. There is practically no alternative plasma target to the FRC as it is the only closed field, magnetically confined plasma that has demonstrated the configuration lifetime scaling required for the relatively slow liner compression envisioned here. It is critical to have sufficient plasma confinement in order to retain plasma energy and inventory during the time required for the liner to reach peak compression. Even for the fastest implosion speeds achieved experimentally to date (~3 mm/μs), the time to maximum compression is several times the axial ion transit time. The FRC also has the distinct feature that even with a liner capable of only a 2D radial compression, the FRC will undergo an axial contraction due to the internal field line tension within the FRC, with the net result being effectively a 2.4D compression of the FRC. The energy within the FRC separatrix at peak compression is dominated by plasma energy that is in pressure balance with the edge magnetic field B_0. This allows one to write:

$$E_L = \frac{1}{2} M_L v_L^2 = 3 n_0 k T_0 \cdot \frac{4}{3} \pi r_0^3 \varepsilon = \frac{B_0^2}{\mu_0} \pi r_0^3 \varepsilon \,, \tag{4}$$

where the zero subscript indicates values at peak compression. The last expression in Eq. (4) reflects the reasonable assumption that $r_s \sim r_0$ and that the FRC plasma is in radial magnetic pressure balance ($2n_0kT_0 = B_0^2/2\mu_0$). One has then for the fusion energy produced in the FRC during the shell's dwell time τ_D at peak compression:

$$E_{fus} \cong \; 1.2\times10^{-12}\, n_0^2 \langle \sigma v \rangle \frac{4}{3} \pi r_0^3 \, \varepsilon \, \tau_D \;\; = \;\; 1.1\times10^{-42}\, n_0^2 T_0^2 \frac{r_0^4}{v_L} \varepsilon \tag{5}$$

Adiabatic Law:	$P \sim V^{-5/3}$	$\Rightarrow$	$T \sim B_e^{4/5}$
Rad. P Balance:	$P \sim nkT \sim B_e^2$		$n \sim B_e^{6/5}$
Particle Cons:	$nV = \text{const.}$		$r_s^2 l_s \sim B_e^{-6/5}$
FRC φ Cons:	$\varphi \sim r_c^2 B_e$ (const x_s)		$l_s \sim r_s^{2/5}$

Parameter	Merged FRC ($t = \tau_{1/4}$)	Radial FRC Compression	Axial FRC Compression
v_L (km/s)	2.5	~ 0	0
r_L (cm)	22.5	0.9	0.9
r_s (cm)	20	0.8	0.88
l_s (cm)	80	22	3.5
B_{ext} (T)	0.16	100	410
T_e+T_i (keV)	0.06	5	15
n (m^{-3})	1.1×10^{21}	2.5×10^{24}	1.4×10^{25}
E_p (kJ)	2.2	180	560
E (Pa)	1.5×10^{4}	6×10^{9}	10^{11}
τ_N (μs)	600	175	270

Figure 5. (Top) FRC adiabatic scaling laws, and (Bottom) Anticipated FRC parameters from merging, a purely radial, and a purely axial compression. *During the actual liner implosion the FRC radial and axial compressions would occur simultaneously. They are calculated separately to show their relative effects.*

where n_0 and T_0 are the peak density and temperature. The liner shell dwell time at peak compression, τ_D, is approximated as ~ $2r_0/v_L$, the time it would take the liner to reach the axis unimpeded and rebound to r_0. The dwell time will actually be much longer for a thick liner as the outer liner surface continues to travel inward until the shock from the halting of the inner liner surface reaches the outer surface. This time can be much longer than the assumed τ_D since r_L^{outer} ~ $6r_0$. The more conservative dwell time is assumed here as liner compressive effects are also not considered in this zero order analysis. The usual approximation for the D-T fusion cross section in this temperature range (5-40 keV): $\langle\sigma v\rangle \cong 1.1\text{x}10^{-31}\ T^2(\text{eV})$ was also assumed. Radial pressure balance, together with expressions (4) and (5) yields for the fusion gain:

$$G = \frac{E_{fus}}{E_L} \quad = \quad 1.73\times10^{-3}\sqrt{\frac{M_L}{l_0}}\,B_0 \quad = \quad 4.3\times10^{-8}\sqrt{M_L}\;E_L^{11/8} \tag{6}$$

where l_0 (= $2r_0\cdot\varepsilon$) is the length of the FRC at peak compression. The last expression is obtained from the adiabatic scaling laws for the FRC (see Fig. 5):

$$E_L \sim B_0^2\, r_0^2\, l_0 \sim B_0^{4/5} \;\; and \;\; \quad l_0 \sim r_0^{2/5} \sim B_0^{-1/5} \tag{7}$$

in order to express G in terms of the liner kinetic energy and mass, E_L and M_L only.

Starting with typical FRC parameters achieved in past experiments one obtains the final FRC parameters reflecting both radial and axial adiabatic compression from the 3D convergence of the liners. The ends of the merged liners are observed to do this naturally in the AEDS calculations (see Fig. 4), as a consequence of a significant, axially-inward liner motion. The unique response of the FRC equilibrium to axial liner compression is quite valuable in this context as it provides for magnetic insulation of the FRC boundary regardless of the increase in the ratio of plasma to magnetic energy that comes with the increased axial compression.

While the FRC can be generated over a wide range of sizes, temperatures and densities and then translated into the liners for further compression, the proper plasma parameters for the initial FRC are best found by extrapolation back from the desired final state. The compression

that is applied by the liners is adiabatic with regard to FRC as the liner speed is far less than the plasma sound speed. The key adiabatic relations for the FRC are stated in Fig. 5. The injection of the FRC is delayed until the liners have been fully accelerated and have moved inward away from the driver coils. For the validation experiments currently being constructed, two FRCs will be injected and merged inside the liner as this permits an axially stationary liner compression. This limits vacuum end wall damage and considerably eases the diagnostic evaluation of the compression process as the target remains fixed. Adding a translating component to the liner motion is straightforward and would be something to be addressed in the next phase of development of FDR.

The inward liner motion and compression ceases when the internal FRC energy has increased to the point to where it stagnates the liner inward motion. At this point the plasma energy will roughly equal the initial liner kinetic energy. From Fig. 5 the final compressed FRC length is 35 mm at an internal pressure characteristic of a 410 T field ~ 67 GPa. Ideally, the capacitor energy storage and driver circuit at the UW is capable of generating liner energies where E_L = 560 kJ. The 3D convergence of an Aluminum liner set with an initial total mass of 0.18 kg would produce a fusion gain G = 1.6. If realized, this would be an extraordinary achievement for such a modest experiment, and a testament to the cost and efficiency advantages of this approach to fusion.

The total gain desired from the FDR is determined by the energy requirements to vaporize, ionize and energize the metal liner propellant to achieve a suitably high Isp. It is useful then to rewrite Eq. (6) in terms of the fusion energy produced per unit liner mass, or

$$\frac{E_{fus}}{M_L} = G\left(\frac{E_L}{M_L}\right) = 4.3\times10^{-8}\, M_L^{15/8}\, v_L^{4.75} \tag{8}$$

where Eq. (4) was used to put the expression in terms of the explicit liner variables. It can be seen that increasing either the liner mass, or velocity will increase the energy input into each liner particle for higher Isp. There is however a velocity limit for a given liner material and thickness. This set by a material's properties (electrical conductivity, melting point, and heat capacity) in order to avoid vaporization due to the inductive heating that the liner experiences

during magnetic acceleration of the liner. As was first pointed out by Cnare in his landmark foil compression experiments, the liner's minimum thickness (mass) for a given liner velocity can be characterized by a parameter g_M defined by the "current integral":

$$\int_0^{t_m} I^2 dt = g_M A^2 \tag{9}$$

where I is the current flowing through the material cross-sectional area, $A = w \times \delta$, (w is the hoop width and δ the hoop thickness). The driving force is simply the magnetic pressure ($B^2/2\mu_0$) applied over the surface area of the metal shell facing the coil when in close proximity to the driving coil. The current can be related to the field through Ampere's law which can be reasonably approximated as $B_e = \mu_0 I/w$. Normalizing to the action constant for the vaporization of aluminum from an initial 300 °K, i.e. where $g_{Al} = 5.9 \times 10^{16}$ $A^2 \cdot sec/m^4$, one finds for the maximum velocity for a given shell thickness δ:

$$v_{\max} = 6.8x10^{10} \frac{g_M}{g_{Al}} \frac{\delta}{\rho_M}, \tag{10}$$

where ρ_M is the shell material density. While the liner thickness limits the launch velocity, once in motion further heating is no longer an issue, even during the final field compression, due to the thickening of the liner with convergence. To achieve sufficient gain, the liner initial thickness will typically be much greater than that needed for the characteristic velocities (2-4 km/s) anticipated.

There are potentially several metals that could be employed. Not surprisingly, aluminum is a strong contender due to its low density and high conductivity, but lithium is not far behind. For a given liner energy, its low mass density allows for thicker initial liner as well as a larger final shell radius. The latter is important for slowing down the fusion neutrons and extracting the maximum energy from the fusion products. Possessing a low yield strength, lithium also has several advantages as a plasma propellant. Recall that the ultimate fate of the shell is vaporization and ionization after intense fusion, Ohmic and radiative heating. Lithium is to be

favored for its low vaporization temperature and ionization energy thereby minimizing the frozen flow losses. Due to its low atomic mass it will also attain the highest I_{sp} for a given fusion energy yield. For these reasons, lithium is the propellant of choice for the FDR. From Eq. (10) one finds for lithium: v_{max} (km/s) = 16·δ(mm). As will be seen, the anticipated lithium liner thickness is several mm so there is no real issue here as high gain can be accomplished with liner velocities of 3-4 km/s. For the validation experiment aluminum is the clear choice due to its wide availability, low cost, and ease in handling.

To achieve ignition, a fusion gain G > 5 is desired along with sufficient magnetic field for the magnetic confinement of the fusion product alpha (^{4}He) within the FRC plasmoid. With fusion alpha heating, ignition conditions are achieved and the effective gain can be significantly increased, potentially to as large as several hundred as noted above.

III. Mission Analysis

Following the manned Moon missions, it was assumed that the next stepping stone towards mankind's exploration of the solar system would be a mission to Mars. While mankind has certainly achieved many space milestones which have led to significant scientific discoveries, up to now manned space travel has been severely limited. The reasons for this can be boiled down to two main issues. Simply put, with current technologies manned exploration of the solar system: (1) takes too long and (2) costs too much. With a closer look at virtually all the issues encountered when considering a manned planetary mission, the main problem will come back to these two reasons. For example, space travel outside the protection of the Earth's magnetosphere presents a myriad of safety issues for human beings. Foremost, there is exposure to radiation and high energy particles that can cause significant cancer risk as well as bone and muscle loss due to the lack of sufficient gravity. Both these health issues only become major issues for long durations in the space environment. Radiation exposure can be lessened by bringing massive shielding into space, and muscle and bone loss can be limited by creating artificial gravity. However to do so, would simply transfer these issues to the "cost too much" category. In addition to physical safety, there is also mental fatigue that can become problematic for long duration missions. Finally, and perhaps most catastrophically, long duration missions can have an increased risk of critical failure.

Beyond safety, there are also the issues associated with the political climate over long periods of time. Policies and program directives can change significantly from administration to administration, making large-scale, long term manned space exploration difficult to fund in a consistent way. Along those same lines, the general interest of the public must be maintained for long missions as well. While the aforementioned does not entail a complete list of the concerns associated with space travel it does provide good examples of the major issues that scale as a function of mission time.

Space operations have never been inexpensive endeavors, and the added complexity of manned spaceflight only adds to the cost. This is one of the major reasons for robotic exploration as is done currently. There are direct costs incurred with sending men into space, such as operational costs as well as the expenses associated with complex pre-deployed assets or on-orbit assembles usually required for manned planetary exploration. It is worth noting that both these

direct costs also scale with mission length. Generally speaking, both operational and space asset cost go up significantly for longer duration missions. There are also launch costs required for any space mission. At $10,000 per kg to LEO, large space structures and fuel depots quickly come to dominate the cost.

A solution that addresses both of these two obstacles to manned space travel is a propulsion method that has high specific power, α (engine power/spacecraft mass) in addition to high exhaust velocities (Isp). High specific power (α of order unity) to significantly reduce trip times, and high Isp (> 3,000 s) dramatically increase payload mass fraction, greatly reducing initial mass at LEO. The overarching design criteria therefore, is a mission architecture based on a propulsion system that can complete a manned Mars mission in 210 days using only a single launch from Earth. How this is to be accomplished with the Fusion Driven Rocket will now be outlined.

A. Previous Mars Mission Analysis

A manned Mars case study was chosen as this would clearly be the first destination for a planetary manned mission. Manned Mars missions have been analyzed many times over the ensuing decades after Apollo with a large variety of spacecraft and propulsion methods. The most recent and possibly the most detailed was that conducted by NASA in the 2000s.[12] The results of that study were summarized in the Design Reference Architecture (DRA) 5 in 2009. Many of the aspects of this study, such as payload and habitat mass, were used as the starting point for the reference architecture for the FDR. In addition the NASA DRA 5 detailed the full scope of Mars exploration options, including launch, Earth orbital operations, trans-Mars injection (TMI), Earth-Mars cruise, Mars orbit insertion (MOI), Mars orbital operations, entry/descent/landing, surface operations, Mars ascent, on-orbit rendezvous, TMI, and Earth arrival. The DRA 5 also developed many figures of merit to evaluate what are referred to as Opposition-Class and Conjunction-class missions. Opposition-class missions are typified by short surface stay times at Mars (typically 30 to 90 days) and relatively short total round-trip mission times (500 to 650 days). The exploration community has adopted the terminology “short-stay” missions for this class. Conjunction-class missions are typified by long-duration surface stay times (500 days or more) and long total round-trip times (approximately 900 days). These missions represent the global minimum-energy solutions for a given launch opportunity.

What was concluded in DRA 5 is that the choice of the overall exploration mission sequence and corresponding trajectory strategy has perhaps the greatest single influence on the resulting architecture. It was stated that “the ideal mission would be one that provides: (1) the shortest overall mission to reduce the associated human health and reliability risks; (2) adequate time on the surface in which to maximize the return of mission objectives and science; and (3) low mission mass, which, in turn, reduces the overall cost and mission complexity.” It was also determined that the ideal mission did not exist, and it was clear it was principally due to the limitation in propulsive capabilities which resulted in stringent confinement to orbital mechanics and planet phasing. Basically, a short-stay mission approach would require departing Mars on a non-optimal return trajectory, while a long-stay approach time would be spent at Mars waiting for more optimal alignment for a lower-energy return. It is important to note that the risk assessment that was conducted in DRA 5 indicated that both the short-stay (Opposition-class) and the long-stay (Conjunction-class) mission option posed a high risk to crew members that would exceed the current permissible radiation exposure limits. It was concluded in DRA 5 that a Conjunction-class or long stay mission would be favorable. This was largely based on the criteria of Crew Health and Performance (CHP) components. This metric was broken down into Physiological Countermeasures, Human Factor and Habitability, Radiation, Behavioral Health and Performance, and Medical Capabilities. Even though the Conjunction-class mission showed an overall increase risk to Behavioral Health and Performance, as well as Medical Capabilities due to longer overall duration, it was favorable based on less 0-g transit phases and less exposure to free space heavy ion environment. The other major reason that was sighted as preferable for long-stay missions is the percentage of time spent at Mars compared to the total mission time. Again, due to lack of adequate propulsion, the Opposition-class loses out. However with increased propulsion capabilities it is not only possible to increase this percentage to a significant fraction even for short-stay times, it is also possible to lessen all the major CHPs including bringing the radiation exposure to with permissible exposure limits.

B. Designing a New Mission to Mars

Mission Architecture Goals
➢ 90 day transit times to and from Mars ➢ Single launch to Mars (130 MT IMLEO) ➢ No pre-deployed assets ➢ 22 MT Payload mass ➢ Full propulsive MOI ➢ Full propulsive EOI ➢ Reusable spacecraft

Table 1. *Mission goals based of the objective of reducing transit*

A top down approach was used to examine the effects of fusion propulsion on manned exploration of the solar system. This is the most sensible way to avoid having the fusion concept "tail" wag the mission "dog". Given the large uncertainty in the maximum fusion gain,

System Mass Summary	Mass (MT)
Mars Entry Vehicle	22
Crew/Consumables	2
Transit habitat (MTV)	15
FDR spacecraft	15
Total Dry Mass	54

Table 2. Spacecraft day mass summary including Mars payload *This table includes the Mars transit habitat as well as the supporting life support and subsystems*

spacecraft α and Isp, it made more sense to specify the desired mission goals (see Table 1) first,

and have that in turn determine the type and scale of the fusion system – assuming of course that the fusion system can provide the necessary α and Isp.

The first set of mission analysis performed for FDR was conducted using trade studies of fusion gain and single trip time from Earth to Mars.[13] The objective of the work reported here was to expand upon a single case study to determine the exact fusion conditions that would be needed to achieve the ideal Mars mission as outlined in Table 1. To this end, two of the criteria were selected for this case study as most important: a 90 day transit to Mars, and a single launch of the spacecraft to LEO. The 90 day transfer was considered the most important parameter as it not only reduced the cost and safety risks of a manned mission to Mars, but was the simplest, if not only viable way to bring radiation exposure to within permissible limits. While missions faster than 90 days were certainly feasible with FDR propulsion, the ΔV budget increased significantly, driving down payload mass fraction, and ultimately increasing initial mass in low earth orbit (IMLEO). This leads to the second main criterion which limits the IMLEO mass to

Mission Assumptions		
Payload mass	63	MT
Spacecraft mass	15	MT
Earth Orbital Altitude	407	km
Mars park orbit	1	sol
	250x33793	km
Capacitor specific mass	2.5	J/g
Solar panel specific mass	200	W/kg
Tankage fraction	10	%
Isp	5000	s
Fusion Gain	200	

Table 3. Mission assumption based on the payload and park orbits from DRA 5. *Specific masses and engine performance parameter assumed to fulfill the mission architecture goals stated in Table 2.*

130 MT or less. It was felt that this was an important element in the feasibility of manned Mars missions as it greatly simplifies the total mission plan and substantially reduces mission costs.

Beyond these two main mission criteria several other mission stipulations were set forth. Foremost was a set payload masses. For this study the payload to Mars would be primarily a Mars Entry Vehicle of 21 MT. This vehicle would consist of the entry, descent, and landing

Maneuver	ΔV (km/s)	ΔT (days)	Mi (MT)	Mf (MT)	Mp (MT)
TMI	7.6	6.5	116.4	99.6	16.8
MOI	13.8	9.5	99.6	75.1	24.5
TEI	16.2	5.8	53.1	38.2	14.9
EOI	11.8	3.2	38.2	30	8.2

Table 4. Mission Maneuvers

system, the surface habitat for the 30 day stay, as well as the ascent module to rendezvous with the orbiting FDR spacecraft. Consumables were estimated to be 1.5 kg per person per day. For a crew of six on the 210 day mission this was almost 2 MT. The payload for the entire mission, or the return payload to earth, would be the Mars Transfer Vehicle (MTV) consisting of an inflatable-type structure and weighing 15 MT. It is worth noting a Crew Exploration Vehicle (CEV) or Earth re-entry vehicle is not included in the mass budget. One of the mission assumptions was to have FDR as a reusable spacecraft. Therefore the entire spacecraft will be in circular Earth orbit were a rendezvous with a CEV could be made. By doing so 11 MT of mass that would not needless be taking all the way to Mars and back. The dray mass breakdown is shown in Table 2.

Two other mission stipulations for this study were the use of full propulsive orbit insertion maneuvers at both Mars and Earth return. Eliminating aerobraking at Mars reduces risk and complexity of the spacecraft and mission architecture. Furthermore it was shown in earlier analysis[13] that the mass of the heat shield required for an Aerobraking maneuver is much more massive than the propellant needed by the FDR to perform the same ΔV maneuver. While chemical propulsion missions and even NTP propulsion show large mass saving by using aerobraking instead of more propellant, this is not true of a high Isp engine. Along similar lines there is the aerocapture maneuver that is normally assumed upon Earth return. DRA 5 took into account that aerocapture at Earth was possible and well understood based on previous flight experience. It employed return trajectories with Earth entry speeds for a nominal Mars return trajectory that were as high as 12 km/s. This was deemed acceptable based on the 11 km/s

required for the lunar Crew Exploration Vehicle (CEV). For this case study an Earth Orbit Insertion maneuver was conducted instead of relying on a direct entry approach from Mars. This was done for two reasons. First, it allows for the standard CEV to be used without necessitating the development of higher density, lightweight, thermal protection systems. Second, by allowing the spacecraft to enter into an earth orbit upon return from Mars, the FDR spacecraft would be ready for future missions simply by re-launching a new payload and additional propellant. As will be discussed later, the FDR spacecraft is designed as a reusable system.

C. Mission Design Details

With the basic mission goals outlined, trajectory optimization was carried out using the COPERNICUS software. COPERNICUS is a NASA developed code that provides a single, unified framework for modeling, designing, and optimizing spacecraft trajectories for robotic and human missions. The methodology facilitates modeling and optimization for problems ranging from a single spacecraft orbiting a single celestial body, to a mission involving multiple spacecraft and multiple propulsion systems operating in gravitational fields of multiple celestial bodies. The model was set up to start with an initial (and final) Earth orbit of 407 km. This was done to allow comparison with the DRA 5 mission architecture. The parking orbit at Mars was also taken from DRA 5 as 1 sol orbit, which has a periapsis altitude of 250 km and an apoapsis altitude of 33,793 km. The mission was modeled using 7 segments: Trans Mars Injection (TMI), Trans-Mars coast, Mars Orbit Insertion (MOI), stay time, Trans-Earth Injection (TEI), and an Earth Orbit Insertion (EOI). Segment functions were setup to limit the entire mission time to 210 days and mandates that the Mars stay time be no less than 30 days. The mission architecture was also set up so that the payload mass of 39 MT was dropped off at Mars and the 30 MT spacecraft mass was returned to earth. The spacecraft mass assumed here is based on first iteration design efforts and spacecraft scaling optimization that was conducted in previous work.[14] A list of the mission parameters can be found in Table 3. The COPERNICUS code was employed to find a minimum ΔV trajectory for these mission parameters. The code was allowed to optimize departure date as well as the length of all 4 maneuvers (TMI, MOI, TEI, EOI) as well as the coast times.

COPERNICUS optimized to a slightly shortened trip time to Mars of 80.8 days and a return trip time of 99.2 days. The total ΔV budget for the mission optimized to a minimum of roughly 50 km/s. The ΔV as well as the burn time of each maneuver is listed in Table 4.

The original trajectory optimization was conducted using a simplified orbital model in order for CORPERNICUS to perform a wider range of parameter sweeps. This model allowed for finite burns and coast periods, but did not fully model the escape and capture maneuver's required at both Earth and Mars. Therefore it was necessary to examine in detail the near body

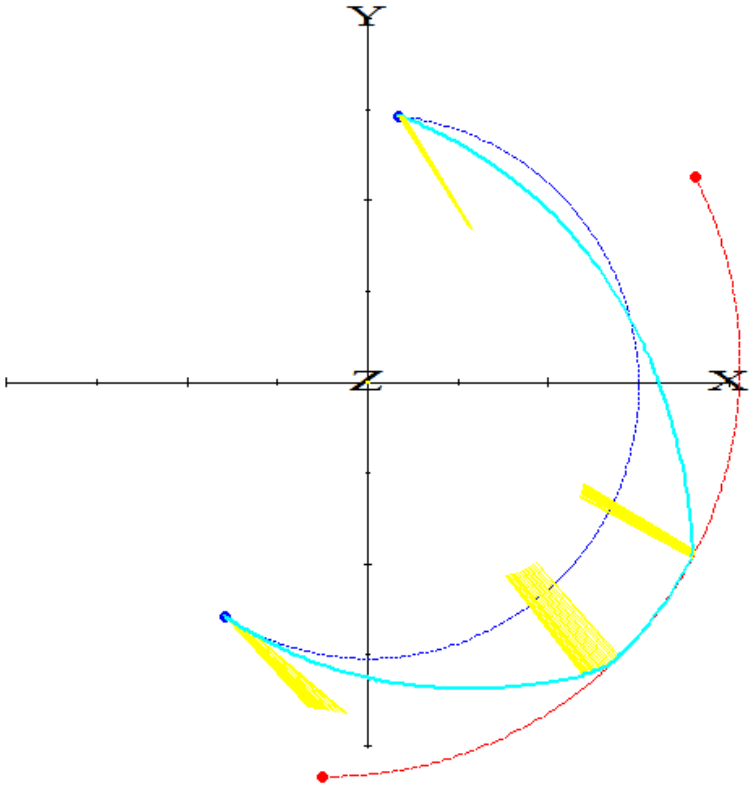

Figure 6. COPERNICUS visualization of the ΔV optimized trajectory for a 210 day manned mars mission. *Mission consists of Includes a 82.9 day Earth-Mars transit, a 30 day stay, and a 97.1 day Mars-Earth return.*

orbital mechanics and the required maneuvers to enter or exit their gravitational influence. Figure 6 depicts the results from COPERNICUS with finite burn maneuvers for TMI, MOI, TEI, and TOI. All of the ΔVs for these maneuvers were within 2% of the ΔV determined from the simplified full mission profile optimization except for the TOI maneuver. This maneuver, as

shown in Fig. 6, required an additional impulsive maneuver in order to circularize the orbit at the 407 km LEO orbit. This was done to allow COPERNICUS to converge to a solution using rather high thrust impulse burns. A more optimized Earth Orbit insertion maneuver will be calculated in future mission designs, but for this preliminary design the ΔV budget presented in Table 4 is sufficient.

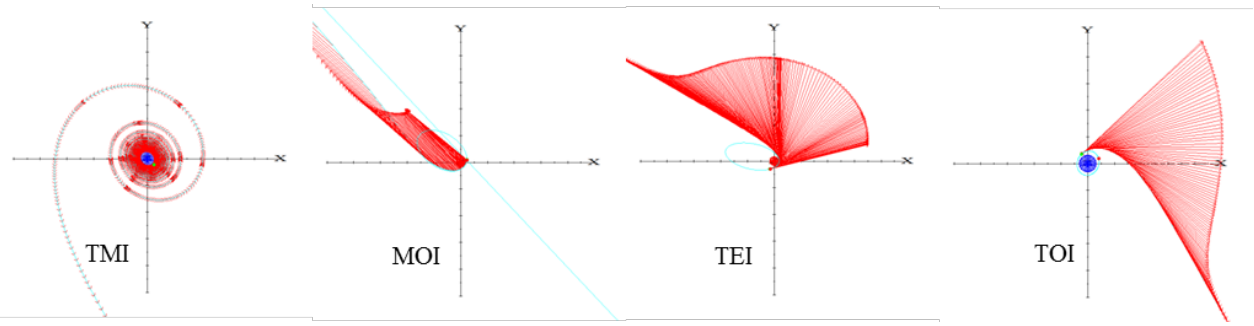

Figure 7. COPERNICUS visualization of the optimized, near-body finite burns for the 210 day architecture. *An initial park orbit of 407 km at Earth and a 1 sol park orbit at Mars was assumed.*

With the ΔV determined for an ideal Mars mission that satisfies both criteria (1) and (2) as stated in DRA5, the final criteria (3) is to be determined by the characteristic specific impulse of the propulsion system. This final criteria is a low mission mass, and it was the goal of this case study to have the mass small enough to enable a single launch to Mars. Based on projections for future heavy lift vehicles, the mass limit for IMLEO is 130 MT. It is also worth noting that if future heavy launch vehicles cannot achieve this metric the mission architecture for this case study would simply require two separate launches and a single on-orbit rendezvous. In this scenario it would be speculated that the FDR spacecraft would be sent up first and a pre-mission check would be conducted including main FDR testing without the crew members on board. The second launch would be the payload plus crew. This type of system checkout is likely to be desirable in either case.

Within the COPERNICUS code, propulsive maneuvers can be determined using any number of thruster parameters. For this case study an Isp was chosen to be 5000 s and the power allowed to be optimized in order for the initial spacecraft mass to be less than 130 MT. This Isp value is

consistent with a fusion gain of 200. With an Isp of 5000 s and the optimal ΔV budgets for the specified mission requirement, as well as the specified payload and spacecraft mass, COPPERNICUS calculations determined that a jet power of 36 MW would be needed to complete the mission. With the power defined, an overall picture and scaling of the spacecraft itself is now possible.

As was stated, the objective was to dramatically improve upon current mission Mars architectures in order to bring a manned mission within fiscal and conceptual reach. Design architectures that use convention chemical propulsion require up to 12 heavy lift launches and as much as 1,252 MT in LEO. With Nuclear Thermal Propulsion this mass can be reduced to 849 MT over 9 launches. This is compared to a single launch of 134 MT for Fusion Driven Rocket architecture. These metrics of comparison are summarized in Table 5. The DRA architectures require significant pre-deployed assets at Mars prior to a manned mission. This includes propellant for the return trip home as well habitats and supplies for a stay time of 539 days. And

Mission Comparison	**FDR**	**DRA 5 NTP**	**DRA 5 chemical**
Number of launches	1	9	12
IMLEO (MT)	134	849	1252
Mission time (days)	210	914(1680)	914(1680)

Table 5. Mission launch requirements. *Mass required in LEO, and the overall mission time for the 210 day FDR Mar mission compared to the DRA architecture using both Nuclear Thermal Propulsion (NTP) and chemical propulsion systems.*

while this case study assumed the 63 MT payload of the manned portion of the DRA architecture it did not presume to include any of the pre-deployed assets as the stay time was reduced to 30 days and all the propellant need for the round trip mission would be carried in the original spacecraft. Because the architecture requires pre-deployed assets to be placed at Mars before the mission can begin, the total mission time for start to finish is 1680 days

Spacecraft Component	Mass (MT)
Spacecraft structure[1]	3.4
Lithium containment vessel	0.1
FRC formation system[2]	0.5
Propellant Feed mechanism	1.2
Energy storage[3]	2.5
Liner driver coils[4]	0.3
Energy delivery system[5]	1.2
Solar Panels[6]	2.0
Thermal management	1.1
Magnetic expander	0.2
Margin	2.5
Spacecraft Mass	**15**
Crew habitat (DRA5.0)	63
Lithium Propellant	56
Total Mass	**134**

Table 6: FDR Spacecraft Mass Budget

1. Fairings, support structure, communication, data handling ACS, Batteries 2. Hardware responsible for formation and injection of Fusion material (FRC)

3. Capacitors (1.8 MJ @ 1 kJ/KG), switches, power bus

4. Electromagnetic coil used to drive inductive liner

5. All other pulsed power components (see text)

6. 180 kW @ 200 W/kg

IV. Spacecraft Design

Based on the mission down design approach, requirements have been set forth for a spacecraft that is less than 15 MT and is comprised of a rocket engine that can produce 36 MW of jet power at an Isp of 5000 s. This section will focus on the limitation of 15 MT for the spacecraft dry mass, and detail how the FDR design can satisfy this design requirement.

One of the most significant masses in the FDR concept is the energy storage system required to energize the liners. This is accomplished with high voltage, pulse capacitors. Using the straight gain equations from the fusion physics section D, and assuming an additional enhancement from ignition of 10 to achieve a fusion gain of 200, a total liner kinetic energy of at least 2.8 MJ will be required. A total liner mass of 0.5 kg results in an Isp ~ 5000 s as desired. To achieve an average jet power of 36 MW with 90% conversion efficiency will require a rep rate of 1/14 sec^{-1} providing sufficient time for liner reload and recharging the energy storage systems. It will be assumed that the stored (bank) energy must be at least twice the liner kinetic energy. A coupling efficiency of 45% is assumed which, as was mentioned earlier, is near the optimum coupling efficiency and is consistent with the 1D circuit modeling.[15] A 6.2 MJ bank of capacitors is thus required. Commercial high voltage, high energy density, pulse capacitors have demonstrated energy densities as high as 3 J/g.[16] While improvement in performance can be expected in the future, the assumption here for the FDR spacecraft design will be 2.5 J/g reflecting a devaluation for space rating and margin, and resulting in a total capacitor mass ~ 2.5 MT. Based on laboratory experience, the energy delivery system (SEP converters, charging system, start and crowbar switches, housings, support structures, power feeds, cable, and stripline) will scale with the capacitor mass. The multiplier would certainly be less than half the capacitor mass. A very conservative value of roughly half however is assumed or 1.2 MT.

The second major power system component that is required are solar panels. It is important to note that the Fusion Driven Rocket, at least as it is envisioned for its first flight mission, will power the fusion reaction using electrical energy derived from solar panels. There are several reasons for this. First, solar panels have a long flight heritage and a proven performance record in space. They have flown on over 99% of space missions launched to date. Second, while energy could certainly be obtained from the flux compression occurring during propellant expansion out of the rocket engine, this adds complexity and risk. While this type of energy recovery may be

incorporated later in a fusion rocket development program, it was not felt to be critical to the concept feasibility.

The current state of the art solar panels (e.g. the MegaFlex program) are expected to generate over 200 W/kg, and this value was used in calculating the solar panel specific mass. It should be

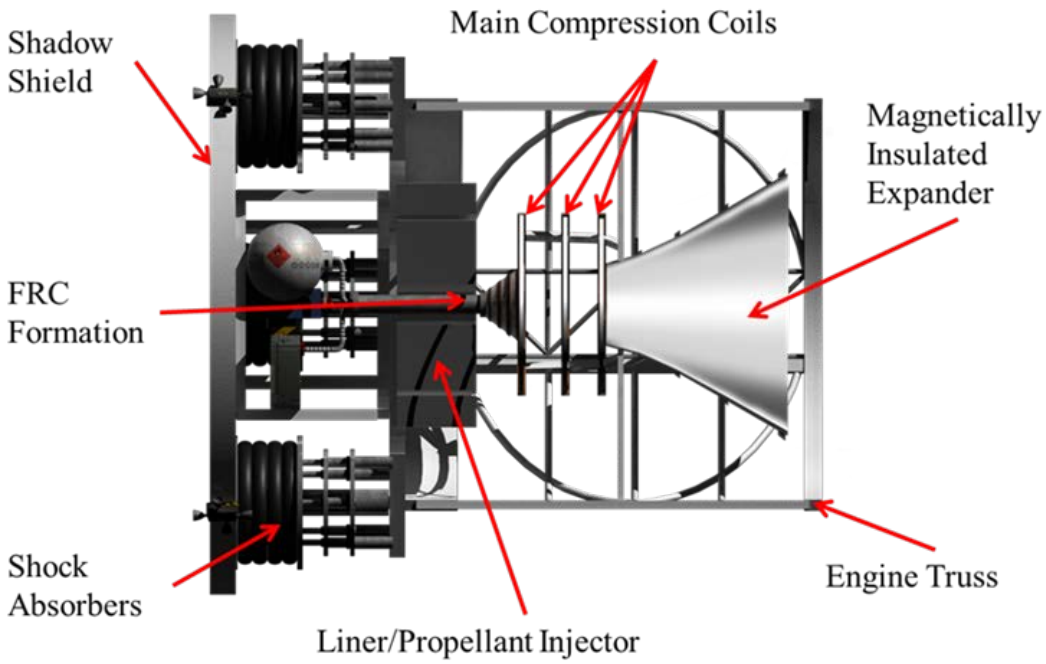

Figure 8. Schematic of the Fusion Driven Rocket including major subsystems.

noted that the development of much higher density solar arrays are anticipated in the near future. It has been predicted that 500 W/kg, possibly up to 1000 W/kg would be possible with advanced III-V multi-junction cells.[17] At a fusion gain of 200 the 36 MW of jet power needed for the 210 day Mars mission will thus require 180 kW of solar power. This is the solar power that will be needed throughout the mission; including Mars were the solar irradiance is 56% less. Since panel performance metrics such as specific mass are scaled for Earth irradiance, the solar panel system mass for FDR was scaled up by a factor of 2.25 to 2 MT for the aforementioned solar panels with an Earth α of 200 W/kg.

As was described earlier, the Fusion Driven Rocket is comprised of main liner compression coils as well as coils to create a divergent magnetic field at the exit. The mass of these coils is

estimated based on them being high strength aluminum with the appropriate cross sections to be structurally sound, and capable of handling the required currents and impulsive loads. This resulted in a total mass of 0.5 MT. These coils will certainly be fabricated taking advantage of modern, lightweight, high field structural materials such as SiC-SiC composites and other materials suitable for a neutron and space environment. The conservative estimate however provides for margin. Certainly carbon composite structures would also be used to provide rigidity to the coil assemblies.

A thermal management system will also be needed. This system will most likely consist of a working fluid that will be pumped through the high heat flux components such as magnetic coils and power electronics. The fluid will be radiated through space radiator panels. Detailed MCMP calculations of the neutron, gamma and particle physics are underway. With a more detailed understanding of the energy deposition in the various structures, a more in-depth design of the thermal managements system can be made. For now it is assumed that a large fraction of the neutron energy will be absorbed and used in heating of the liner as discussed in Section II. Given the large stand-off, along with the dimensional thickness of most of the structures, the energy deposition from the fusion neutrons will be small. It will be assumed however that 10% of the fusion energy is absorbed and 360 kW of heat rejection is required from the radiators. For high temperatures, space radiator specific mass of 1 kW/kg is quite conceivable.[18] For this case study, due to the uncertain nature of the heat load to the engine subcomponents, a design margin of a factor of three was added. As a result 1.1 MT was allotted for the thermal control/heat rejection system.

In addition to the liner compression mechanism, the Fusion Driven Rocket requires a fusion plasma. The mass of the apparatus required for the generation, translation and injection of the FRC plasmoid must be included. The mass of this system is based on that employed in laboratory devices. Such a system will not be that dissimilar to the one to be used in the validation experiments to be discussed later, and would weigh no more than 500 kg. At first glance this appears to remarkably small, but it should be recalled that the vast increase in plasma energy required for fusion is being supplied by the liner energy (see Fig. 5), and that the initial FRC energy is only 2.2 kJ.

It should also be noted that even though the fusion fuel (50% deuterium/tritium mix) requires gaseous tank storage, the fuel mass required is insignificant. From the COPERNICUS calculations, the total energy required for the complete trip to Mars and return to Earth requires a total of 69 Terajoules. Each fusion event consumes one triton and one deuteron, and produces 2.82×10^{-12} J so that 2.43×10^{25} tritons and deuterons are required. This amounts however to only 120 g of tritium and 80 g of deuterium fuel for the entire trip.

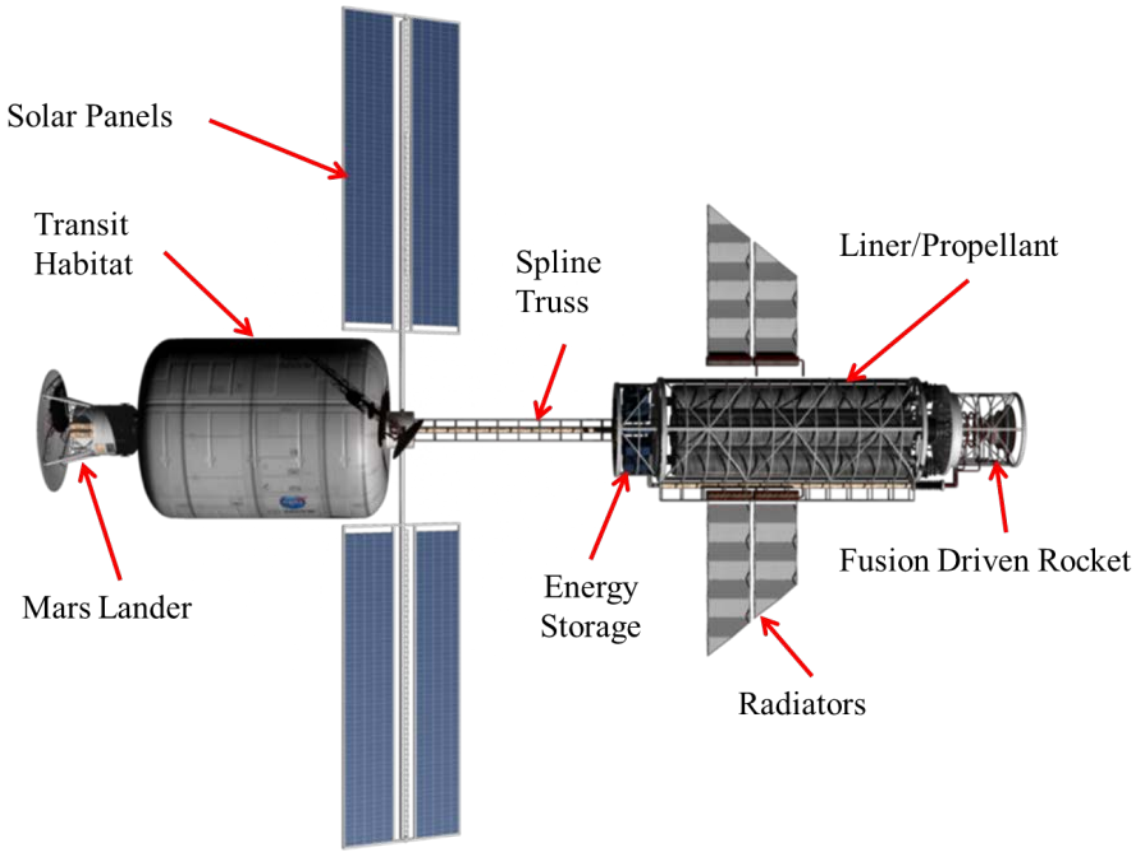

Figure 9. Schematic of the full 210 day FDR spacecraft. *Total spacecraft length is 45 m with a diameter of 5 m. (Diameter does not include the solar and radiator panes, nor the inflatable transit habitat.*

The final two major spacecraft components relate to the propellant mass. The primary propellant for the Fusion Driven Rocket will likely be composed of the lithium in the form of liners. Since lithium is a solid at room temperature, a low mass propellant storage system can be employed with a minimal tank mass fraction. For the purpose of this study it was assumed a constant tankage mass of 100 kg. The propellant feed mechanism on the other hand will require

more mass. This device is responsible for assembling and injecting the liners into the magnetic coils before each thruster firing. The optimum method is clearly one that requires the least amount of complexity on orbit, therefore it is assumed that the liner material will be completely fabricated to the required specification on earth and then loaded on to a roll. These rolls would then be used to form the liner hoops that would be guided mechanically, and injected electromagnetically at low velocity into position under the driver coils prior to driver coil activation. This method would also allow for layering of material within the liner to optimize for lower Ohmic losses, better neutron energy absorption and liner stability. While the envisioned process appears straightforward, a large mass budget of 1.2 MT is specified due to the lack of a detailed assembly design at this point in the design.

The spacecraft structural components include all of the remaining subsystems normally included in a spacecraft design. This includes fairings, support structures, communication systems, data handling ACS, and battery power system. An important aspect of the support structure is a shock absorbing system that interfaces the FDR with the spacecraft structure. The total mass for the spacecraft structure is therefore given the largest mass budget of any subcomponent in this analysis at 3.4 MT. In an attempt to be conservative, an additional margin of 20% for the entire spacecraft mass budget was included in addition to the margin and de-rating factor discussed for individual components. As reflected in Table 6, all of these components result in a spacecraft dry mass of 15 MT. With the 63 MT payload and the 57 MT of lithium propellant, the total IMLEO mass is 134 MT. It was clear in performing the analysis that there may be several areas where there are potentially large mass savings. Possibly the largest being the payload taken from DRA 5 which had a much longer Martian stay. The Apollo command and service modules together weighed only 30 MT. Given newer materials and greater knowledge of the space environment, a much smaller payload mass for the 30 day Martian sortie mission is envisioned as the design is refined. With the smaller payload, the performance metrics of gain and efficiency for the FDR can be less demanding, while still maintaining the total spacecraft mass at 130 MT or less for the 210 day mission.

Details of the Fusion Driven Rocket are shown in Fig. 8. This schematic shows all the major components of the engine at their relative scale. The engine is approximately 3.4 m in length from shadow shield to the end of the engine truss. The engine truss acts to support the 3 main compression coils as well as the magnetic expander. An open truss design was used to create the

largest possible open area as well as to reduce weight. This open area allows for un-captured neutrons to escape the engine without causing additional heating or activation. The truss is 2.25 meter in diameter and is attached to the shock absorber plate. This plate transfers the shock from the pulsed fusion reaction to the rest of the spacecraft. This helps reduce or eliminate structural vibration especially on sensitive subcomponents such as the solar and radiator panels.

The lithium-based propellant is stored on 1.6 meter diameter spools, 9 m in length. Each spool would weigh approximately 9.7 MT. Six spools are arranged azimuthally around a seventh central spool for a total propellant mass of 68 MT of propellant. A good packing fraction is produced by this arrangement, and it also provides for all of the material to fit within a 5 m diameter saddle truss. This packing arrangement also affords additional radiation shielding, although adequate shielding is obtained by thick, permanent, graphite composite shields placed adjacent to the FDR. This shield placement also acts as a shadow shield for all of the spacecraft components including solar panels. A saddle truss was employed to facilitate refueling and reuse of the FDR spacecraft. It also provides for the option of a propellant or equipment drop for an even faster 90 day round trip Marian mission (30 day transit with a 30 day stay). This mission would likely require fuel pre-deployment at Mars.

The heat rejection radiator system is also attached to the saddle truss. They are approximately 5.2 m wide and 7.7 m long with a surface area 120 m^2. The radiators have been profiled to stay within the shadow shield to limit neutron exposure. Located at the forward most end of the saddle truss is the energy storage and electronic components to power the main compression coils as well as the magnetic field coils. This compartment also contains all of the power conversion modules and capacitor charging supplies. The power is fed down along a box frame truss on the side of the saddle truss to the FDR in an insulated and cooled stripline configuration. In this configuration, the saddle truss and the attached components can be classified as part of the propulsion system of the spacecraft. It includes the engine itself as well as all the power systems, cooling systems, and propellant. The propulsion system is attached to the rest of the space craft via a 9 m long spine truss. This truss allows more stand off from the propulsion system, reducing the size required of the shadow shield. The spine truss also acts as a good separation point to modularize the spacecraft if required and would provide a location for addition equipment and payload to be stowed or attached. At the forward most end of the spline truss is the main solar panels and the communication subsystem. The solar array is located here to place it well inside

the shadow. Each solar panel is 4.2 m wide and 15 m long adding up to a total surface area of 126 square meters. The Mars Transhab is 8.2 m in diameter and 11 m long and would mostly likely be composed of an inflatable structure. At the very front of the vehicle is the Mars Lander. The spacecraft length is 34 m in total. The component design was carried out mindful of the diameter limits of future planned payload fairings. This of course requires the use of deployable solar and radiator arrays, inflatable habitat, and possibly a compressible spine truss section.

V. FDR Experimental Studies and Future Work

The greatest challenge for the FDR concept is in demonstrating the feasibility of inductively-driven, metal liner compression of the FRC plasma to fusion ignition. An experimental exploration of the liner implosion at a relevant scale and energy was undertaken at the Plasma Dynamics Laboratory (PDL) at the University of Washington to address this challenge. The results are presented here

A. Previous work

The possibility of attaining the very high pressures required for the confinement of a fusion

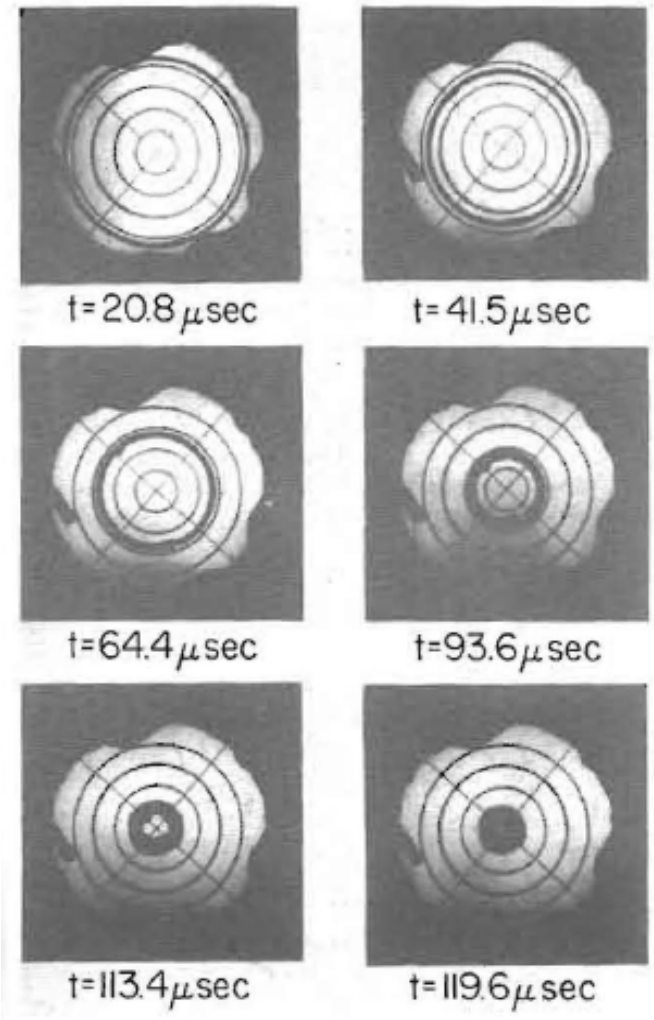

Figure 10. Sequence of images of a backlit aluminum liner implosion (from Ref. 19).

plasm by imploding metal liners to achieve high magnetic field is not new. Inductively driven liners have been used for years to obtain the largest non-explosively driven magnetic fields of up to 610 T.[6] A field of this strength would be considerably more than that required for compression of the FRC to achieve substantial fusion gain. The feasibility of rapidly accelerating inward and compressing thin hoops of aluminum and copper inductively was first demonstrated by Cnare.[5] Since then, the technique has been employed in several experiments to obtain very high magnetic fields in a small volume, which is certainly a result that is highly desired here as well. There are many advantages inherent in this approach, large stand-off from debris, electrical and physical isolation from the target, and magnetic insulation of the driver system from high energy particles to mention a few of the most crucial ones. Another great advantage is simplicity. Even though there is essentially no magnetic field within the liners initially, there is enough leakage flux during the inward acceleration that at peak compression the magnetic field that is trapped inside the now thickened metal wall thermally isolates and magnetizes the target plasmoid.

After the groundbreaking experiments performed by Cnare in the early 1960s, an inductively driven liner similar to those to be employed in the current experiments at PDL, was realized in experiments by Turchi et al.[19] at NRL (see Fig. 10) in the early 70s. Large compression ratio convergence (~ 30:1) was obtained employing a thin (1 mm), large diameter (30 cm), but axially short (7 cm) aluminum liner. Peak magnetic fields as large as 140 T were achieved with excellent symmetry and quality employing only a 540 kJ capacitor bank.

As was noted earlier, the Cnare experiments as well as later experiments, there is a rapidly diminishing liner acceleration after the liner has moved inward roughly 20% of the coil radius. This is due to the drop-off in magnetic force as the liner moves away from the coil which limits the effective radial distance over which it is possible to efficiently maintain significant magnetic pressure. The "stroke length" can be significantly increased by increasing the radius of the driver coil/liner. By increasing the initial liner radius the distance over which one has to accelerate the liners to a given velocity increases. This in turn allows for a significantly lower axial magnetic field to be employed to achieve the same final liner velocity. With the liner's increased

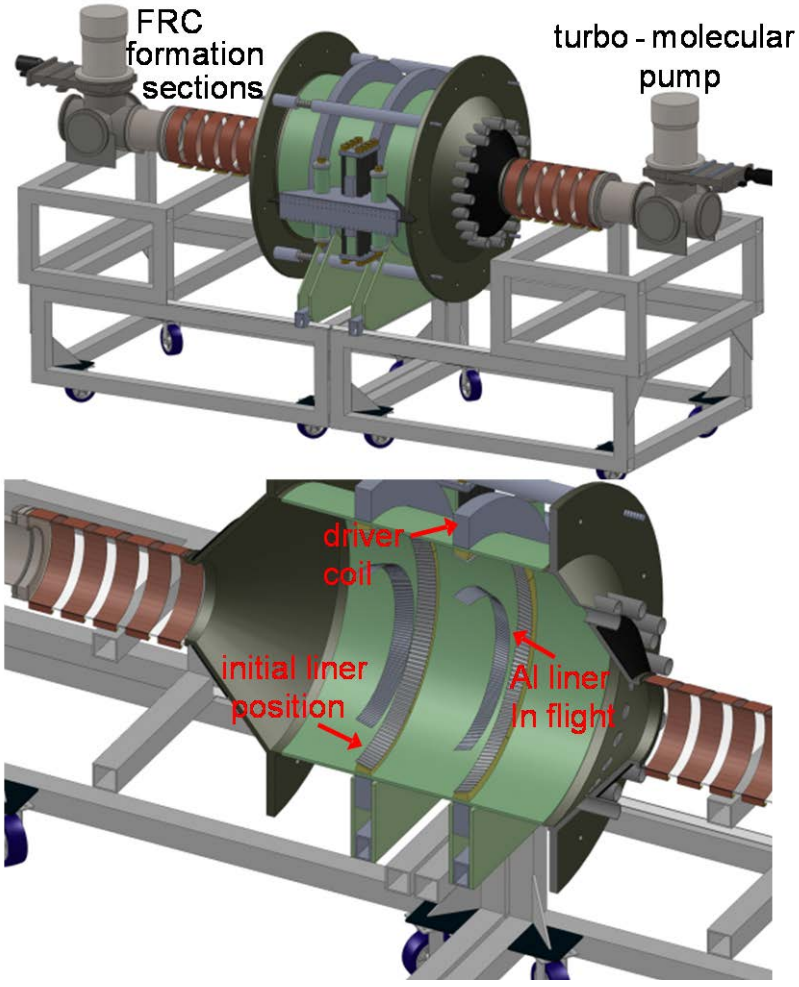

Fig. 11. Fusion Driven Rocket liner compression test bed for liner validation experiments.

circumferential length, the total mass accelerated by the same axial field coil is significantly increased as is the liner kinetic energy.

Driving a liner with as large a radius as envisioned here for the FDR prototype ($r_c \sim r_L = 0.4$ m) has never been demonstrated, let alone an array of liners. This demonstration therefore became the first order of business in the FDR concept validation

B. Inductively Driven Liners at Large Radius

The initial liner tests were conducted at the scale desired for the prototype FDR with the coil radius of 0.41 m. The facility at the UW is equipped with a high voltage (up to ±25 kV) capacitor

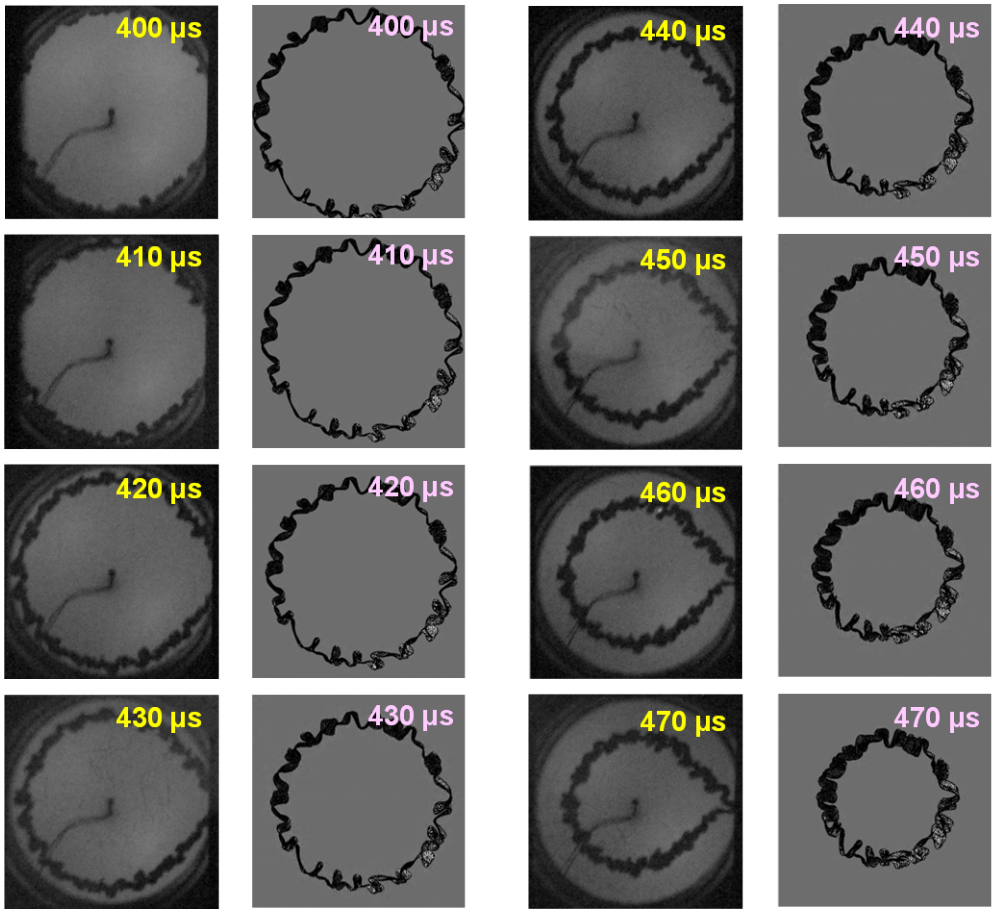

Figure 12. Experimental End-on images (left) and AEDS code results (right) for a 0.4 m radius, 0.16 kg aluminum liner. *The stored energy was 175 kJ (±10 kV, 870 µF). The time refers to discharge initiation. Aperture in experimental images is at 14 cm radius. Internal probe wires can also be seen on axis.*

bank with a stored energy as large as 1.0 MJ. For the initial liner implosion experiments only a

fraction of this bank was employed (870 μF at ± 15 kV for a total stored energy of 392 kJ) to avoid significant collateral damage in the early testing. The AEDS analysis for the prototype FDR with three converging liners (see Fig. 4) was based on the following. It was assumed that each liner was driven by a capacitor bank with an initial energy storage of 335 kJ. The testing of one liner can thus be performed at similar energy to the AEDS calculations for comparison. The first tests were conducted with 0.4 m radius aluminum liners that were 6 cm wide, and 0.4 mm thick with a resultant mass of 0.16 kg. A schematic of the FDR test bed is shown in Fig. 11. The initial driver coils were energized by an array of 48 capacitor modules each consisting of five 25 kV 14.6 μF capacitors. A pair of D size ignitrons in series was employed for the start as well as crowbar switches. They were all triggered simultaneously by a single 25 kV pseudospark switch assuring simultaneity. The modules were divided in pairs connected in series to increase the maximum voltage (nominally ± 25 kV). The 24 module pairs were then connected in parallel to the feedplate of the driver coil via 384 high voltage coaxial cables to minimize the stray inductance (0.07 μH), which was roughly 5% that of the vacuum coil inductance (1.4 μH). The energy coupling efficiency is strongly dependent on having the liner as close as possible to the coil at startup. The liner however acts to shunt most of the coil inductance before the liner moves inward. Making the stray as small as possible is critical to maintaining the magnetic energy in the gap during liner acceleration. In fact it is important that the stray inductance still be small compared to the inductance of the shunted coil. To a good approximation the initial coil-liner system appears as a stripline whose inductance is determined by the liner width w (6 cm), coil-liner gap distance δ_{gap} (1.3 cm), and liner circumference, i.e. L_{gap} (μH) ~ $(2\pi r_c)\cdot\delta_{gap}/w$ ~ 0.56 μH.

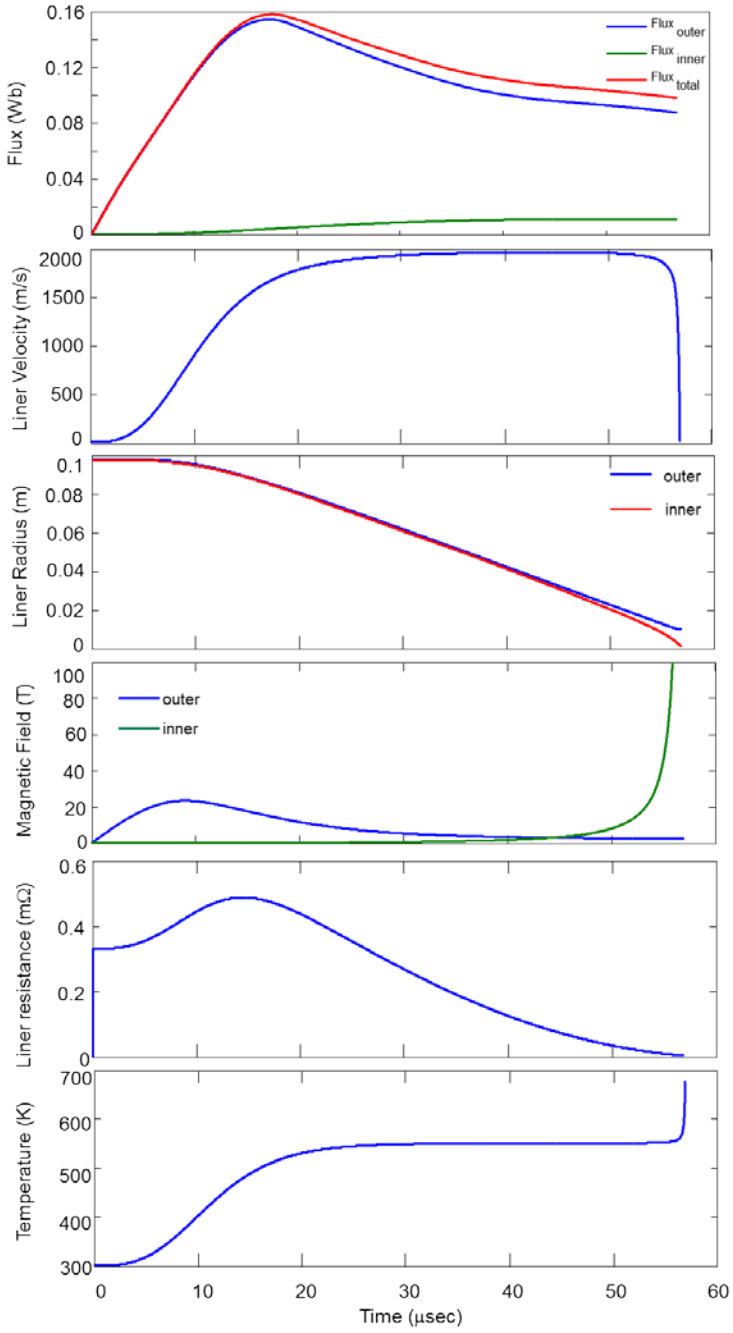

Figure 13. Circuit and liner parameters from 1D model for FRC compression experiments. *Results are for two 10 cm radius, 5 cm wide, and 0.5 mm thick liners driven by 390 kJ bank at ± 15 kV with 70 nH stray inductance.*

The prototype-scale liner convergence tests were performed with aluminum liners in the G-10 vacuum chamber with a driver coil pair as illustrated in Fig. 11. The liners were fabricated from aluminum 1100 strip that was seam welded together and annealed. The weld was ground to

maintain as best as possible the thickness, thermal and resistive properties of the bulk material. The liners were placed inside the vacuum chamber as indicated in Fig. 11. While the vacuum wall increases the gap considerably from what would be employed in a space based driver, it was necessary here to avoid issues with atmospheric interference, and would have been required in any case for the FRC plasmoid formation, translation and liner compression experiments.

The principle diagnostics that were employed to determine liner position as a function of time were several internal magnetic probes on axis, as well as external axial flux and B loops. End-on images of the liner motion were also obtained with a backlit fast framing camera as in the Cnare and Turchi experiments. These images yield detailed information regarding liner uniformity during convergence. In order to avoid confusion, a single liner was installed and only one coil energized. The resultant images from the experiment as well as similar constructed "images" obtained from the 3D AEDS calculation are shown in Fig. 12. It should be noted that these images were obtained for only the final 14 cm of the liner's radially inward travel as the vacuum chamber end cones (see Fig. 11) blocked visual access at larger radius. The AEDS

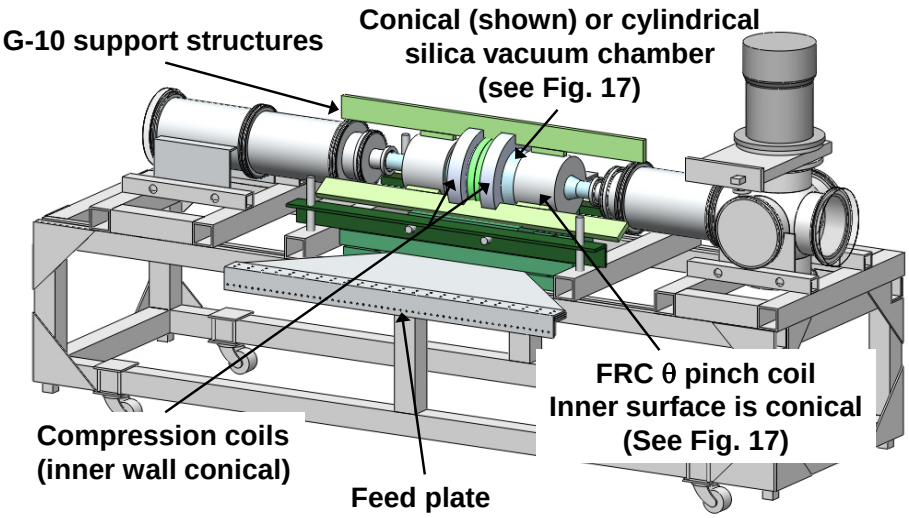

Figure 14. Test bed for 3-D liner compression studies of the FRC plasmoid.

calculations were carried out with the same material, dimensions and magnetic pressure time history as the liners. The near identical results validate the use of the AEDS code for accurately predicting liner dynamics in designing future liner implosion systems. The buckling seen in both

experiment and calculations occurs fairly early in the implosion. It appears that the early buckling serves two useful functions in that it minimizes the energy lost to compressional internal energy in the liners, and, as the liners move inward, the buckles naturally merge together to form a thick, compact stable wall at peak compression as desired. The predicted liner velocity and the actual liner velocity were quite close as can be seen in Fig. 12.

It should be noted that not all of the liner was observed to converge uniformly in the experiment as Fig 12 shows quite clearly. The liner section near the feedplate is retarded as it did not achieve the same inward velocity as the rest of the liner. This was found to be due to the thick aluminum feed plates causing the return magnetic field outside the coil to divert azimuthally around them near the feedplate gap. This significantly lowered the field in the gap at that location. Remarkably, this “tardy” section the liner did not appear to cause any major issues until it was sectioned off late in the implosion. The feedplate does not need to be a thick conductor as all the coil current flows in the first few skin depths (~ 1 mm) of the inner wall. A redesigned thin (7 mm) feedplate backed with G-10 (5 cm) reinforcement produced liner implosions that exhibited no such asymmetry.

Interestingly, virtually all of the damage generated by the imploded liners was created by axial jets consisting of aluminum vapor and, for lower kinetic energy liners, small bits of Aluminum fragments. There was little if any damage to the vacuum wall under the driver coils. The conversion of radial kinetic energy into axial kinetic energy appears to be a natural consequence of magnetized liner implosions. The high energy liners were rapidly heated and melted by Ohmic currents flowing in the liner. As the liner collapses on axis, the magnetic field increases dramatically (see Fig. 13) as the axial magnetic field, which had diffused through the liner during the initial acceleration, is rapidly compressed to very high values. The metal liner

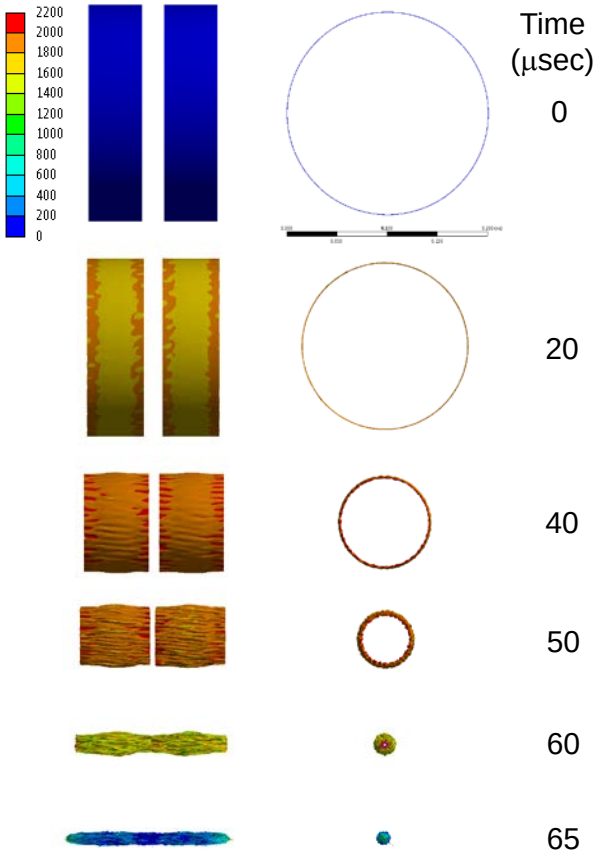

Figure 15. AEDS calculation for the liner implosion for the smaller driver coil. *Initial conditions were set to match the experiment as were the 1D calculation results shown in Fig. 13.Color scale is in units of m/s.*

acts to exclude this field and the rapidly increasing induced current quickly heats, melts and vaporizes the liner as anticipated. However without heating from the fusion event, there is no significant liner ionization. The axial jet-like behavior of the aluminum vapor is thus not a result

of a plasma interaction with the axial magnetic field, but a consequence of the magnetic field on the implosion physics while the liner is still intact and a good conductor. Since magnetic field effects are not yet a direct part of the AEDS calculations, this process is best studied and

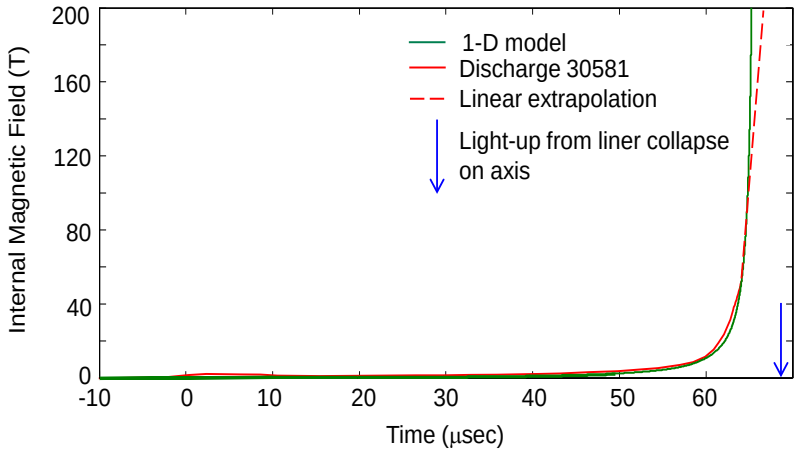

Figure 16. Comparison of the experimentally measured internal B and that predicted by the 1D code. *Code results were shifted in time to compensate for experimental timing delay as well as a somewhat slower axial implosion.*

understood using the 1D liner code that includes the behavior of all the relevant fields, fluxes, Ohmic heating, and circuit behavior.[15] The results for the liners to be employed in the FRC compression experiments are shown in Fig. 13.

C. Inductively driven liners for FRC compression experiments

For the FRC formation, translation, and compression experiments it was decided to employ smaller coils of similar width (5 cm), but much smaller radius (10.3 cm). The primary reason is related to the speed of the liner implosion using the same energy storage, but divided over multiple liners. The aluminum liner thickness was required to be 0.4 mm to avoid both significant Ohmic heating during acceleration, and flux bleed through that would be well in excess of that desired for later FRC injection. While the kinetic energy of these more massive liners could be made sufficient for a fusion gain experiment, the liner velocity given the available bank was roughly 1 mm/μsec. The time required for the liner to converge, assuming an FRC injection at $r_L \sim 10$ cm would be at least 100 μsec. While it is possible to generate an FRC with the requisite lifetime at this scale, it was not possible with the financial resources of the project to fabricate the appropriate plasma sources, coils and pulse power supplies. The smaller coil, with

its associated vacuum components, energy storage, and delivery systems solved this problem, and also allowed for much easier modification and replacement when needed.

The initial tests at smaller radius were conducted employing two straight wall cylindrical coils as in the larger radius setup. The same capacitor bank was used resulting in a driver magnetic field that was significantly increased which acted on a liner whose mass was significantly decreased, thus providing for a potentially much higher liner velocity. There was however some scaling trends that made this less than optimum. While the stray inductance was unchanged, the new coil had a much lower inductance, both in vacuum (0.19 μH) and with liners (63 nH) which was now comparable to the stray inductance which remained essentially the same. The effective coupling was thus significantly reduced. A schematic of the device is found in Fig. 14. Two liners were now employed as this will be necessary for 3D compression of the FRC. Both the 1D code and the AEDS were modified to reflect the new liner system. The results from the 1D code are found in Fig. 13 and the results from the 3D AEDS calculations can be found in Fig. 15. The gross dynamical behavior is quite similar for both codes and compare well with the experimental results. The experimental end-on images also appear very similar to the AEDS calculation although the internal axial probe obscures the liner behavior at touch down on axis.

There is some axial non-uniformity detected in the 3D calculations. This is primarily due to the stronger magnetic field found initially at the edges of the driver coils. The increased radial pressure causes the liner edges to arrive on axis a bit earlier. Experimentally this behavior also caused the internal magnetic probe to be terminated prior to peak field at the center of the liners where the 10 turn, 7 mm diameter pickup coils were located. A comparison of the internal magnetic field observed to that predicted by the 1D code is shown in Fig. 16. The rapid increase of the trapped magnetic field inside the liner is clearly observed for both however the rate of increase is somewhat less than that found in the code. A plausible reason is for this is that the internal cross-sectional area inside the liner is no doubt proportionately larger at small radius due to the azimuthal modulation of the inner wall from the previous buckling. This is clearly observed in the AEDS calculations but would not be reflected in the 1D code. Even with this difference, internal axial magnetic fields well in excess of 100 T are inferred by the measurements as well as both of the codes.

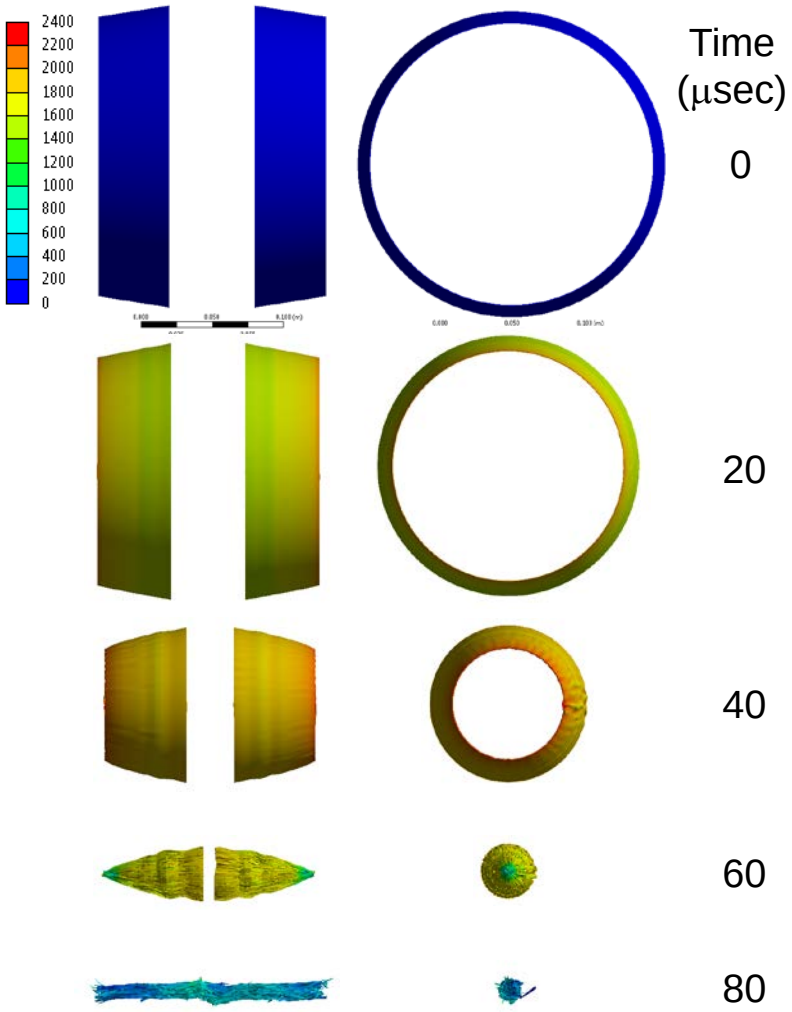

Figure 17. AEDS® calculation for the liner implosion for the smaller driver coil. *Initial conditions were set to match anticipated experimental parameters. Color scale is in units of m/s.*

VI.

D. Experimental Design for the inductively driven liner compression of an FRC plasmoid

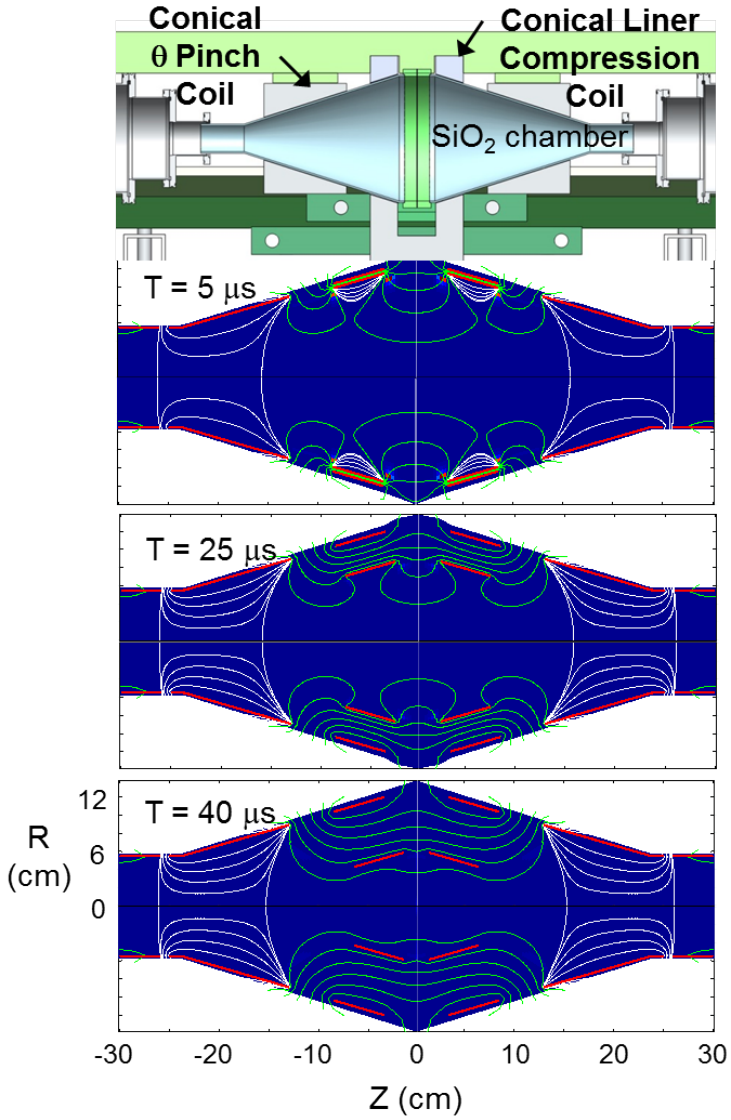

Figure 18. Schematic of FDR validation experiment atop with magnetic flux contours 2D magnetic vacuum solver below. *Liner and coil inner boundaries shown as red lines in calculation.*

Future experiments the analysis and design of the converging liners were studied in preparation for the 3D FRC compression experiments to be pursued as the next step assuming a suitable funding can be secured. The results from the analysis and design studies are outlined in this section. The crucial element that must be demonstrated for the FDR to be a viable propulsion system is the production of significant fusion gain from converging liners. Doing this *in situ* is

the next logical step. By not having the post implosion liner effluvia transported at high velocity out one end makes it possible to perform the key experimental test of the fusion gain in the laboratory. The rest of this section is devoted to a description of the critical design elements and how this test would be accomplished.

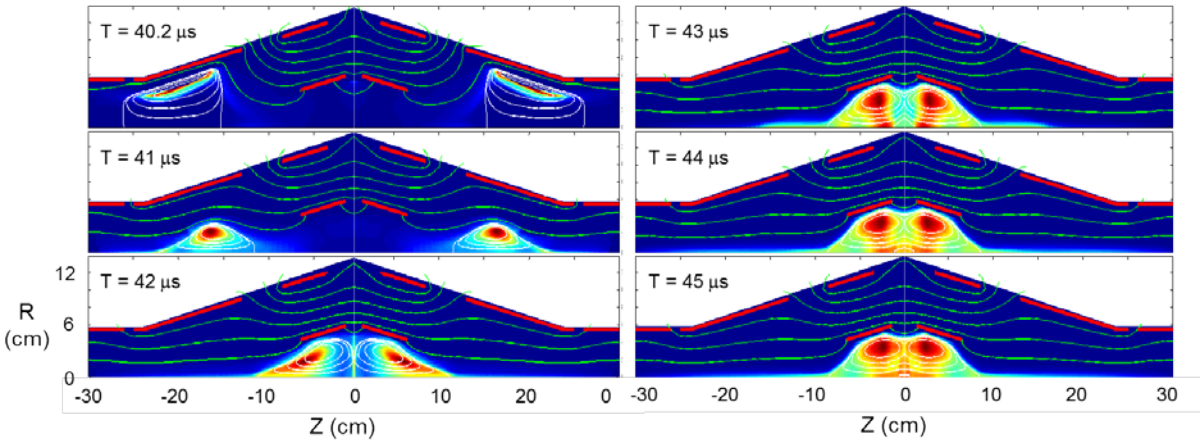

Figure 19. Flux lines and pressure contours from 2D MHD calculation for FRC formation and insertion into converging liners. *Times refer to the start time for coil driver initiation (see Fig. 18). Contours from red (high) to blue (low) are normalized to maximum and minimum plasma pressure at each time.*

In order to create both an axial and radial acceleration of the liners, the driver coil is machined to have a conical pitch to the inner wall. With a matching conical liner the flux conserving nature of both surfaces assures that the accelerating magnetic field is parallel to both thus producing a magnetic pressure component normal to the surface that has both a radial and axial component. As a function of z, the strength of the magnetic field decreases as 1/r toward the large end of the coil and liner. Both the axial and radial components of the force, F acting on the liner scale as $P_B/A \sim B(z)^2/2\mu_0 \cdot 2\pi r_L(z)w$ which therefore scales as 1/r. Since the liner mass per unit length increases linearly with r, the liner acceleration per unit length will scale as $F/m_L \propto 1/r^2$. The cone angle of the liner and coil thus need not be very steep to generate a significant axial acceleration of the liner as well as an increasing pitch to the liner as it moves in radially. This heuristic argument was born out by the AEDS calculations. The ideal convergence would result in the FRC trapped inside the liners with the touchdown of the liners first occurring on the outside ends. The staged arrival of the liner on axis creates a rapid pinching motion axially

inward. In this manner a 3D compression of the FRC is produced at peak compression similar in behavior to that of a shaped charge.

The results from the AEDS calculations for the conical liners are found in Fig. 17 for the experimental setup shown in Fig. 14 which employs the same stored energy and delivery as the straight coils experiments. The cone angle in the driver coils is 10 degrees with the small end the same radius as the straight coils (10.3 cm). The initial axial separation of the liners and driver coils is increased from 2 cm to 7 cm to accommodate the axial motion. As can be seen in Fig. 17, the liners move in axially, closing this gap to essentially zero at termination. The plan is to form and inject the FRCs after the liners have moved into the position found at t = 40 μsec in Figs. 17 and 18. The magnetic environment inside the vacuum chamber at that time is solved for using a 2D magnetic field vacuum solver that correctly treats both coil and liner as flux conservers. A plot of the magnetic flux inside the chamber at three characteristic times during the liner implosion prior to FRC formation and injection is found in Fig. 18. It can be seen that the liners

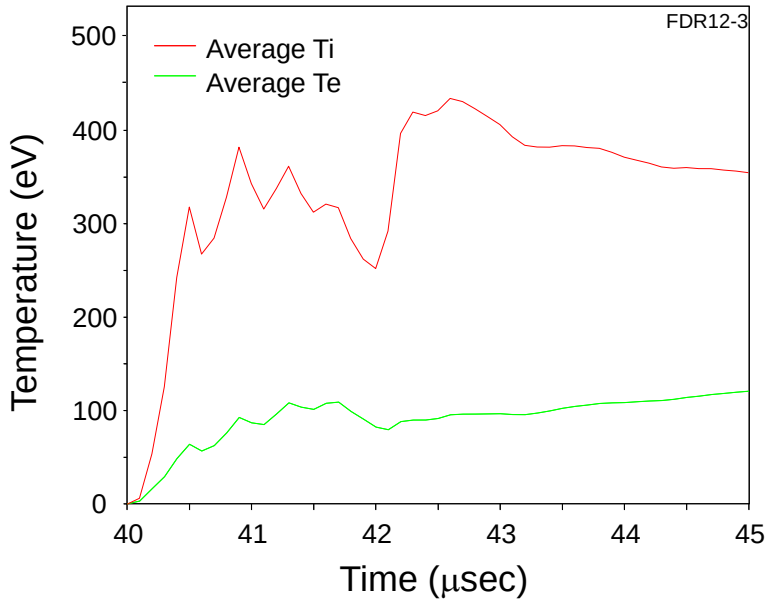

Figure 20. Time history of the average electron and ion temperatures in the FRC from the 2D MHD calculations during the formation and insertion of the FRCs into the converging liners.

prevent any significant flux inside the liner, but that external flux contours extend well beyond the liners once the liner moves in radially. This behavior is actually advantageous as it keeps the FRCs from expanding radially as they exit the conical formation coils and merge, and it tends to

keep the resultant FRC located inside the liner until the fields within the liner increase significantly at small radius. The presence of the large magnetic field radially outside the liners also serves to maintain the FRC radially inside the liners even though there is initially a fairly wide gap at insertion (see Fig. 19).

Detailed 2D, resistive Magneto-Hydrodynamic (MHD) calculations have been carried out to study and optimize the FRC formation and merging in the appropriate geometry for insertion into the two converging liner bands. It appears that for the *in situ* case (no overall translation of the liners), that two liners should be sufficient and even optimal to assure proper axial and radial compression of the FRC. The results from a 2D MHD calculation of FRC merging with two liners for the actual coil and liner geometry to be employed in these experiments are shown in Fig. 19. The start of the FRC formation and injection into the liners is held off until the liner has moved in a little over half way at 40 μsec (see Fig. 18). It requires only a few microseconds to form and insert the FRC. For that short duration, the liners only move inward ~ 4 mm so that the stationary liner assumed in the 2D MHD calculation is a good approximation. A plot of the ion and electron temperature for the deuterium plasma from the calculation is found in Fig. 20. The peak plasma density under the liners at 44 μsec is 5×10^{21} m^{-3}. The axial magnetic field inside the liners before and after FRC insertion is 0.2 T and 1.2 T respectively reflecting the flux compression due to the presence of the high β FRC.

E. Metal liner material and dynamics

The choice of the metal for implosion is important, particularly if it is to be used for fusion applications. As was first pointed out earlier, a material's electrical and thermal properties determine the liner's minimum thickness (mass) for a given liner velocity (energy) when driven by the inductive technique in order to avoid vaporization due to Ohmic heating from the induced currents. The material properties relating to this resistive heating (electrical conductivity, melting point, heat capacity, etc.) can be characterized by a parameter g_M defined by the "current integral" (see Eq. 9) where I is the current flowing through the material cross-sectional area, $A = w \times \delta$, where w is the hoop width and δ is the hoop thickness. The driving force is simply the magnetic pressure ($B^2/2\mu_0$) applied over the surface area of the metal shell facing the coil when in close proximity to the driving coil. The current can be related to the force through Ampere's law which can be reasonably approximated as $B = \mu_0 I/w$. Normalizing to the action constant, g_{Al}

for the vaporization of aluminum from an initial temperature of 300 °K, one finds for the maximum velocity for a given shell thickness δ:

$$v_m = 2.5x10^7 \frac{g_M}{g_{Al}} \frac{\rho_{Al}}{\rho_M} \delta \quad (m/s), \tag{11}$$

where ρ_M is the shell material density. This is usually not a significant issue during FRC compression phase due to the formation of a thick wall at convergence, but the initial thickness should typically be much greater than needed for the characteristic velocities (2 km/s) anticipated. The relatively strong dependence on conductivity favors a good conductor such as Aluminum. A Lithium shell could be especially advantageous in that the initial thin shell could

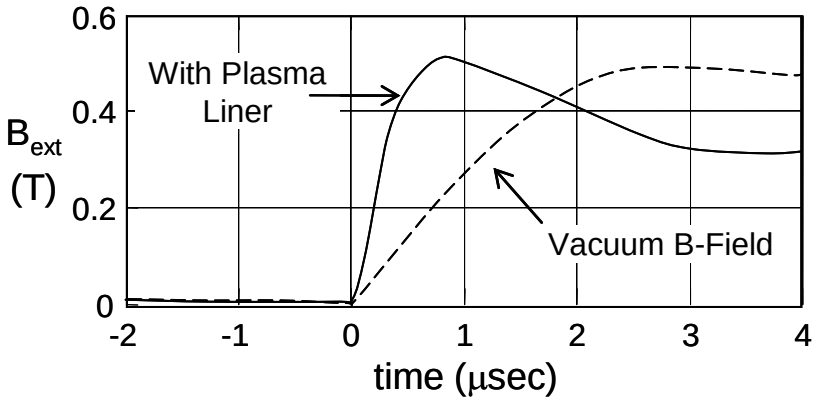

Figure 21: Magnetic field at the compression section midplane measured between the theta pinch coil and the vacuum wall with and without the xenon plasma liner.

be readily extruded for positioning under the coil between pulses. Besides having a low yield strength, Lithium also has other advantages as a liner material. Recall that the ultimate fate of the imploded liner in the presence of significant fusion gain is melting, followed by vaporization and possibly ionization after intense fusion neutron, alpha and radiative heating. Lithium is to be favored for its breeding potential, high vaporization temperature and very low ionization energy. The advantages of Aluminum are also many – inexpensive, easy to handle, high electrical conductivity, and structurally sturdy yet malleable. For the effort proposed here the obvious choice is Aluminum as it was for the initial work on the Foil Liner Compression (FLC)

experiments at MSNW and the Fusion Driven Rocket (FDR) experiments at PDL. Aluminum is also readily available in virtually any thickness, it is safe to handle, and has good vacuum properties. With the use of a thin liner at larger radius there is a hidden benefit in that a significant axial buffer field between the FRC and liner is provided from flux leakage through the liner during the initial stages of acceleration. This external field, B_{ext}, then diffuses into the cylinder with a characteristic diffusion time given by:

$$\tau = \tfrac{1}{2}\, \mu_0\, r_L\, \delta\, \sigma_L \tag{12}$$

where r_L is the initial (inner) cylinder radius, and σ_L is its electrical conductivity. The diffusion of the field is governed by the equation:

$$\tau \frac{dB_{in}}{dt} = B_{ext} - B_{in}\ . \tag{13}$$

The dynamics of the liner implosion are then governed by the equation:

$$M_L \frac{d^2 r}{dt^2} = \left(\frac{B_{in}^2}{2\mu_0} - \frac{B_{ext}^2}{2\mu_0} \right) 2\pi r\, w \tag{14}$$

where M_L is the liner mass, and w the liner width.

With the initiation of the θ-pinch current the field rises rapidly in the small radial gap between the external coil and the liner as the liner acts to shunt virtually all of the coil inductance. A large driving field is rapidly developed. Striking evidence of this was observed on the Plasma Liner Compression experiment at MSNW[8]. With a close fitting driver coil, the plasma sheath formation at the inner vacuum wall eliminated most of the coil inductance and caused a much more rapid rise in the current as only the stray inductances of the external circuit (cables, switches, and coil-sheath gap) provide the only significant impedance to current flow. The rapid current rise was readily detected by the external magnetic probes positioned radially between the coil and the vacuum tube wall. The drop in field after liner lift-off (~ 1 μsec in Fig. 21) below

that of the vacuum field is a reflection of the energy transfer to the liner which was over 50% in these experiments.

It can be seen From Eqs. (12) and (13) that for a high conductance liner during liner acceleration, very little flux leaks through the liner ($B_{in} << B_{ext}$). With the greater inertia of a solid metal liner, the magnetic field maintains a roughly constant amplitude ($B_{ext} \sim$ const.) during this time with the increase in flux in the gap countered by the increasing gap cross-sectional area. With this assumption, Eq. (14) is now readily integrated. With the liner mass $M_L = 2\pi r_L w \delta \rho_{Al}$ where δ is the liner thickness and ρ_{Al} the density of Aluminum, the liner velocity is:

$$v_L = \left(\frac{r(t)}{2\mu_0 r_L \delta \rho_{Al}} \right) B_{ext}^2 t \quad = 125 \frac{\tau_{1/4}}{\delta} B_{ext}^2 , \tag{15}$$

where the approximation is made that the liner is accelerated at roughly constant field up to the time when the liner has moved inward to $r = 0.8\ r_L$. From a circuit efficiency point of view, this should occur at the point of maximum energy transfer into the driver coil. This will occur at the quarter cycle time $\tau_{1/4}$ of the driver circuit, when the bank is typically crowbarred to preserve the flux in the driver coil. Thus the effective drive time $t \sim \tau_{1/4}$ is determined by the bank capacitance and coil inductance at this time. This determines B_{ext} as the magnetic field energy cannot be greater than stored energy minus the anticipated liner energy which is (2 – 0.6) MJ ~ 1.4 MJ for the energy storage requirements for the driver coils. Equating this to the magnetic energy stored in the annuli of the liners yields a magnetic field $B_{ext} = 30$ T in the gap when the liner has moved inward by 20% of the initial coil (liner) radius of 0.15 m. While this is a large field its transient nature allows for the coil to tolerate the large magnetic force, and well below the yield strength of several structural materials. Employing ANSYS® structural analysis on the coil design chosen for the Inductively Driven Liner Prototype (IDLP) device (see Fig. 22), it was found that coils constructed from 7075 aluminum were sufficient to handle the integrated force during the liner drive without exceeding elastic limits of the material and early fatigue failure from repetitive operation. This is in contrast to smaller flux driven experiments where the field strength employed to drive the liner was greater than 100 T and the drive coil is typically destroyed in the

process.[21] It should be mentioned though that the maximum compressed fields were as high as 730 T.[22] Such high fields however are not necessary for achieving high gain in a fusion context.

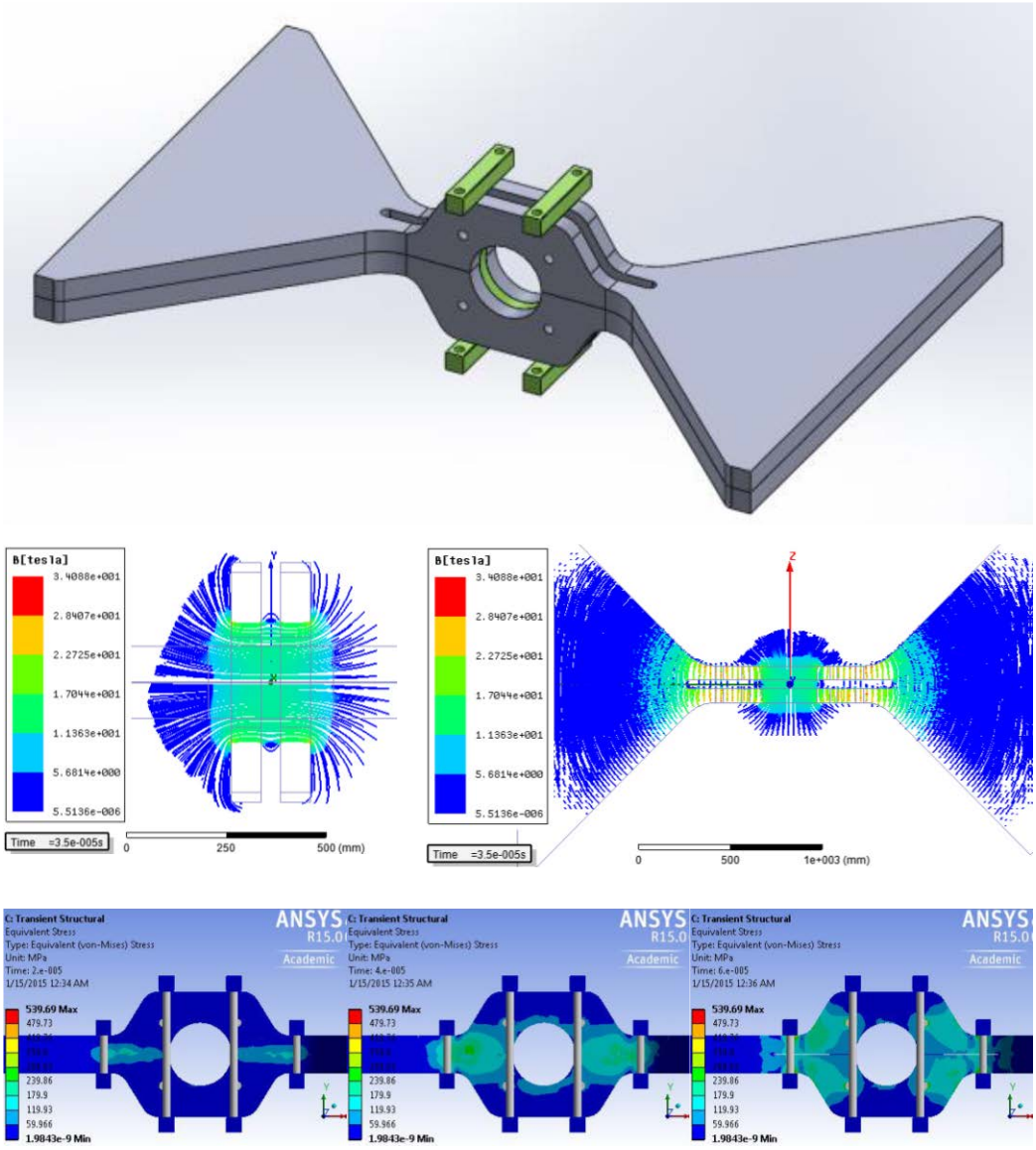

Figure 22. (top) CAD rendering of the 30 cm ID driver coils to be employed on the IDL prototype (feedplate clamps not shown for clarity). (middle) ANSYS Maxwell® calculation of the magnetic field based on the actual driver circuit to be employed. (bottom) ANSYS Structural® calculation the coil stresses at 20, 40 and 60 μsec.

The voltage needed to produce the required field in the gap on the appropriate timescale is given by:

$$V = \omega AB = \frac{\pi}{2\tau_{1/4}} \pi r_L^2 B_{ext} = 48\, kV\ , \qquad (16)$$

While the liner continues to be accelerated, the rate drops dramatically as the area between the coil and liner grows but the capacitor bank energy has been fully transferred to the coil. For the liner to have moved inward 3 cm in 20 μsec under a constant magnetic force implies a terminal velocity of v_L =2.3 km/s. This is consistent with Eq. (15) which predicts a velocity of 2.5 km/s. Given the inevitable Ohmic and internal compressive energy losses, a velocity of 2 km/sec is more realistic and agrees with more detailed analysis. With a nominal liner kinetic energy of 560 kJ the total liner mass can now be determined with M_L = 0.28 kg. These are both consistent with Fig. 23 based on more detailed calculations and modeling. These calculations

Parameter	MSNW-UW IDL	IDL Reactor
Stored Energy, E_s	2.0 MJ	20 MJ
Capacitance, C_s	6.4 mF	43.2 mF
Charge Voltage	25 kV	25 kV
Coupling η (E_L/E_s)	0.30	0.40
Liner mass	0.28 kg	2.5 kg
Peak liner velocity	2 km/s	2.5 km/s
Max. inner B	280 T	400 T
Fusion gain (E_{fus}/E_L)	1.8	210

Figure 23. Basic parameters from the 1D liner model for the future IDL gain demonstration device and those of a reactor base on IDL fusion concept. *Fusion gain was determined using the adiabatic scaling laws for FRC compression and energy conservation. Assuming a simple bounce model for the liner dynamics:*

$$G = \frac{E_{fus}}{E_L} = 4.3\times10^{-8}\sqrt{M_L}\ E_L^{11/8}$$

were performed for the coil geometry shown in Fig. 22 and the results of the 1D calculations for the next step IDLP will be reviewed shortly. Assuming two 7.5 cm wide Aluminum liners implies a liner thickness δ = 0.75 mm (30 mil).

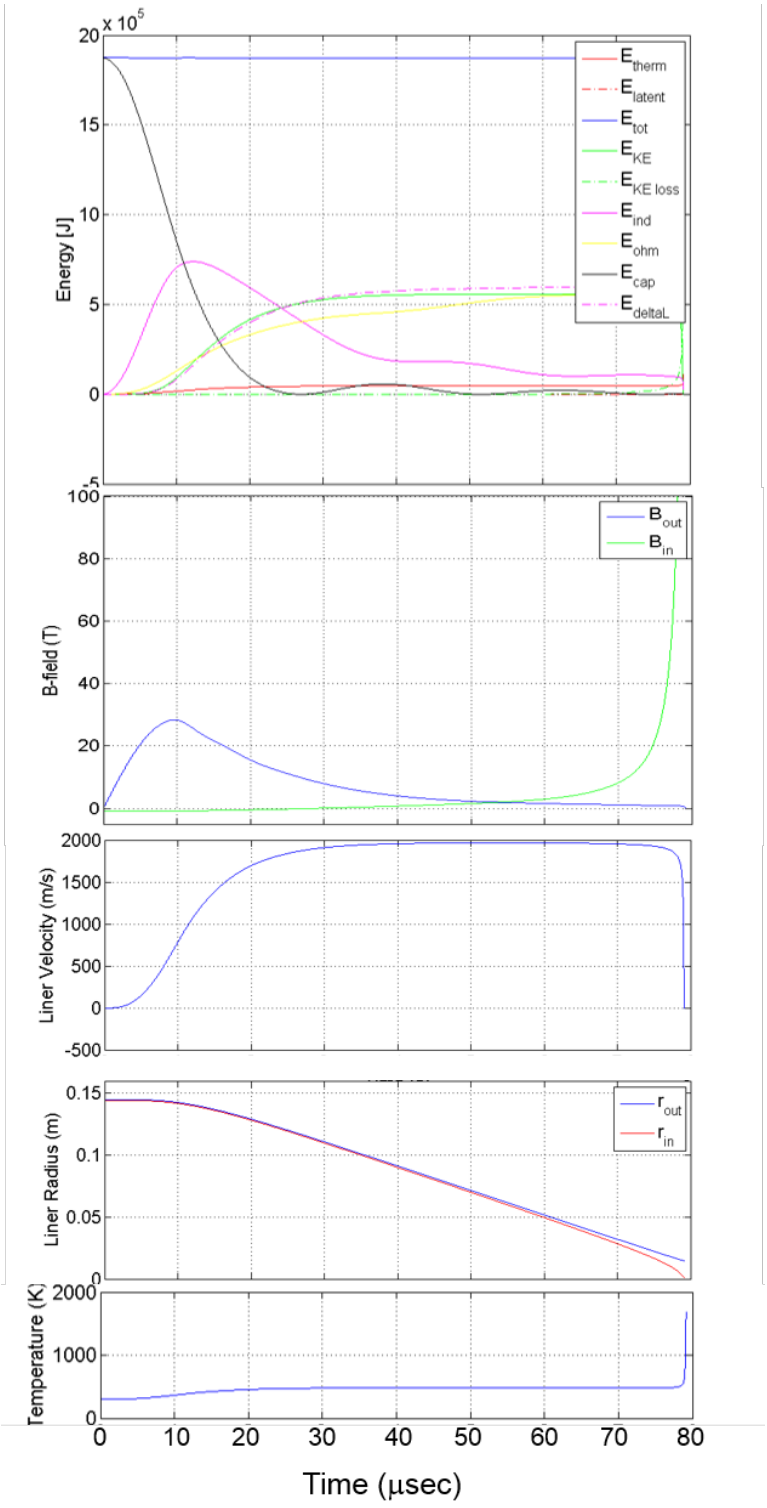

Figure 24. Results from the 1D code showing various liner and magnetic field parameters as a function time for the proposed IDLP.

While this simple analysis is useful for grasping the basic requirements and scaling dependencies, details of the liner implosion process is best studied and understood using the 1D liner code that was developed for this purpose. The model was designed to investigate the dynamic behavior of the liner-driver system where all the relevant magnetic fields, forces, currents, fluxes, Ohmic heating, and circuit behavior were included in order to optimize the design of the IDLP.[15] It is paramount that the liner kinetic energy be determined accurately as this is the major factor that determines the fusion yield. Crucial to this end was the accurate determination of the coupling between the liner and driver coil as the liner moves radially inward. The following procedure was carried out to properly determine this coupling for the actual geometric dimensions of both the coil and liner. The total circuit inductance was first determined from the 3D electromagnetic code ANSYS Maxwell® over a range of liner radial positions and coil currents. The calculations were based on a single drive coil with a 0.15 m inner radius and an axial length of 7.5 cm as proposed here for the IDLP. The actual coil that would need to be fabricated was fully designed and specified in SolidWorks® and imported into ANSYS Maxwell® (see Fig. 22). This code solves for the magnetic field in 3D for a given drive circuit, but is not capable of solving the full dynamic motion of the liners placed within the drive coil. However it can solve for the fields and effective inductances for liners of various radii and location. Maxwell was thus used to determine the magnetic field and radial forces for a given drive current at a specific liner radius. A table of these values was created and used in the 1D model. The ANSYS Maxwell® data was fit with a smoothing spline function, so that the data could be interpolated to the exact liner radius determined by the 1D model.

The circuit equations were based on the actual experimental circuit parameter values anticipated for the Inductively Driven Liner Prototype (IDLP). The results for the liners to be employed in the FRC compression experiments are shown in Fig. 24. Slightly lower bank energy was assumed to account for losses not in the model such as the internal liner compressive stress energy. As can be seen the model supports the conclusions from analytic calculations. It should be noted that the 0.75 mm thick Aluminum liner stays well below the melting point (934 °K) until the induced currents from the final compression of the internal magnetic field (and FRC) rapidly increase the liner temperature. It can also be seen that the coupling efficiency is still 30% while accounting for all resistive losses and circuit stray inductance. The liner also achieves the desired 2 km/sec.

F. Target FRC Formation and Compression

The initial plasma parameters achieved inside the converging liner are critical to obtaining the optimal compressed plasma target parameters. It is also crucial to have sufficient plasma confinement in order to retain plasma energy and inventory during the travel time required for

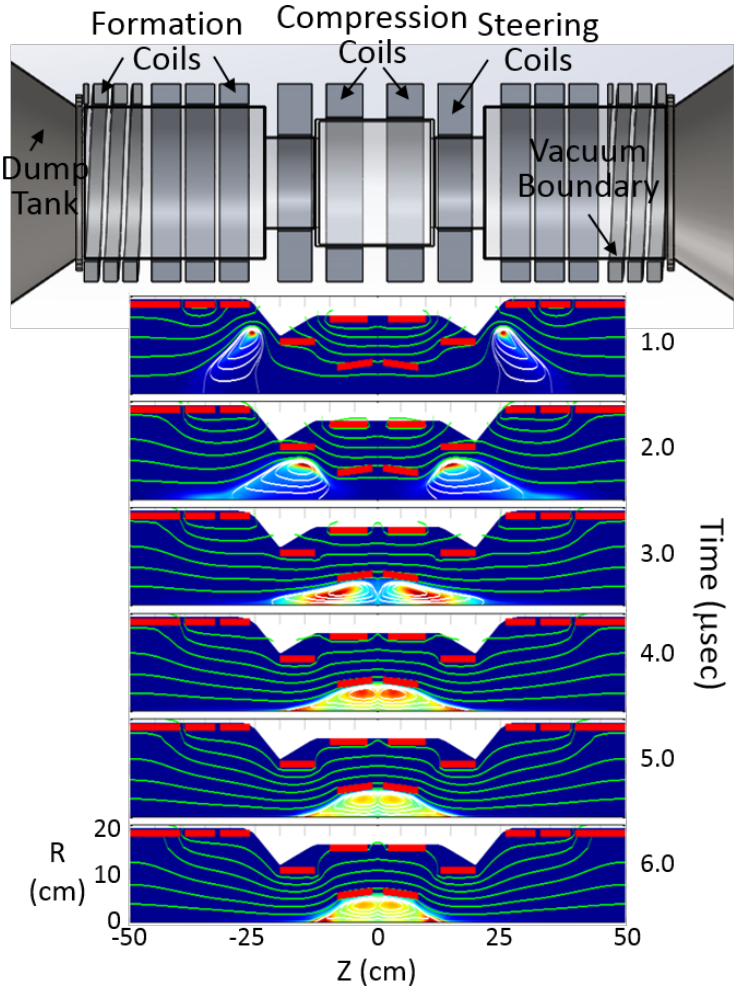

Figure 25. CAD drawing of proposed IDL device with flux lines and pressure contours from a 2D MHD calculation.

the liner to reach peak compression. Even for the fastest practical implosion speeds (~3-4 mm/μs), the time to maximum compression will always be several times the axial ion transit time. Closed-field magnetic confinement is thus a requisite. The FRC can provide this, and at high β as a bonus. The FRC also has the distinct feature that even with liner capable of only a

radial compression; the FRC undergoes an axial contraction during radial compression due to the internal field line tension within the FRC, with the net result being effectively a 2.4D compression of the FRC. Injecting two FRCs and merging them inside the liner considerably shortens the time for compression as this process can be delayed until the liners have been fully accelerated and have moved inward away from the driver coils as is illustrated in the 2D MHD calculations for the IDLP depicted in Fig. 25.

The FRC has been generated over a wide range of sizes temperatures and densities in past experiments. The proper plasma parameters for the merged FRCs are best found by extrapolation

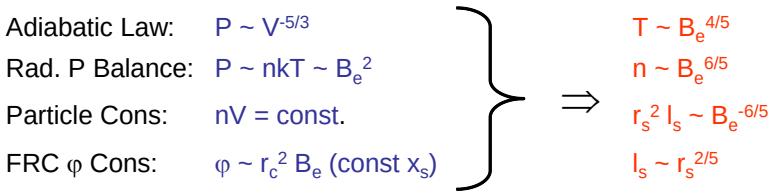

Parameter	Merged FRC	Radial Comp	Axial Comp
Liner velocity: v_L (km/s)	2.0	0	0
Liner radius: r_L (cm)	8	0.8	0.8
FRC radius: r_s (cm)	6	0.6	0.7
FRC length: (cm)	30	12	6
Liner internal B: B_{in}: (T)	2	200	280
FRC Temp.: T_e+T_i (keV)	0.76	15	30
FRC density: n (m^{-3})	1.3×10^{22}	3.2×10^{24}	6.5×10^{24}
FRC energy: E_p (kJ)	8	215	430
FRC lifetime: τ_N (μsec)	213	92	147

Figure 26: (Top) FRC adiabatic scaling laws, and (Bottom) Anticipated FRC parameters from merging, a purely radial, and then a purely axial compression. *In the actual compression the FRC radial and axial compressions would overlap. Number in blue are the target compressed values consistent with initial energy and bank parameters. Numbers in green were determined from Eq. 18. All others are derived from the adiabatic scaling laws stated above.*

back from the desired final state. The compression that is applied by the liners is expected to be adiabatic as the liner compression speed is much less than the FRC plasma sound speed. The key adiabatic relations that govern FRC compression can be found in Fig. 26.

It is easiest to understand the behavior and parametric scaling of the FRC under a 3D liner compression by dividing the process into two steps as is done in Fig. 26. First, it is assumed that the FRC is compressed only radially as it is in the usual Z-pinch liner approach[27] and the manner in which the FRC parameters change is determined fully by the adiabatic scaling laws in Fig. 26. The additional axial compression provided by the liner axial convergence creates a volume change and increases both the FRC average β and radius. The values in the last column reflect these changes from the roughly factor of two axial compression indicated by the AEDS modelling of the liner implosion.

The first column reflects the target parameters of the FRC after the two source FRCs have been merged into the liner compression chamber. It can be seen from Fig. 24 that the optimum time of FRC insertion is ~ 50 μsec, i.e. when the liner radius and internal magnetic field are in the target range determined in Fig. 26. This is well after the liners have reached maximum inward velocity so that the FRC residence time within the liners is considerably shortened. With v_L ~ 2 km/sec (2 mm/μsec) the time to full compression is roughly another ~ 30 μsec from this point. It is worthwhile at this point to consider the FRC confinement scaling that is necessary to assure adequate target lifetime and inventory.

In the first FRC experiments the FRC particle confinement was observed to scale roughly as $\tau \sim r^2/\rho_i$ [26] where ρ_i is the ion Larmour radius at the FRC separatrix. Since the FRC has primarily only a poloidal magnetic field, the plasma pressure at the null must equal the radial pressure exerted by the external field in equilibrium,

$$B_e^2 = 2\mu_0 n_0 k(T_i + T_e), \tag{17}$$

where the zero subscript refers to the value at the magnetic null radius R (= $r_s/\sqrt{2}$). With $T_i \sim T_e$ one has $1/\rho_i \sim n^{1/2}$ inferring that the diffusion coefficient for the FRC is independent of radial scale and has only a positive scaling with density. A trend, it should be noted, that is very favorable for the use of the FRC as a target plasma at high density. Later results on LSX[23] and other experiments indicated further dependences with the FRC elongation, ε, and the ratio of FRC separatrix radius, r_s to coil radius r_c, with this ratio designated as x_s. The observed particle

confinement, stated in terms of directly measured quantities that can be accurately measured across all experiments yields the following scaling[24]:

$$\tau_N = 3.2\times10^{-15}\,\varepsilon^{1/2}\,x_s^{0.8}\,r_s^{2.1}\,n^{0.6}\,. \tag{18}$$

Merged FRCs seem to have improved confinement[20,25] over this scaling by factors of several. As can be seen in Fig. 26 that for the various FRC plasma states, even at maximum compression, the FRC confinement indicated by the scaling expressed in Eq. (18) should be more than adequate without any enhancement. This is particularly true for the compressed state.

The liner stagnation (dwell) time for the liner experiments under consideration is given roughly by the time it would take the liner to reach the axis and back unimpeded or $\tau_D \sim 2r_0/v_L$ = (2)(7.5 mm)/(2 mm/μsec) = 7.5 μsec. The dwell time is thus far less than the predicted FRC particle confinement time. It is in fact similar to the Bohm time so that confinement can be much worse than expected and not be a serious issue. Even if the plasma diffuses to the liner wall, it has been shown[4] that the thermal transport in such a high field region would be insignificant even for a cold boundary and a plasma β greater than unity.

To achieve the final parametric values listed in Fig. 26, one first has to achieve the initial parameters stated in Fig. 26 for the merged FRC. The 2D resistive code Moqui was used to calculate the behavior of the FRC merging in the proposed experimental device and devise an appropriate source for obtaining the desired values. The results from these calculations, and depicted in Fig. 25, do indeed produce the values desired. Since the timescale for formation and insertion (~ 5 μsec) is relatively rapid compared to the motion of the liner during this time (~1 cm), the fixed nature of the coils in the calculation is an acceptable approximation. Part of the theoretical effort of this proposal is to modify the codes to track the motion of the liner as well as the FRC all the way to maximum compression.

It should be noted that the leakage flux through the metal liners during liner acceleration provides for the magnetic cushion between the FRC and liners. The field (flux) magnitude inside the liners can actually be adjusted over a wide range by employing an initial “bias” field capacitor bank that produces a field on a timescale long compared to the liner penetration (L/R)

time. Capacitor energy storage banks such as these are already a part of the existing equipment at PDL and, in fact, have been employed in the experiments for just this type of fine tuning. Now that one has a basic design for all the critical elements required: (1) the appropriate coil driver voltage and energy storage, (2) the appropriate coil the liner materials and dimensions, and (3) the FRC formation and merging sequence, scale and field magnitude to create the proper FRC target, it is worthwhile to see what type of fusion parameters one can expect to achieve with the IDLP device.

G. Fusion Based on Inductively Driven Liner Compression of the FRC

As can be seen from the parameters anticipated from the analysis above, the Lawson triple product for the compressed, 15 keV FRC plasma is:

$$n\tau T_i \sim (6.3\times10^{24})(7.5\times10^{-6})(15) = 7.1\times10^{20}\ \text{keV-m}^{-3}\text{-s}\,, \tag{19}$$

where the value of τ was assumed to be the liner dwell time, τ_D, stated earlier. As the anticipated triple product is roughly that required for breakeven, it warrants a discussion as to how such a system might be evolved to a gain regime that can generate commercial electrical power. Thus the derivation of gain, which was given earlier, is repeated here for continuity and to address the specific requirements for fusion in the context of energy generation alone.

The method for achieving the compressional heating required to reach fusion gain conditions based on the compression of the FRC plasmoid has been described. It is useful at this point to provide a short analysis of the conditions required for fusion ignition for IDL fusion utilizing an FRC target. It will be assumed that it is a D-T plasma. It will also be assumed that the inner shell boundary, and thus the FRC, is ellipsoidal with elongation, ε, is incompressible and that the total radial and axial implosion kinetic energy E_k, is transferred into compression of the FRC and magnetic field with negligible losses. The energy within the FRC separatrix at peak compression is dominated by plasma energy that is in pressure balance with the edge magnetic field B_0, so that one can write:

$$E_L = \frac{1}{2} M_L v_L^2 = 3 n_0 k T_0 \cdot \frac{4}{3}\pi r_0^3 \varepsilon = \frac{B_0^2}{\mu_0}\pi r_0^3 \varepsilon\,, \tag{20}$$

where, as before, M_L is the total liner mass and the zero subscript indicates values at peak compression. The last expression in Eq. (20) further reflects the reasonable assumption that $r_s \sim r_0$ and magnetic pressure balance (Eq. 17). One has then for the fusion energy produced in the FRC during the shell's dwell time τ_D at peak compression:

$$E_{fus} \cong \ 1.2\times10^{-12}\, n_0^2 \langle\sigma v\rangle \frac{4}{3}\pi r_0^3\, \varepsilon\, \tau_D \ = \ 1.1\times10^{-42}\, n_0^2\, T_0^2\, \frac{r_0^4}{v_L}\varepsilon\,, \tag{21}$$

where n_0 and T_0 are the peak density and temperature. The usual approximation for the D-T fusion cross section in this temperature range: $\langle\sigma v\rangle \cong 1.1\text{x}10^{-31}\ T^2$ (eV) was also assumed. Pressure balance (Eq. (10)), together with expressions (13) and (14) yields for the fusion gain:

$$G = \frac{E_{fus}}{E_L} \ = \ 1.73\times10^{-3}\sqrt{\frac{M_L}{l_0}}\,B_0 \ = \ 4.3\times10^{-8}\sqrt{M_L}\,E_L^{11/8} = \ 1.7\times10^{-8} M_L^{15/8} v_L^{11/4}\,, \tag{22}$$

where l_0 (= $2r_0\cdot\varepsilon$) is the length of the FRC at peak compression. The 2nd to last expression is obtained by employing the adiabatic scaling laws (see Fig. 26):

$$E_L \sim B_0^2\, r_0^2\, l_0 \sim B_0^{4/5} \quad \textit{and} \quad l_0 \sim r_0^{2/5} \sim B_0^{-1/5}\,. \tag{23}$$

The final expression in Eq. (15) is obtained by restating the liner energy in terms of the liner velocity and mass. Recalling the target parameters for IDLP, the magnetic field was 280 T, the FRC length was 6 cm and the total liner mass was 0.28 kg for a gain, G ~1.8 from Eq. (15) (this is higher than that found Eq. (12) due to the more favorable coupling assumption made here, i.e. $E_L \sim E_p$). If the same liner velocity is maintained, from Eq. (15) it is clear that a higher gain margin can be obtained by increasing the liner mass alone. The liner energy would increase linearly and thereby increase B_0 and decrease the FRC length. Better standoff would be achieved by simply increasing the scale of coil driver by a factor of 3 (i.e. a 0.9 m diameter liner). The liner mass would also increase by this factor if one were to maintain the same liner velocity and width. From Eq. (16) that the gain enhancement would be $(3)^{15/8}$ = 7.85. This more than

sufficient to reach the conditions where ignition need be considered. It was found by Basko et al[3] that the fuel magnetization allows a significant reduction of the "ρR" ignition threshold when the condition B·R > 60 T-cm is fulfilled. The modification to the usual ICF region for ignition (dT/dt

Figure 27. Feedplate clamping on current FRC liner source experiments at PDL.

> 0) due to the presence of magnetic fields is found in Fig. 1. When the BR parameter exceeds the threshold value of 60 T-cm, the dT/dt > 0 region extends to arbitrarily small ρR. The modification of the ignition criteria for ICF comes about primarily due to the magnetization and confinement of the fusion alphas. Having a large buffer field near the wall to deflect alphas predominately generated in the relatively field-free FRC core creates an ideal configuration minimizing alpha losses as well as eliminating synchrotron radiation. It should be noted that the amount of buffer field is an adjustable parameter in the IDL method. It is set by the vacuum flux inside the liner at FRC insertion. For the IDLP parameters found in Fig. 26 it can be seen that the BR parameter at peak compression is 28 T-cm from just the flux external to the FRC without any consideration of the flux inside the FRC. It would be straight forward to increase the buffer flux at the price of less FRC reacting volume. This of course would be more than offset by gains from ignition. More buffer flux also helps to better insulate the FRC from any wall non-uniformities or disturbances.

H. Liner Fabrication and Stability.

As FRCs have been made with the density, temperature, lifetime and scale (see Fig. 26 and Eq. 18), the risk involved in performing the next-step liner compression of the FRC, comes from consideration of the possible instability of the liner implosion. On the liner side, the greatest risk will come from instability in the plasma wall boundary during FRC compression. In conducting the smallest scale experiments performed at PDL (r_c = 6 cm, r_L = 5 cm), driver magnetic fields as

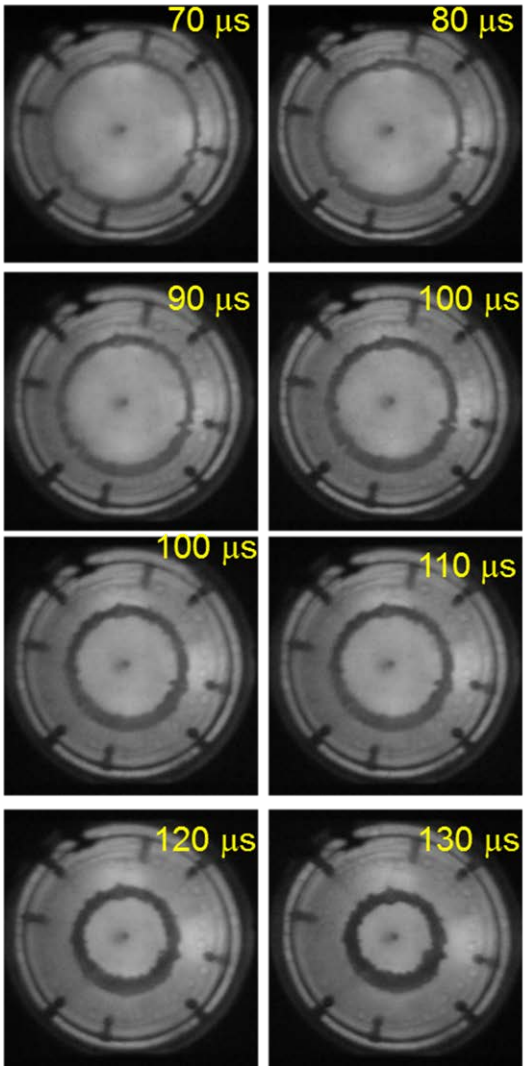

Figure 28. End-on backlit images of two 10 cm radius liners simultaneously imploded on the FDR experiment at PDL. *Compression bank charged to 15 kV (100 kJ).*

large as those anticipated for the 2MJ bank compression in a 15 cm radius coil were attained.

The transiently high magnetic fields do not appear to be a major issue. High current density (and thus magnetic fields) in the feedplates can be an issue. A series of G-10 clamps reinforced by steel beams has proven sufficient in these past experiments (see Fig. 27), and the ANSYS calculations indicate this should be adequate for the IDLP.

The small liners converged with no apparent buckling, as is also observed in other small scale inductively driven liner experiments. Experiments conducted at 10 cm did show some buckling (see Fig. 28), but there was no issues observed at peak field compression (arcs, jets etc.).

The liners were fabricated from Aluminum 1100 strip that was seam welded together and annealed. The weld was ground to maintain as best as possible the thickness, thermal and resistive properties of the bulk material. The liners were placed inside the vacuum chamber under each driver coil. The principle diagnostics that were employed to determine liner position as a function of time were several internal magnetic probes on axis, as well as external axial flux and B loops. End-on images of the liner motion were also obtained with a backlit fast framing camera as in the Cnare and Turchi experiments. These images yield detailed information regarding liner uniformity during convergence. In order to avoid confusion, a single liner was installed and only one coil energized initially. The resultant images from the experiment as well as similar constructed “images” obtained from the 3D AEDS calculation are shown in Fig. 12. It should be noted that not all of the liner was observed to converge uniformly in the experiment as Fig 12 shows quite clearly. The liner section near the feedplate is retarded as it did not achieve the same inward velocity as the rest of the liner. This was found to be due to the thick aluminum feed plates causing the return magnetic field outside the coil to divert azimuthally near the feedplate gap, significantly lowering the field in the gap at that location. This design flaw was readily corrected in later experiments. It should also be noted that these images were obtained for only the final 14 cm of the liner’s radially inward travel as the vacuum chamber end cones blocked visual access at larger radius. The AEDS calculations were carried out with the same material, dimensions and magnetic pressure time history as the liners. The near identical results validate the use of the AEDS code for accurately predicting liner dynamics in designing future liner implosion systems. The buckling seen in both experiment and calculations occurs fairly early in the implosion. It appears that the early buckling serves two useful functions in that it minimizes the energy lost to compressional internal energy in the liners, and, as the liners move inward, the buckles naturally merge together to form a thick, compact stable wall at peak

compression as desired. As one would imagine, all large ratio liners (radius to thickness) are susceptible to buckling. The ability to form very uniform may be important in order to avoid azimuthal non-uniformities at peak compression.

Interestingly, virtually all of the damage generated by the imploded liners was created by axial jets consisting of aluminum vapor and, for lower kinetic energy liners, small bits of Aluminum fragments. There was little if any damage to the vacuum wall under the driver coils, even with liner/drivers as small as 10 cm radius. The conversion of radial kinetic energy into axial kinetic energy appears to be a natural consequence of magnetized liner implosions. The high energy liners were rapidly heated and melted by Ohmic currents flowing in the liner. As the liner collapses on axis, the magnetic field increases dramatically (see Fig. 16) as the axial magnetic field, which had diffused through the liner during the initial acceleration, is rapidly compressed to very high values. The metal liner prohibits the diffusion of this flux on the short timescale of the final implosion, and the rapidly increasing and very large induced current quickly heats, melts and atomizes the liner. However without heating from the fusion event, there is no significant liner ionization. The axial jet-like behavior of the aluminum vapor is thus not a result of a plasma interaction with the axial magnetic field, but a consequence of the magnetic field on the implosion physics while the liner is still intact and a good conductor. Since magnetic field effects are not yet a direct part of the AEDS calculations, how this all unfolds is still not well known. A major part of the theory effort will be directed at a better understanding of this phenomena as it is critical to the design of the eventual reactor.

Much of the work on testing the 3D liner convergence utilizing the inductively driven liner process, was done on smaller radius liners where the liner velocities and coil modifications were more favorable. It was found that two liners, properly driven, were sufficient to produce the desired 3D liner convergence. Experiments were conducted over a range of liner geometries and demonstrated such convergence to compression fields well in excess of 1 Megagauss pressure (100 T) as shown in Fig. 16. The peak magnetic fields that were attained were certainly higher, as B probe failure occurred well before reaching peak fields. This was mainly due to user error (insufficient wire insulation). A much more reliable and accurate system will be adopted for these studies.[28]

An example of the performance of two merging liners initially at 10 cm radius is shown in Fig. 28. The speed of the liner implosion is a critical element for successful compression of the FRC as it must occur on a timescale smaller than the FRC lifetime. This is essentially an Energy Storage and Delivery (ESD) issue. The dramatic difference in liner speed due to differences in stored energy can be readily deduced from the timing differences in Figs. 16 and 28.

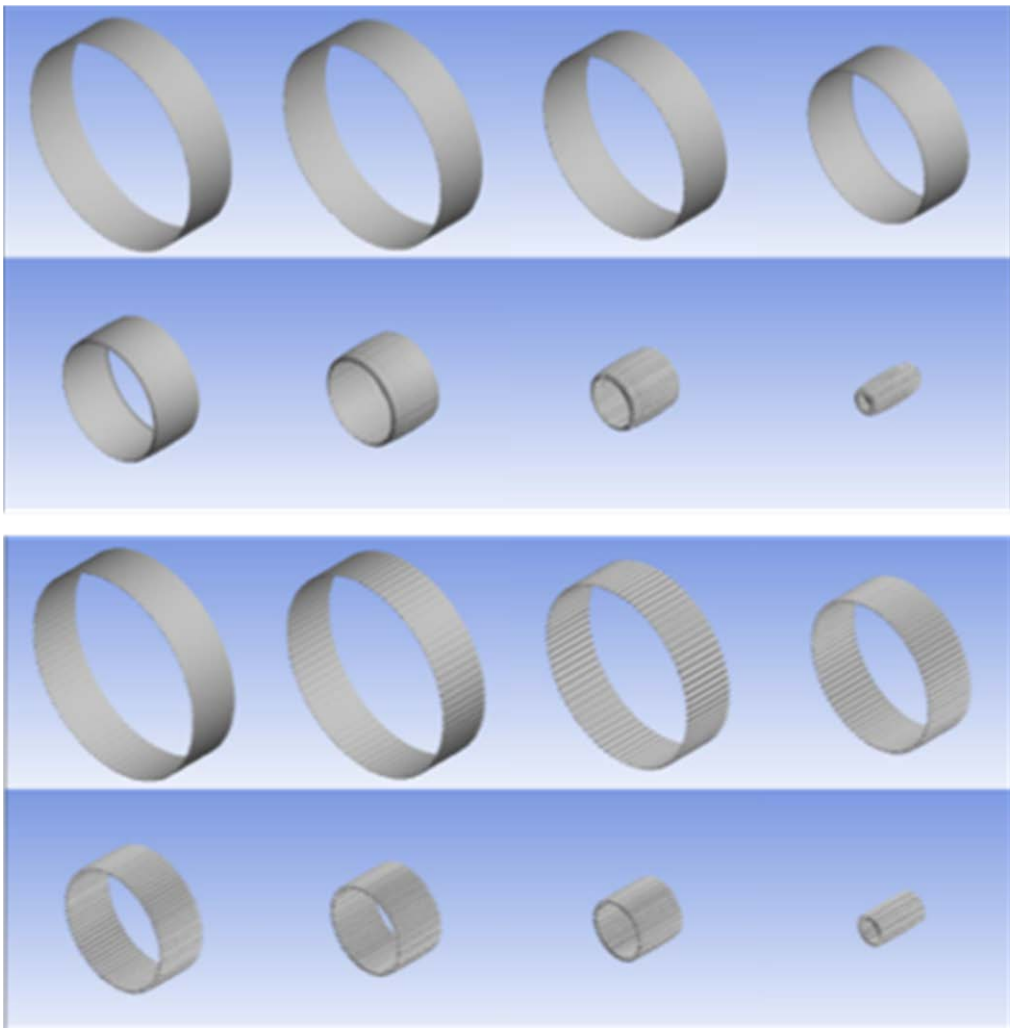

Figure 29. (Top) Evolution of one of the Al solid liners planned for IDLP from an AEDS calculation as function of time (ten μsec intervals starting at 0). (Bottom) Evolution of the same liner but with as function of time for a modulation in thickness with a periodicity of 4.5°.

With inductive drive it is possible to induce an axial convergence of the liners in numerous ways. Several methods have been devised and tested to achieve liner axial convergence from as

simple as a small axial displacement of the liner from directly centered under the driver coil as was done in the experiments, to a tapered coil and liner as in Figs. 18 and 19. The AEDS code has been found to give accurate representation of the liner physics in 3D. The method to be employed in the next step experiment, the use of a steering coil proved to allow for the greatest control and simplicity (see Fig. 25). This also allows for the use of simple cylindrical Aluminum liners that, at least initially, act as independent elements driven radially inward in a symmetric fashion. This also provides for the liner dynamic motion to be described by a simple 1D model through the acceleration phase as was shown in Fig. 24.

It was decided not to leave the potential buckling to underlying imperfections or lack of azimuthal symmetry when it would be only slightly more effort to form the liners with the locations for folding preset. This “pleating” will assure a symmetric folding as the liners converge radially inward with the added bonus of minimal internal stress buildup. The depth of the pleat can be set so that the fold depth is on the order of the final liner thickness minimizing the amount of liner deformation that must occur in compression. Calculations with AEDS were performed for several different liner modulations. It was not difficult to find several that eliminated the arbitrary buckling thereby making the foldup uniform and with reduced internal stress. An example is shown in Fig. 29. It can be seen that the folding begins very early that avoids the eventual buckling instability observed in the case without modulation. The calculation shown had 80 azimuthal periods and was chosen to be similar to the natural buckling frequency observes in the uniform liner calculations. In the liner tests at MSNW it was found that it was possible to form the liner as a roll up with a seam weld made with an ultrasonic welder. This type of weld leaves the material properties (resistance tensile strength, stiffness, etc.) as if it were a continuous piece. The extra material in the overlap is removed by grinding/sanding. This procedure should lend itself readily to incorporating pleats as they can be made prior to welding

There is also the possible issue of liner stability with regard to Rayleigh-Taylor (RT) modes during the deceleration that accompanies magnetic compression. The initial results from the 1D calculation indicates that Ohmic heating from the large induced currents will rapidly bring the inner surface of the liner to the melting point of Aluminum (see Fig. 24). A liquid liner may relax internal stresses and form a better conducing surface but is unstable to RT. It has been shown by Turchi et al. however that rotation of the liner can completely stabilize these modes[29]. Adding a rotational momentum sufficient to accomplish this is actually not that difficult with the IDL

compression method. It should be noted that the liner is free to rotate once it is driven away from contact with the outer wall. With the large ratios of initial to final liner radius foreseen with the IDL, only a relatively small amount of rotational velocity must be induced to be sufficient for stabilization at the small radius where the melting will occur. It was found for a stability that one requires

$$\Omega_0^2 \geq \frac{2}{5\mu_0}\frac{r_0^2 B_0^2}{\rho_{Al} r_i^4 \ln(r_i / r_0)}$$

$$\Omega_0 \geq 146\ rad/\sec \quad (\Omega_i \geq 3.7\ rad/\sec) \qquad (24)$$

The second line reflects the values anticipated for the liners (B_0 = 400 T, r_0 = 0.01 m, r_i = 0.4 m, ρ_{Al} =2700 kg/m^3) at the scale discussed for fusion ignition. The rotational energy acquired by

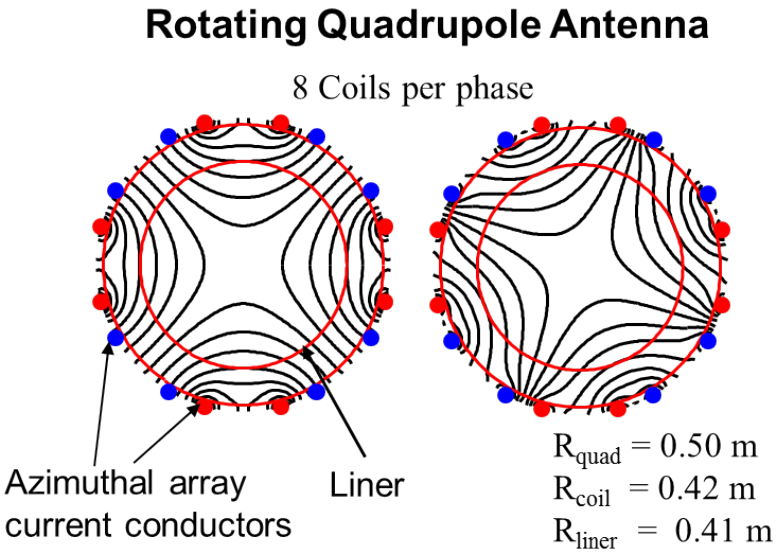

Figure 30. 2 phase coil configuration for rotational stabilization of the liner with a rotating quadrupole magnetic field.

the liner is 2.3 kJ which is negligible compared to the total liner kinetic energy. The rotation can be induced by simply imbedding a slowly rotating transverse magnetic field into the liner prior to

implosion. From force calculations on the proposed aluminum liner, the Rotating Magnetic field (RMF) strength need be no greater than tens of gauss at the frequency of 4 rad/s. An example of the field line structure from a set of axial current rods placed radially outside the driver coils is shown in Fig. 28. FRC rotational stability can also be an issue during the liner compression time. This same quadrupole field has been employed in many FRC experiments in the past[30] and work to do the same here as these fields will be frozen in the liner wall for the relatively short duration of the liner compression.

To obtain a sufficiently predictive theoretical understanding of the liner and plasma dynamics would be extremely useful going forward at the successful completion of the IDLP. This task is inherently a 3D one, and it may be quite feasible to have separately accurate 3D models of FRC plasma and liner. The combining of these two, particularly in regard to the effects of fusion and possible ignition make for a very challenging goal. The risk here is mitigated by employing the most experienced and best FRC modelers together with tremendously powerful and accurate commercial codes. In this way it is hoped that this important task can be successfully completed.

The primary diagnostic of plasma compression and heating will be the neutron count from the D-D fusion reaction. The yield is a sensitive measure of ion temperature. The signal will be analyzed using MCNP codes used in previous FRC experiments.[20] A 16 channel time resolved Doppler spectrometer could be employed to confirm the plasma ion temperature as long as there is a gap between the liners. It is hoped to leave a small gap through the peak implosion to provide more data as to the final FRC plasma state. Through this same gap the plasma density will be obtained from a cross-chamber HeNe laser-based interferometer. With the liner compression of the axial magnetic field and FRC to 200 T, the final ion and electron temperature (the high plasma density will assure that $T_e = T_i$ at that time) is given by the adiabatic scaling law (see Fig. 5) i.e., T_i+T_e (final) = T_i+T_e (initial)$\cdot(B_f/B_i)^{4/5}$ = (500 eV)$\cdot$(60), or T_i = 15 keV which would be well inside the parameter space needed for high fusion gain in a D-T plasma (5 -20 keV). Such a result would clearly validate this approach for obtaining an appropriate fusion plasma for fusion powered propulsion represented by the Fusion Driven Rocket.

Acknowledgments

The authors would like to acknowledge the financial and administrative support from the NASA Innovative Advanced Concepts program (NIAC) and staff. Without their support and encouragement none of this work would have been possible. The authors would also like to acknowledge the expertise, dedication, and craftsmanship of their technical staff: Rorm Arestun (UW), Kyle Holbrook (MSNW) and Chris Pihl (MSNW).

References

[1]Borowski, S. K., et al, "Nuclear Thermal Rockets: Key to Moon - Mars Exploration," *Aerospace America*, Vol. 30, No. 7, July 1992, pp. 34-37.

[2]Williams, C.H., Borowski, S.K., Dudzinski, L.A., and Juhasz, A.J., "A Spherical Torus Nuclear Fusion Reactor Space Propulsion Vehicle Concept for Fast Interplanetary Piloted and Robotic Missions", *35th AIAA/ASME/SAE/ASEE Joint Propulsion Conference*, AIAA 99-2704, June 1999.

[3]M.M. Basko, A.J. Kemp, J. Meyer-ter-Vehn, "Ignition conditions for magnetized target fusion in cylindrical geometry"**,** *Nuclear Fusion*, **40**, 59 (2000).

[4]Drake, R.P., Hammer, J.H., Hartman, C.W., Perkins, L.J., and Ryutov, D.D., "Submegajoule liner implosion of a closed field line configuration", *Fusion Technology*, Vol. 30, pg. 310 (1996)

[5]Cnare, E.C., "Magnetic Flux Compression by Magnetically Imploded Metallic Foils", *Journal of Applied Physics*, Vol. 27, No. 10, pg. 3812, (1967)

[6]Y. H. Matsuda, F. Herlach, S. Ikeda, and N. Miura, "Generation of 600 T by electromagnetic flux compression with improved implosion symmetry"**,** *Rev. Sci. Instrum***. 73** 4288 (2002).

[7]Slough J., et al., "Confinement and Stability of Plasmas in a Field Reversed Configuration", *Phys. Rev. Lett*., Vol. 9, 2212 (1992)

[8]G. Votroubek and J. Slough, "The Plasma Liner Compression Experiment", *Journal of Fusion Energy* **29**, 571 (2010)

[9]Slough J.T., et al "Transport, energy balance, and stability of a large field-reversed configuration", *Physics of Plasmas **2,*** 2286 (1995)

[10]A.A. Harms, K.F. Schoepf, G.H. Miley, D.R. Kingdom, 2002 *Principles of Fusion Energy*, World Scientific Publishing, Singapore 912805, pgs. 267-277.

[11]B. M. Novac, I. R. Smith, D. F. Rankin and M. Hubbard, "A fast and compact θ-pinch electromagnetic flux-compression generator", *J. Phys. D: Appl. Phys.* **37**, 3041 (2004)

[12]Drake, Bret G. "Human Exploration of Mars Design Reference Architecture (DRA) 5.0.", *NASA Special Report*, NASA SP-2009-566, (2009).

[13]Pancotti, Anthony P., John T. Slough, David E. Kirtley, Micheal Pfaff, Christopher Pilh, and George Votroubek. "Mission Design Architecture for the Fusion Driven Rocket." *48th AIAA Joint Propulsion Conference*, 10.2514/6.2012-4113 (2012).

[14]Pancotti, Anthony P., John T. Slough, David E. Kirtley, Micheal Pfaff, Christopher Pilh, and George Votroubek. "The Fusion Driven Rocket." *NIAC Phase II Kickoff Meeting, Hampton*, VA, Nov 2012.

[15]John Slough, Anthony Pancotti, David Kirtley, "Analysis of Inductively Driven Liners for the Generation of Megagauss Magnetic Fields", *14th International Conference on Megagauss Magnetic Field Generation and Related Topics*, paper 4056263, (2012).

[16]J.R. MacDonald, M.A. Schneider, J.B. Ennis, F.W. MacDougall, X.H. Yang, "High Energy Density Capacitors", *IEEE Electrical Insulation Conference*, (2009).

[17]King, Richard R.; Fetzer, C.M.; Law, D.C.; Edmondson, K.M.; Yoon, Hojun; Kinsey, G.S.; Krut, D.D.; Ermer, J.H.; Hebert, P.; Cavicchi, B.T.; Karam, N.H., "Advanced III-V Multijunction Cells for Space," *Photovoltaic Energy Conversion, Conference Record of the 2006 IEEE 4th World Conference on* , vol.2, no., pp.1757,1762, May 2006

[18]Adams, R., et al."Conceptual design of in-space vehicles for human exploration of the outer planets", NASA/TP-2003-212691. November, 2003.

[19]P.J. Turchi, A.L. Cooper, R.D. Ford, D.J. Jenkins, and R.L. Burton, "Review of the NRL Liner Implosion Program", *Megagauss Physics and Technology,* Ed. Peter Turchi, Plenum Press, New York (1980).

[20]John Slough, George Votroubek and Chris Pihl, "Creation of a high-temperature plasma through merging and compression of supersonic field reversed configuration plasmoids", *Nuclear Fusion,* **51**, 053008 (2011)

[21]Y. H. Matsuda, F. Herlach, S. Ikeda, and N. Miura, *"Generation of 600 T by electromagnetic flux compression with improved implosion symmetry"***,** Rev. Sci. Instrum**. 73** 4288 (2002).

[22]D. Nakamura, H. Sawabe, Y. H. Matsuda, and S. Takeyama, *"Precise measurement of a magnetic field generated by the electromagnetic flux compression technique"*, Review of Scientific Instruments **84**, 044702 (2013); doi: 10.1063/1.4798543

[23]A.L. Hoffman, J.T. Slough, "Field reversed configuration lifetime scaling based on measurements from the Large s Experiment", Nuclear Fusion 33, 27 (1993)

[24]John Slough, Samuel Andreason, Hiroshi Gota, Chris Pihl, and George Votroubek, "*The Pulsed High Density Experiment: Concept, Design, and Initial Results"*, J. of Fusion Energy, Vol 25, (2006)

[25]M.W. Binderbauer, et. al. Phys. Rev. Lett., **105**, 045003 (2010)

[26]W.T. Armstrong, et al., Phys. Fluids **24**, 2068 (1981)

[27]Degnan, J.H. Amdahl, D.J. Brown, A. Cavazos, T. Coffey, S.K. Domonkos, M.T. Frese, M.H. Frese, S.D. Gale, D.G. Grabowski, T.C. Intrator, T.P. Kirkpatrick, R.C. Kiuttu, G.F. Lehr, F.M. Letterio, J.D. Parker, J.V. Peterkin, R.E. Roderick, N.F. Ruden, E.L. Siemon, R.E. Sommars, W. Tucker, W. Turchi, P.J. Wurden, G.A., *"Experimental and Computational Progress on Liner Implosions for Compression of FRCs"*, IEEE Transactions on Plasma Science, Vol. 36 Issue 1, pg. 80-91 (2008)

[28]D. Nakamura, H. Sawabe, Y. H. Matsuda, and S. Takeyama, *"Precise measurement of a magnetic field generated by the electromagnetic flux compression technique"*, Review of Scientific Instruments **84**, 044702 (2013); doi: 10.1063/1.4798543

[29]P.J. Turchi, A.L. Cooper, R.D. Ford, D.J. Jenkins, *"Rotational Stabilization of an Imploding Liquid Cylinder"*, Phys. Rev. Lett. **36**, 1546 (1976).

[30]J.T. Slough and K.E. Miller, Phys. Rev. Lett. **85** 1444 (2000).

APPENDIXI

Results of 1D Liner Parametric Study for FDR Fusion Gain Demo

John Slough (MSNW) and Akihisa Shimazu (U. of Wash.)

A 1D liner code, developed for the dynamic modeling of the coil-liner compression mechanism for Fusion Driven Rocket (FDR), was used to study the sensitivity of the overall coil-liner compression performance to variation of FDR parameters. For this analysis, it is assumed that the coil has parallel half-turn geometry with inner radius of 15 cm, turn width of 3 in, half-turn gap distance of 20 mil, and coil spacing of 3 cm. The gap distance between liner outer radius and coil inner radius is assumed to be 0.5 mm. A basic schematic of the parallel half-turn coil is shown below in Fig. 1. The coil-liner system is divided into two following subsections: inner and outer section. The outer section represents the volume between liner and the coil; the inner section represents the volume inside the liner. The external circuit driving the coil-liner compression is assumed to be a simple crowbar circuit with crowbar switch closed when the capacitor bank voltage is equal to ground. A schematic of simple crowbar circuit is show below in Fig. 2.

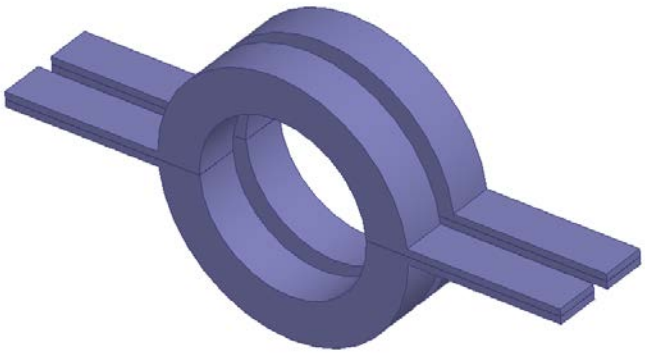

Figure 1. Schematic of parallel half-turn coil. Two half-turn coils are separated by small gap (half-turn gap distance) to complete one coil turn, and two half-turn coil groups are separated by fixed distance (coil spacing) to form two parallel coil turns.

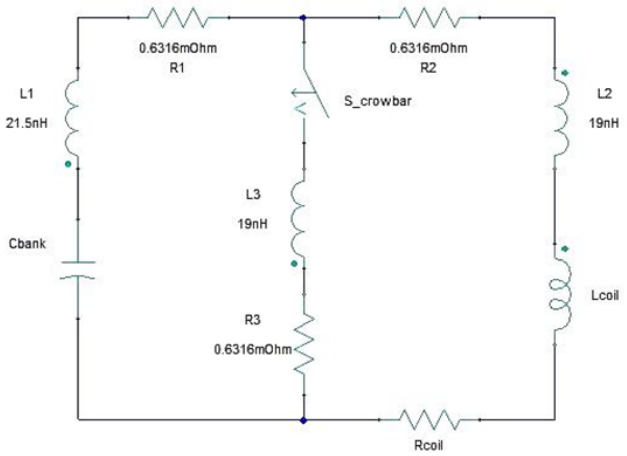

Figure 2. Schematic of simple crowbar circuit

In order to characterize half-turn coil geometry in 1D liner code, ANSYS Maxwell 3D® and Moqui is used to create magnetic field, flux, inductance, and geometry relationship. Moqui is used to generate magnetic field and flux relationship as a function of liner inner radius. Maxwell 3D is used to generate inductance data as a function of liner outer radius. For half-turn geometry, an inductance data for the coil-liner system is extrapolated from a two turn parallel case under assumption that the vacuum system inductance for the half-turn case is $1/4^{th}$ of the two turn parallel case. Liner inductance data is produced directly from Maxwell 3D, by assuming the liners are completely isolated. Due to the 1D nature of the code, axially averaged data is used. More thorough description of the 1D liner code routine is described in Appendix A.

In 1D liner code, the circuit values shown in Fig. 2 are used as a default value for the external circuit. For half-turn parallel case, it is assumed that the resistance is $1/4^{th}$ of the default value shown in Fig. 2 due to change in the external wiring configuration. Half-turn coil resistance is assumed to be 0.125 mΩ, based on the resistance calculated from ANSYS Maxwell 3D. To see the effect of the variation in stray inductances (L1, L2, and L3 in Fig. 2), a dimensionless parameter called Stray Multiplier is used. Stray Multiplier represents the inductance of the circuit as a multiple of the default value. In the 1D Code, it is assumed that all three stray inductors (L1, L2, and L3) all have same Stray Multiplier.

In the parametric study of the half-turn coil, following variation parameters are used: Liner Thickness, Stray Multiplier, Capacitor Bank Voltage, Bank Capacitance, and the Initial Bias Field in the inner section. As a default configuration, liner thickness of 30 mil, stray multiplier of

0.25, bank voltage of 25 kV, bank capacitance of 6000 μF, and initial bias of 0 T are assumed. The thickness is swept from 10 mil to 40 mil, the stray multiplier is swept from 0.0625 to 1, the bank voltage is swept from 15 kV to 35 kV, the capacitance is swept from 3000 μF to 9000 μF, and initial bias is swept from -1.3 T to 0 T.

For the performance comparison between different configurations, following performance parameters are used: Kinetic Energy Efficiency, Ohmic Loss Efficiency, Maximum Theoretical Efficiency, Maximum Liner Velocity, Circuit Crowbar Time, Liner Collapse Time, Maximum Magnetic Field in the Outer and Inner Section, Maximum Liner Temperature, and Magnetic Field in the Inner Section when the Inner Radius of the Liner is at 65% of the Coil Inner Radius. Kinetic Energy Efficiency is defined to be the maximum kinetic energy of the liner divided by the initial bank energy. The Ohmic Loss Efficiency is defined to be the total ohmic loss divided by the initial bank energy. Maximum Theoretical Efficiency is defined to the maximum kinetic energy of the liner divided by the sum of the maximum kinetic energy of the liner and the total ohmic loss. Liner Collapse Time is assumed to be the time when the liner comes to rest and reverses direction. If the liner does not come to rest before the liner inner radius is 1 μm, then the value at 1 μm is used. For Magnetic Field data, the values at the liner inner and outer surface are used.

Liner Thickness Variation:

The result of the parametric study of the half-turn coil with liner thickness variation is shown below in Fig. 3a-3f. A smooth spline fit is used between data points. For liner thickness variation, Stray Multiplier is fixed at 0.25, the Bank Voltage is fixed at 25 kV, the Bank Capacitance is fixed at 6000 μF, and the Initial Bias Field is fixed at 0 T.

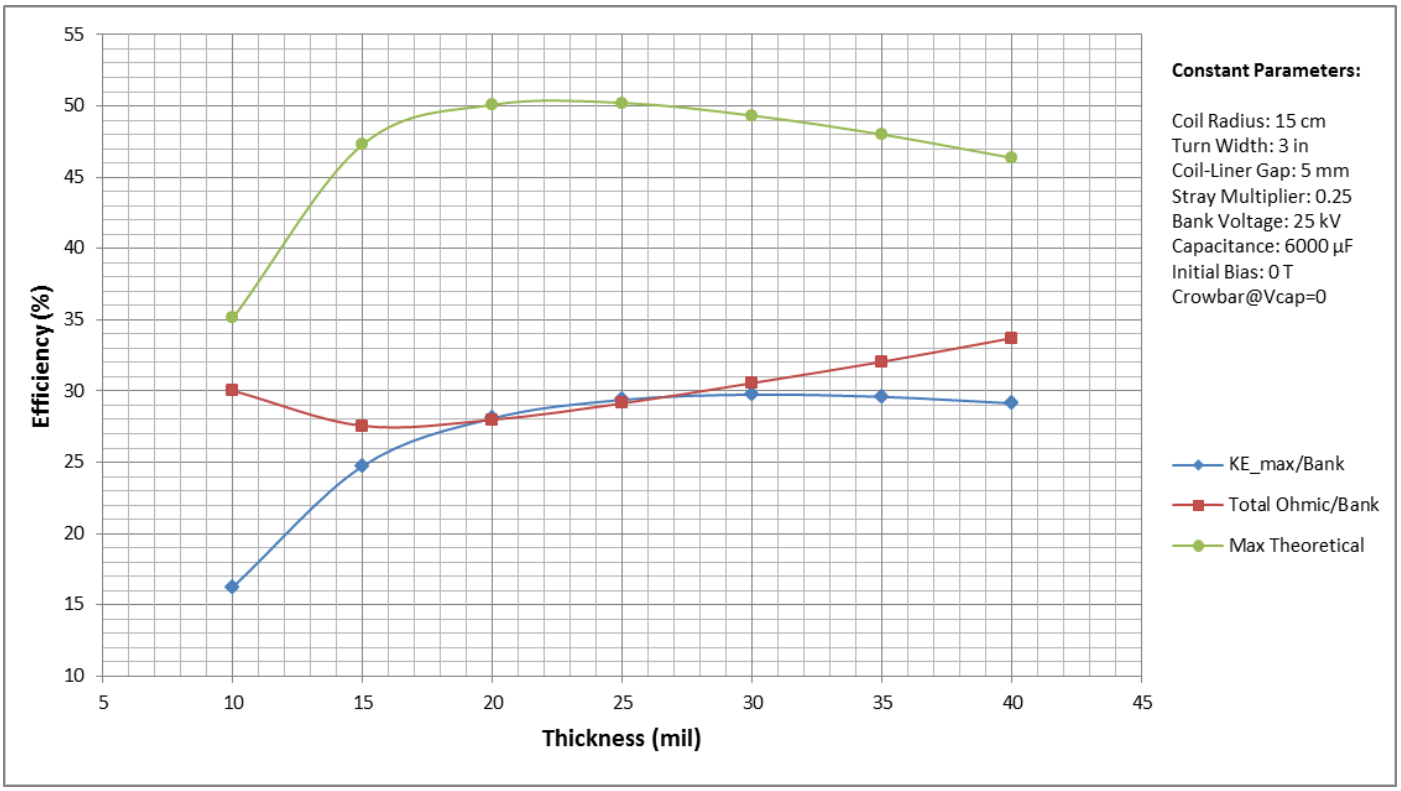

Figure 3a. Plot of Kinetic Energy, Ohmic Loss, and Max Theoretical Efficiencies

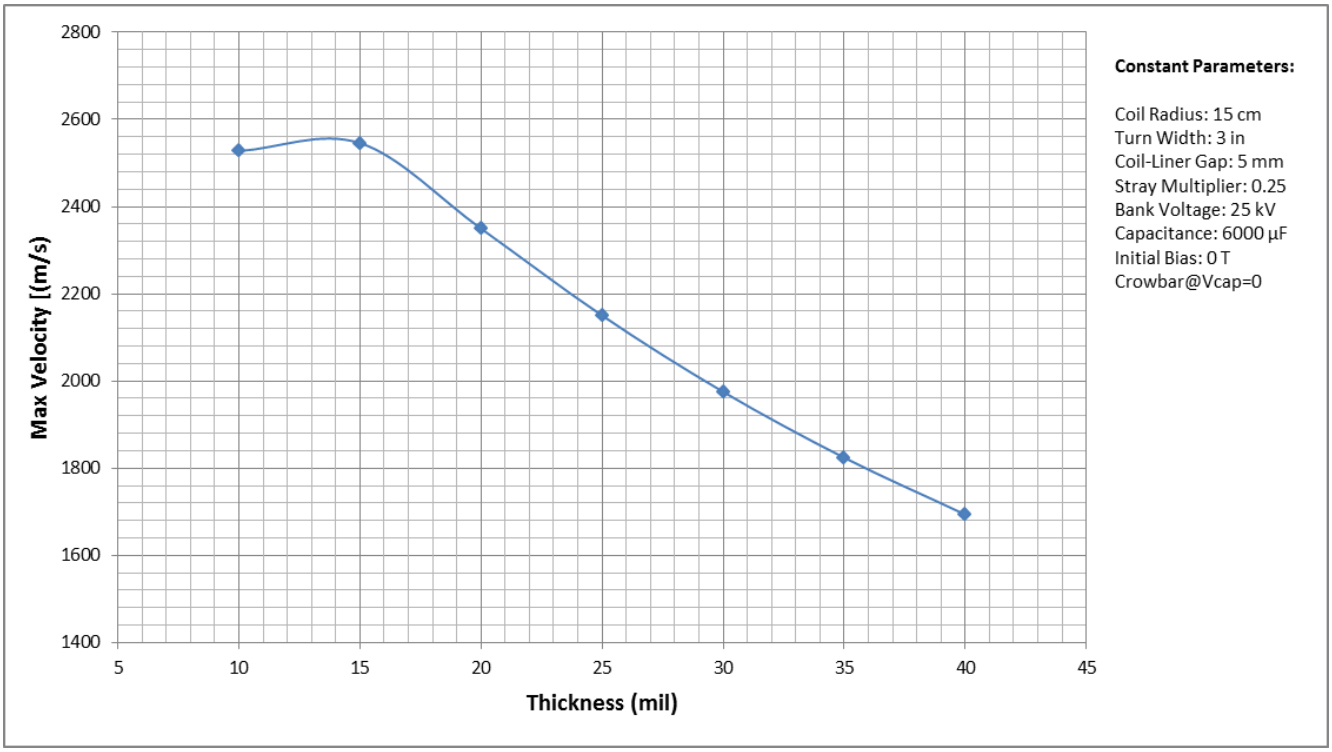

Figure 3b. Plot of Maximum Liner Velocity

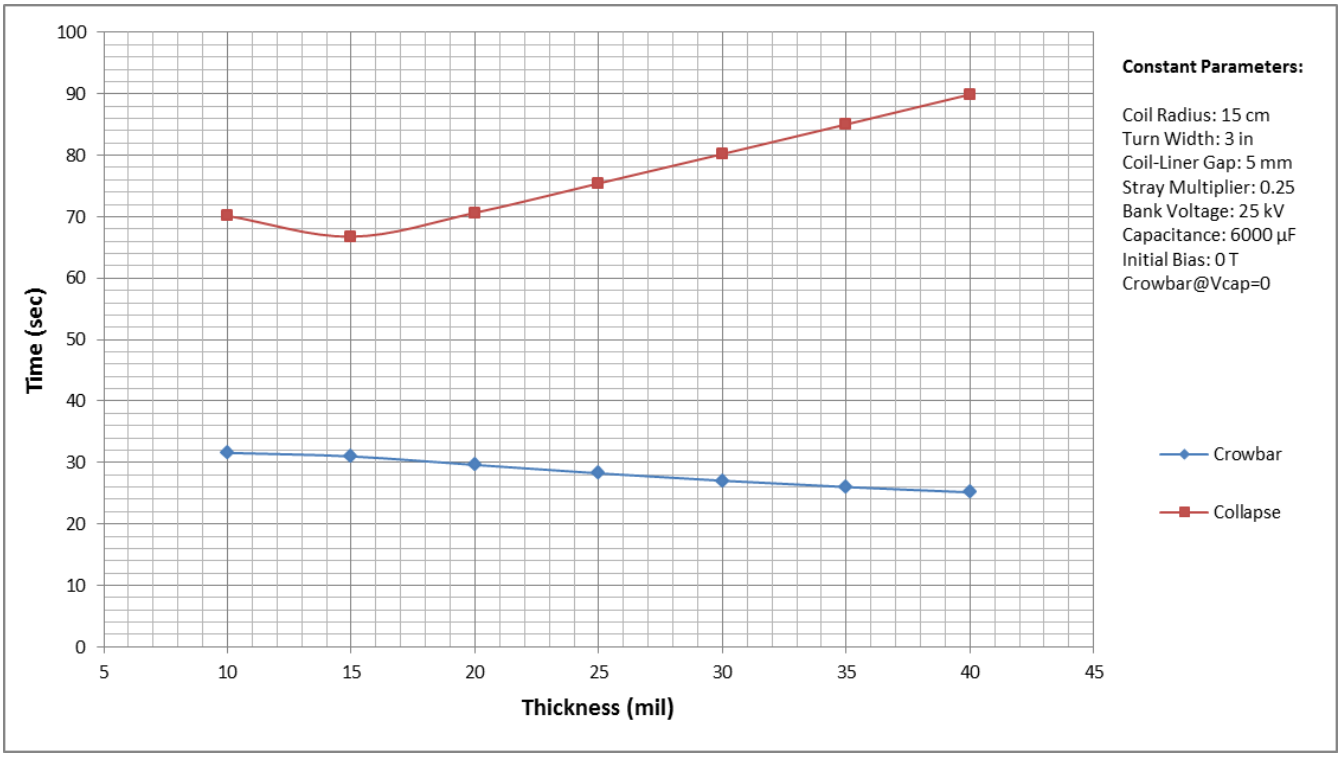

Figure 3c. Plot of Circuit Crowbar and Liner Collapse time

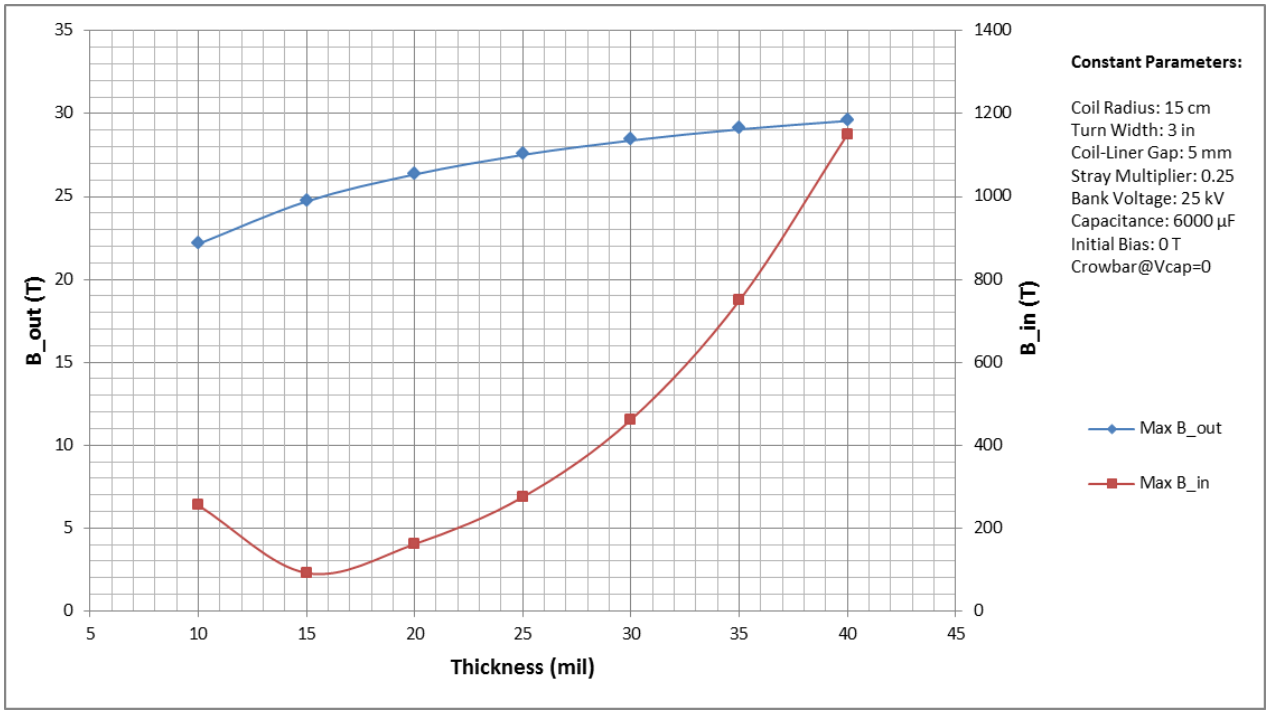

Figure 3d. Magnetic field strength at inner and outer liner surface

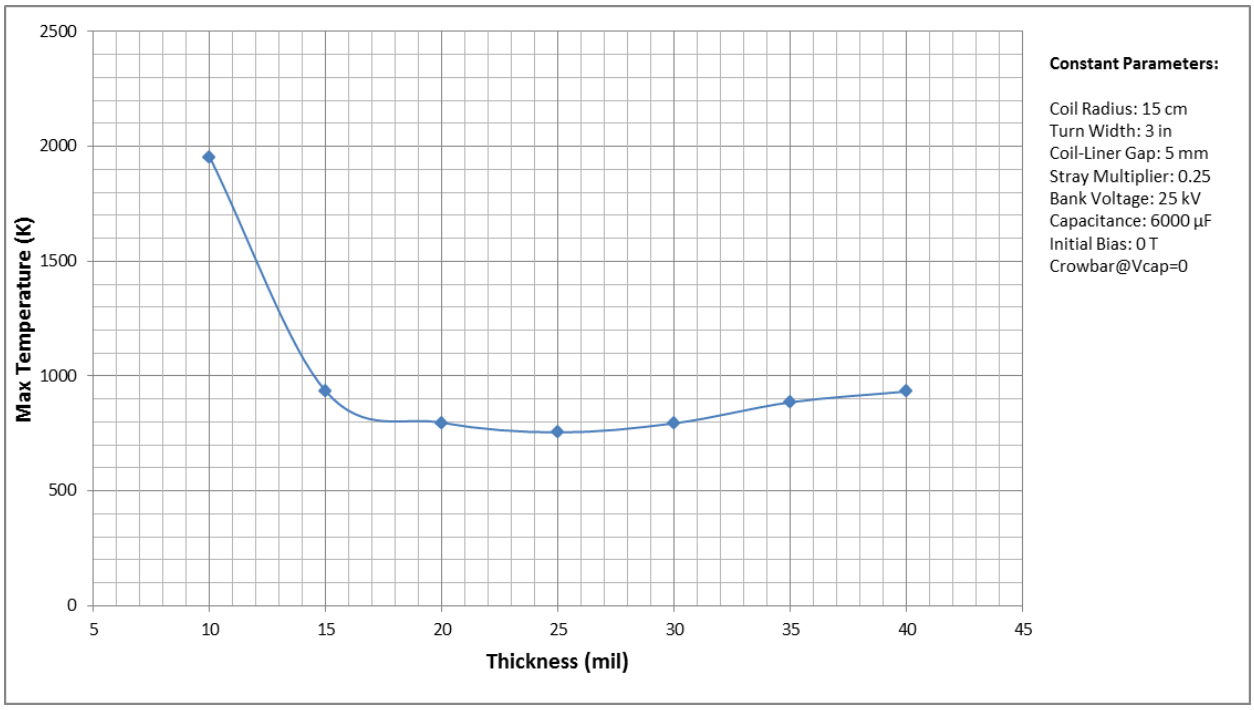

Figure 3e. Plot of the maximum temperature of the liner

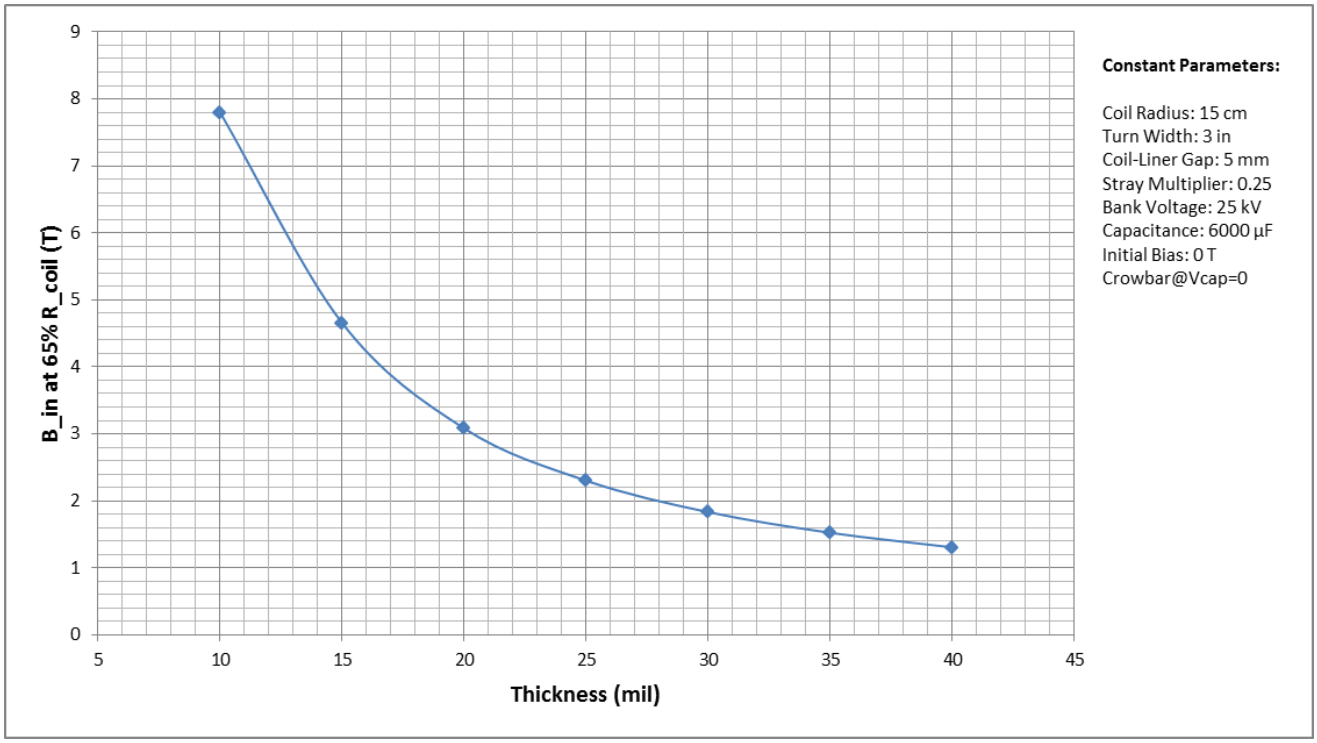

Figure 3f. Plot of the magnetic field strength of liner inner surface at 65% coil radius

Stray Multiplier Variation:

The result of the parametric study of the half-turn coil with stray multiplier variation is shown below in Fig. 4a-4f. A smooth spline fit is used between data points. For stray multiplier variation, Liner Thickness is fixed at 30 mil, the Bank Voltage is fixed at 25 kV, the Bank Capacitance is fixed at 6000 μF, and the Initial Bias Field is fixed at 0 T.

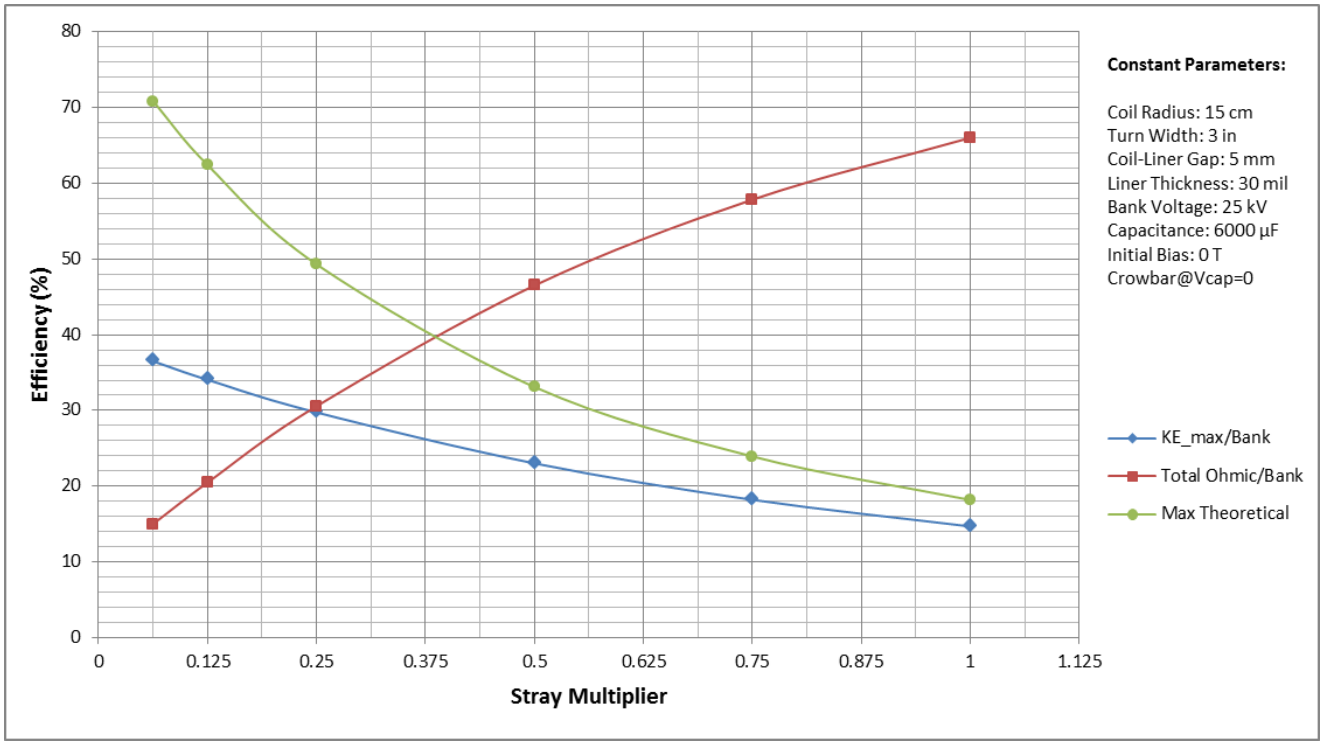

Figure 4a. Plot of Kinetic Energy, Ohmic Loss, and Max Theoretical Efficiencies

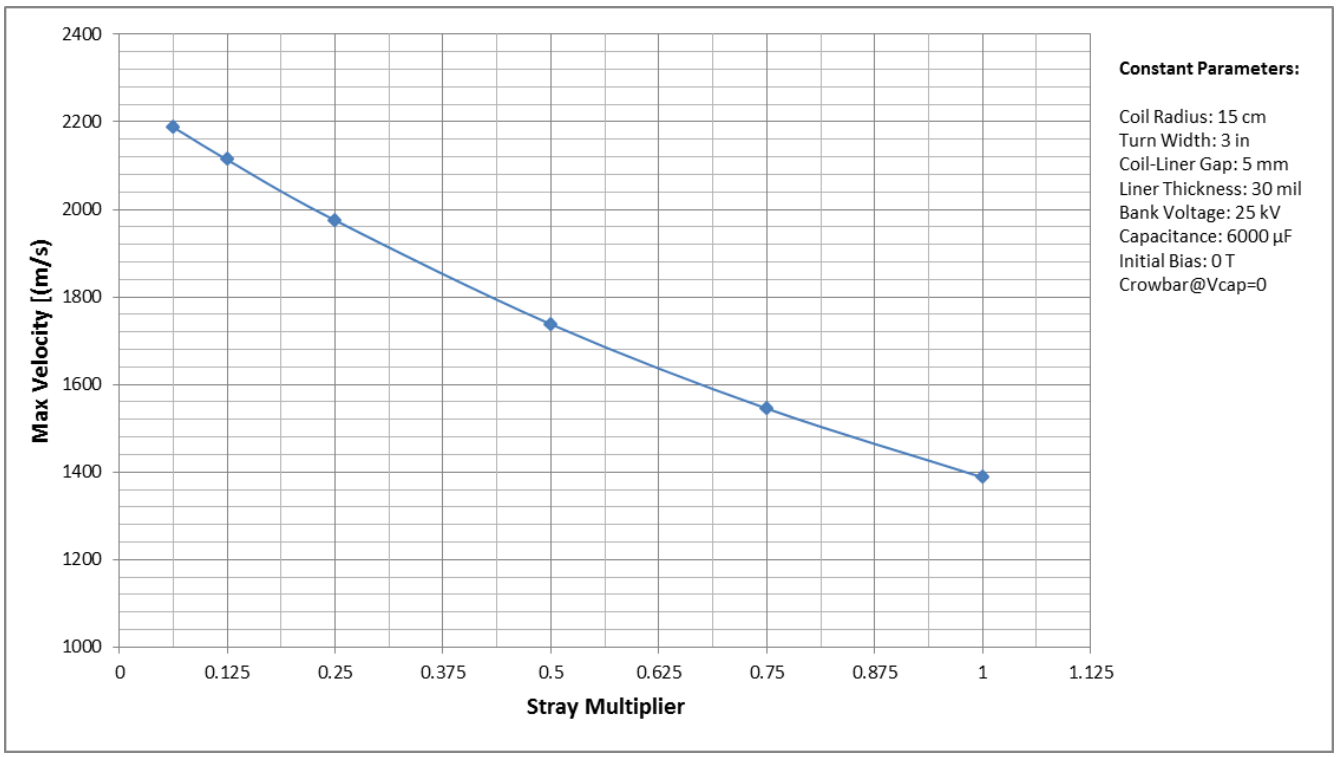

Figure 4b. Plot of Maximum Liner Velocity

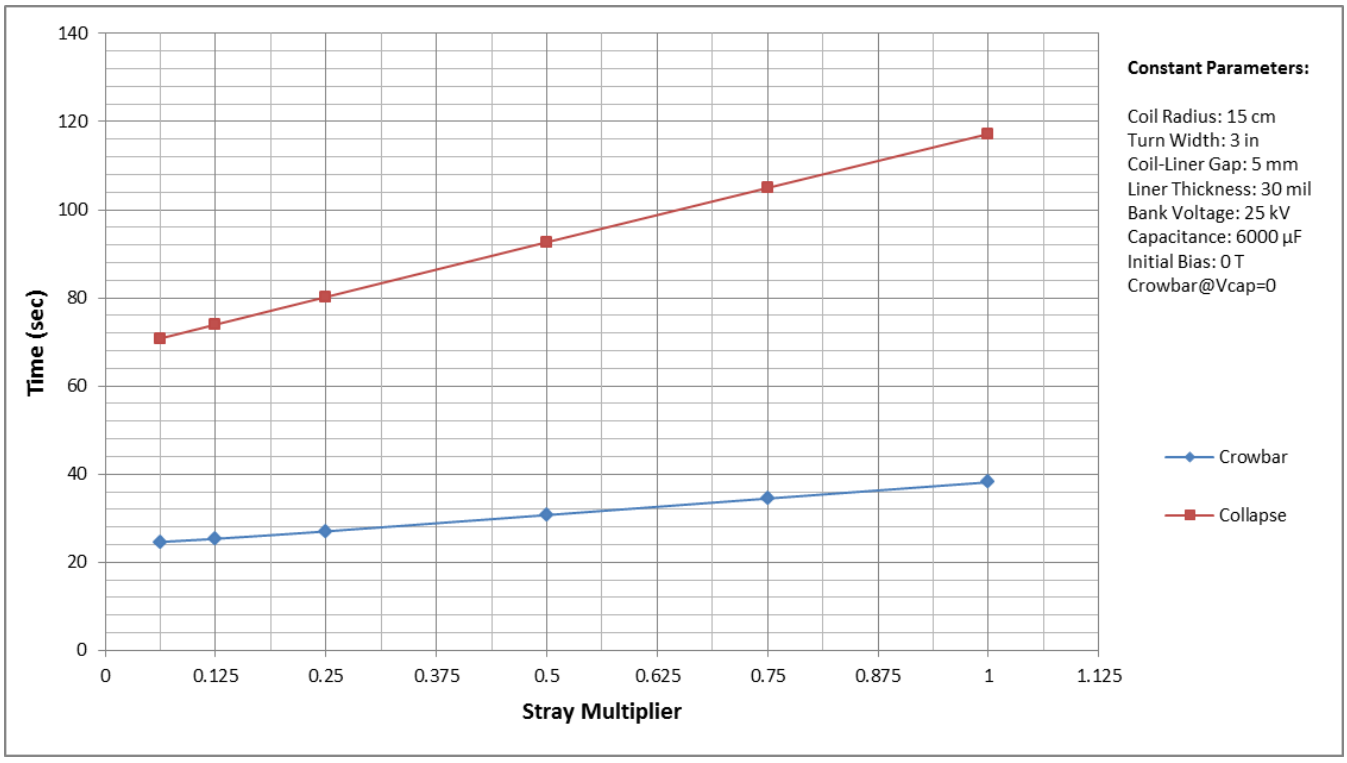

Figure 4c. Plot of Circuit Crowbar and Liner Collapse time

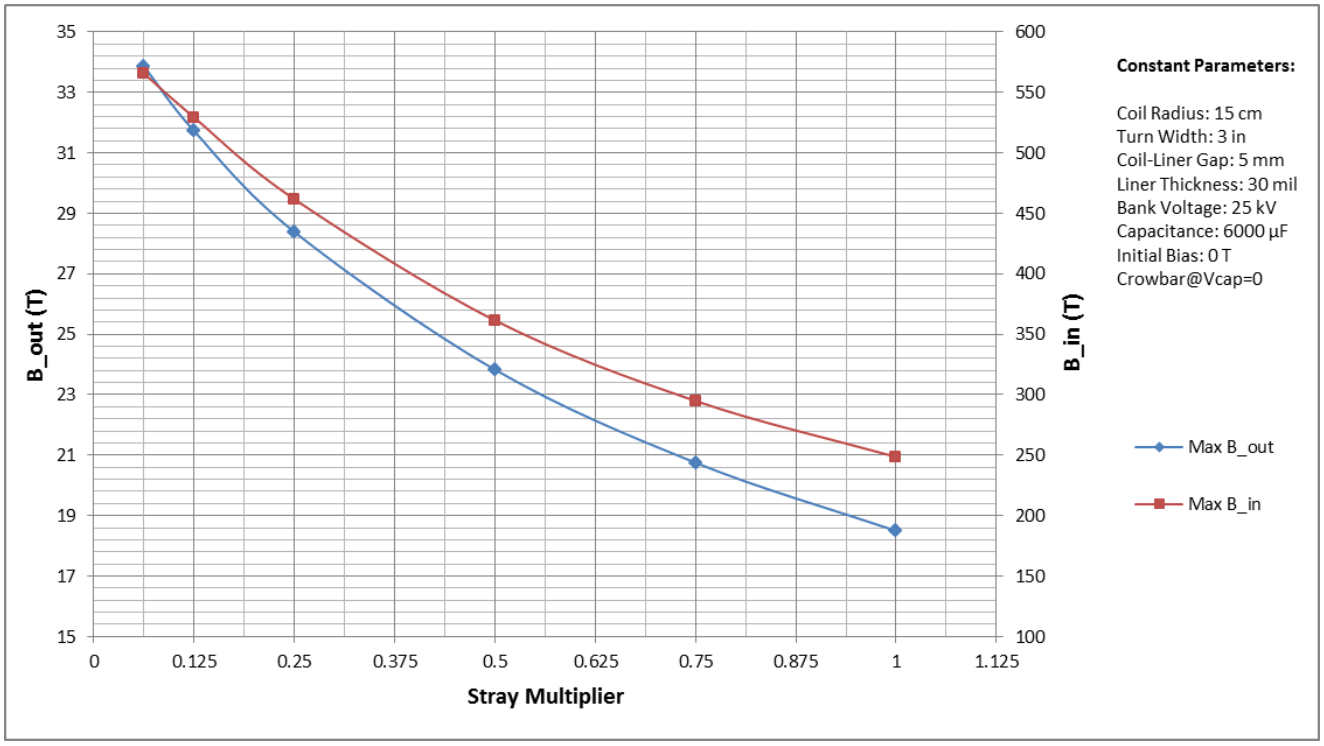

Figure 4d. Magnetic field strength at inner and outer liner surface

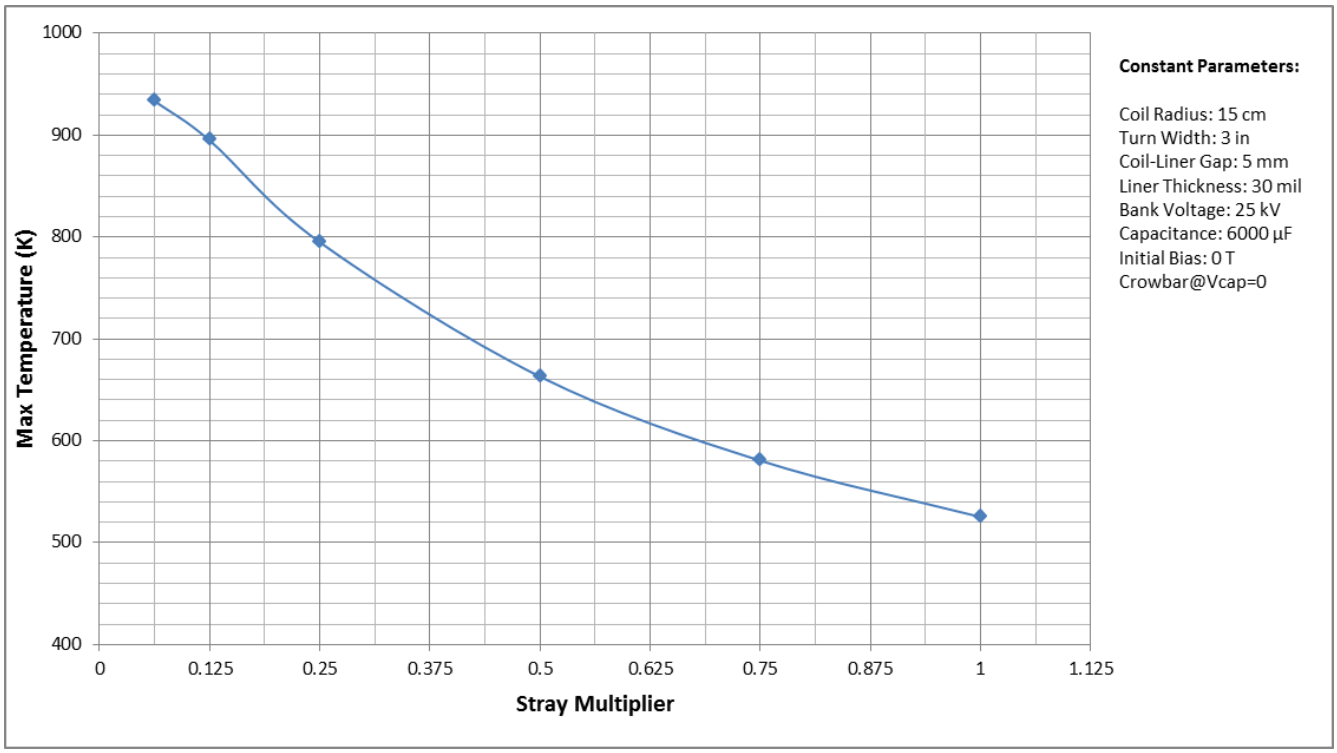

Figure 4e. Plot of the maximum temperature of the liner

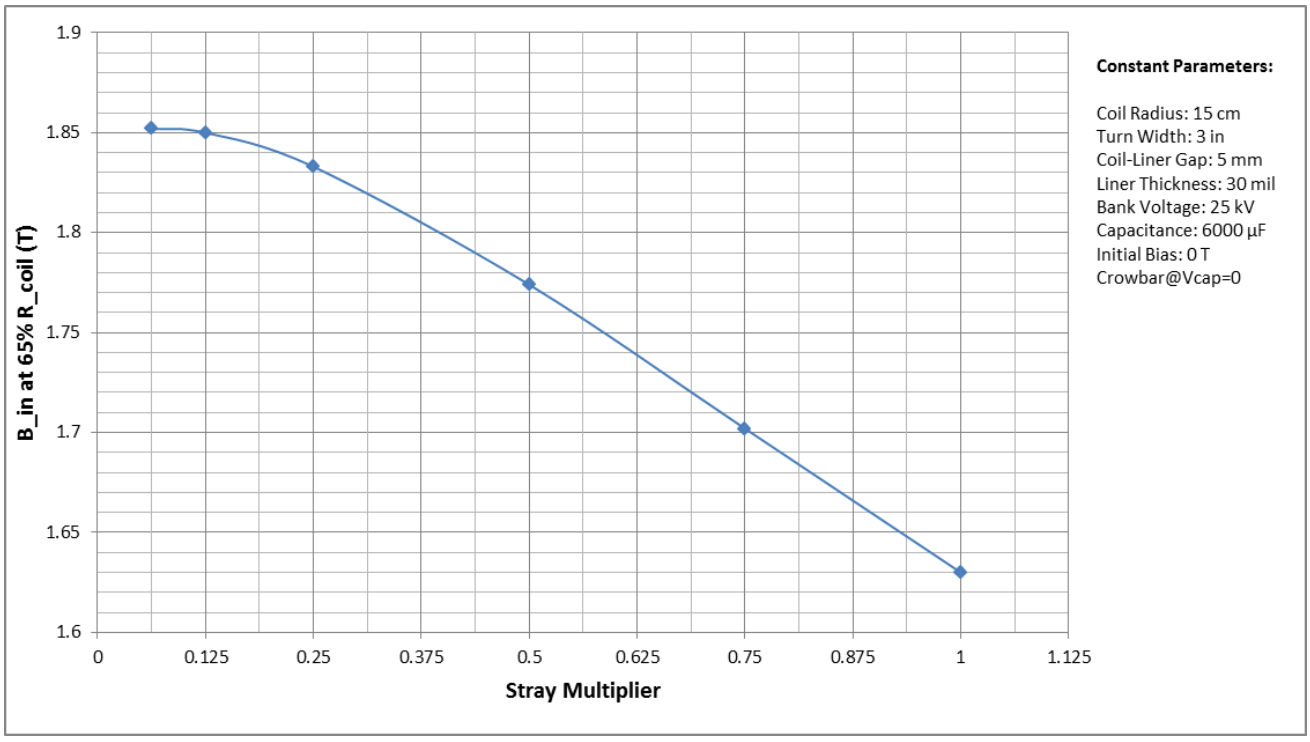

Figure 4f. Plot of the magnetic field strength of liner inner surface at 65% coil radius

Bank Voltage Variation:

The result of the parametric study of the half-turn coil with Bank Voltage variation is shown below in Fig. 5a-5f. A smooth spline fit is used between data points. For Bank Voltage variation, Liner Thickness is fixed at 30 mil, the Stray Multiplier is fixed at 0.25, the Bank Capacitance is fixed at 6000 μF, and the Initial Bias Field is fixed at 0 T.

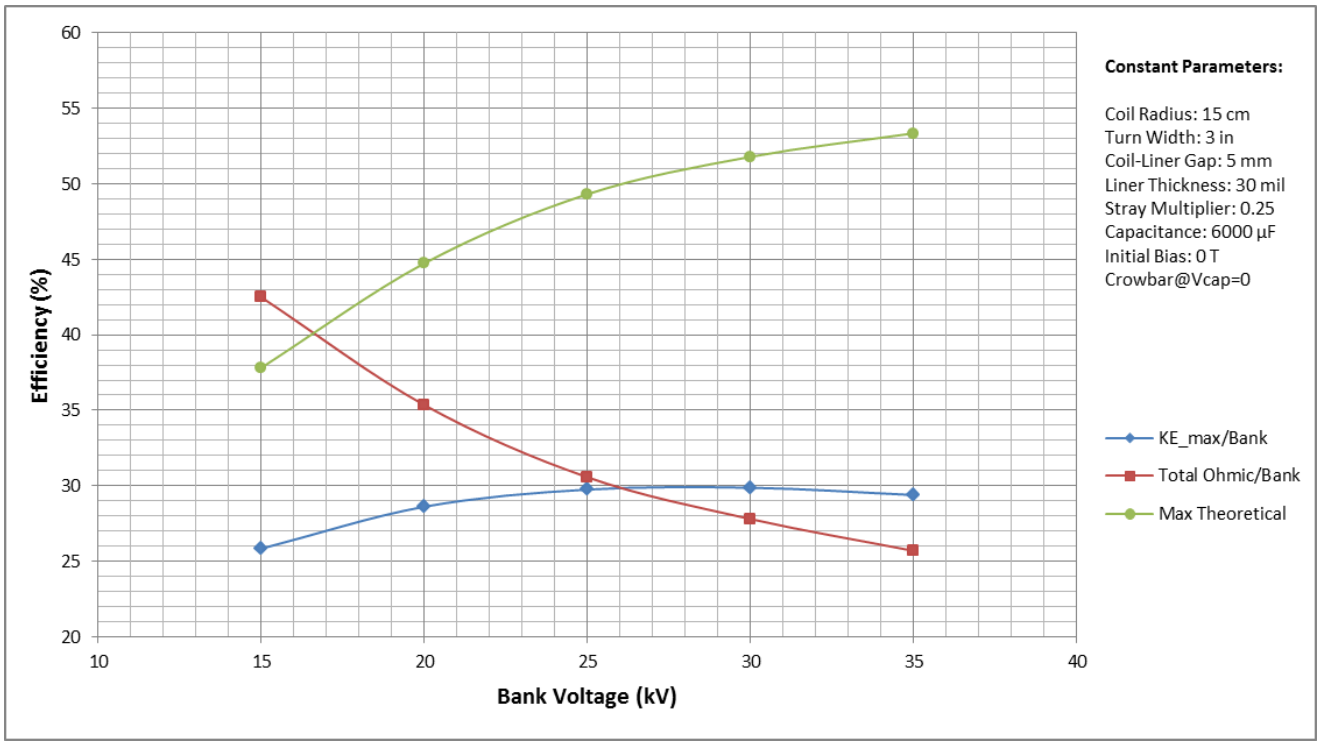

Figure 5a. Plot of Kinetic Energy, Ohmic Loss, and Max Theoretical Efficiencies

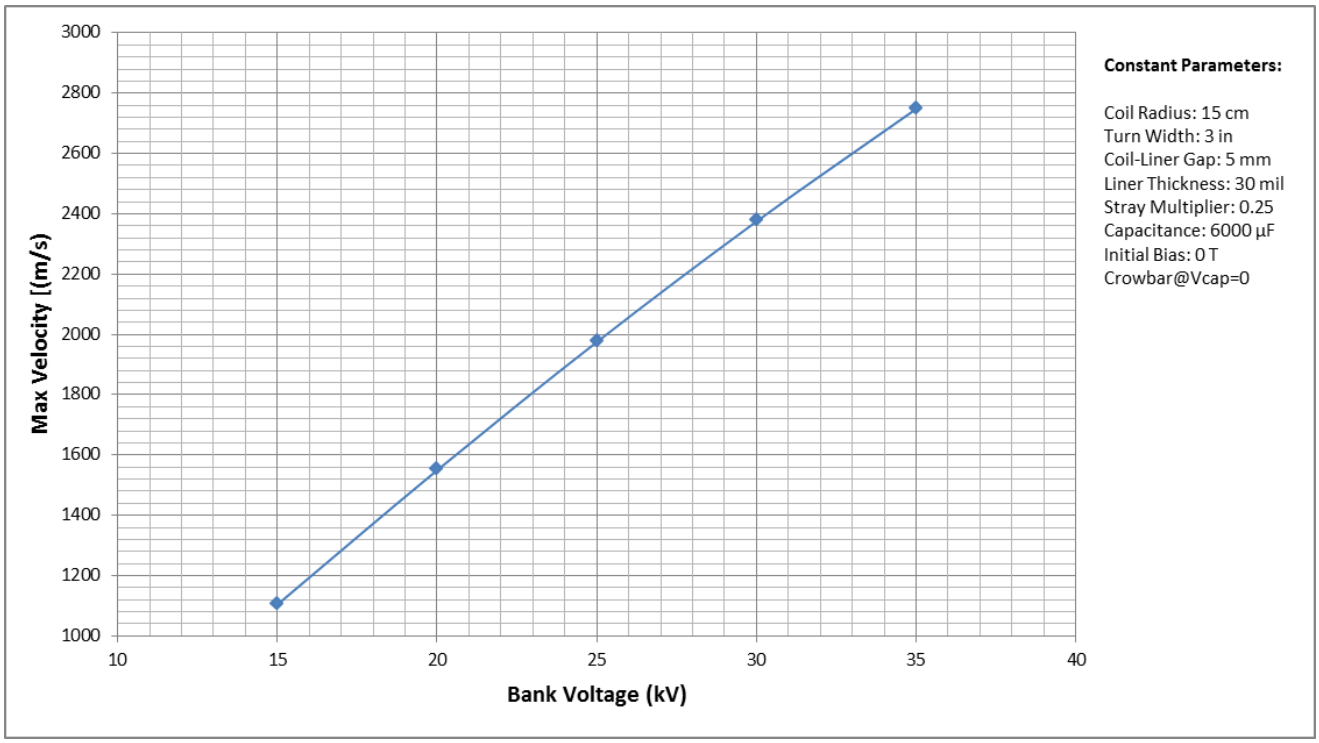

Figure 5b. Plot of Maximum Liner Velocity

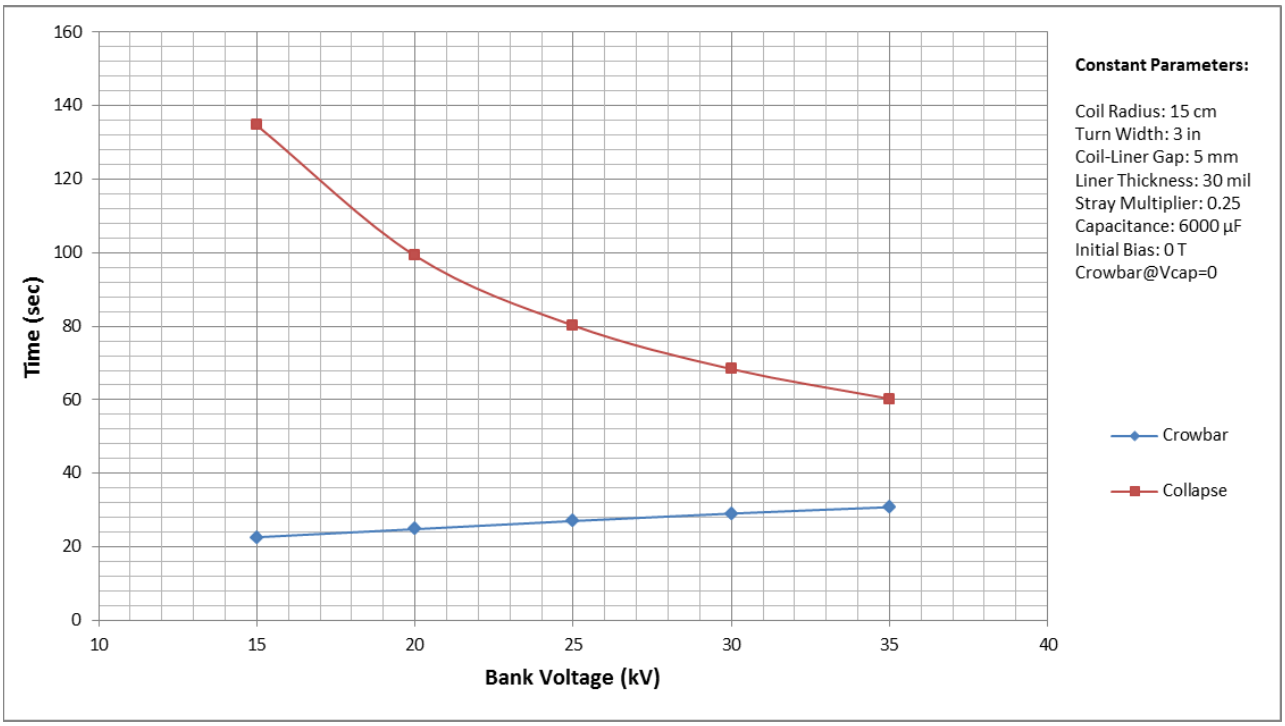

Figure 5c. Plot of Circuit Crowbar and Liner Collapse time

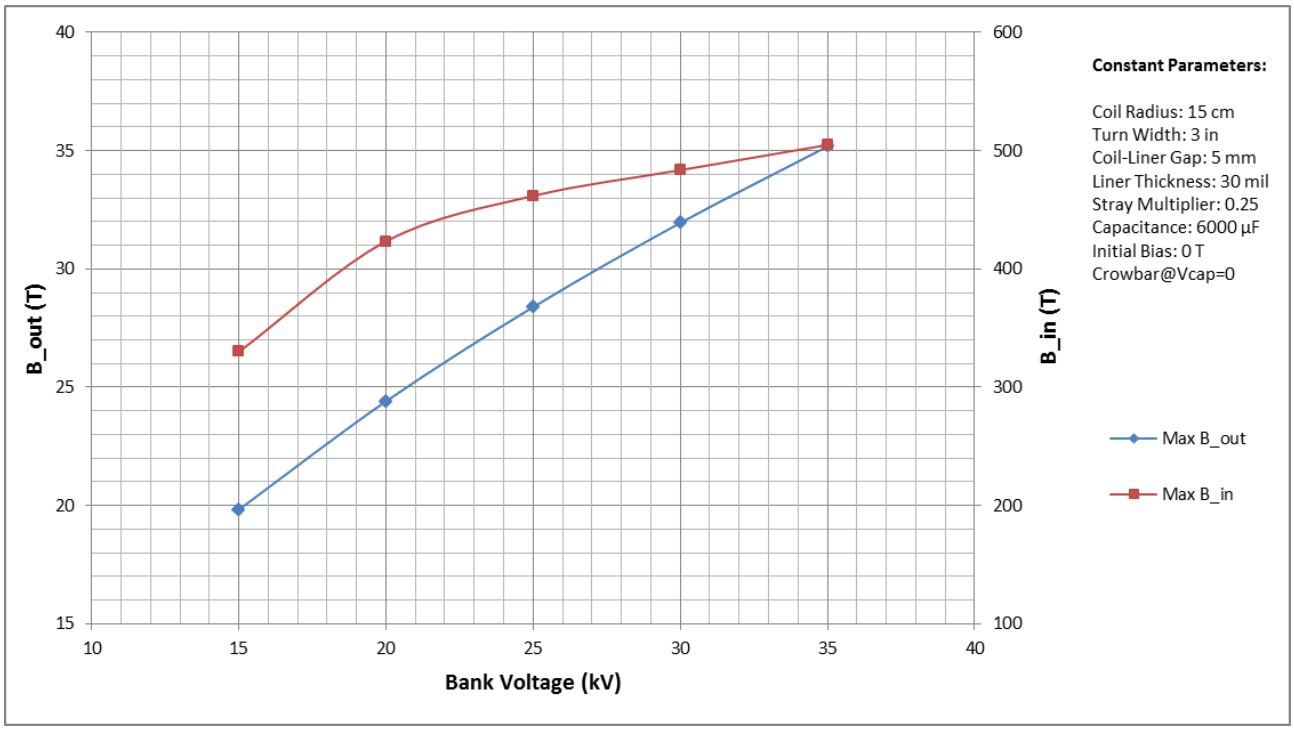

Figure 5d. Magnetic field strength at inner and outer liner surface

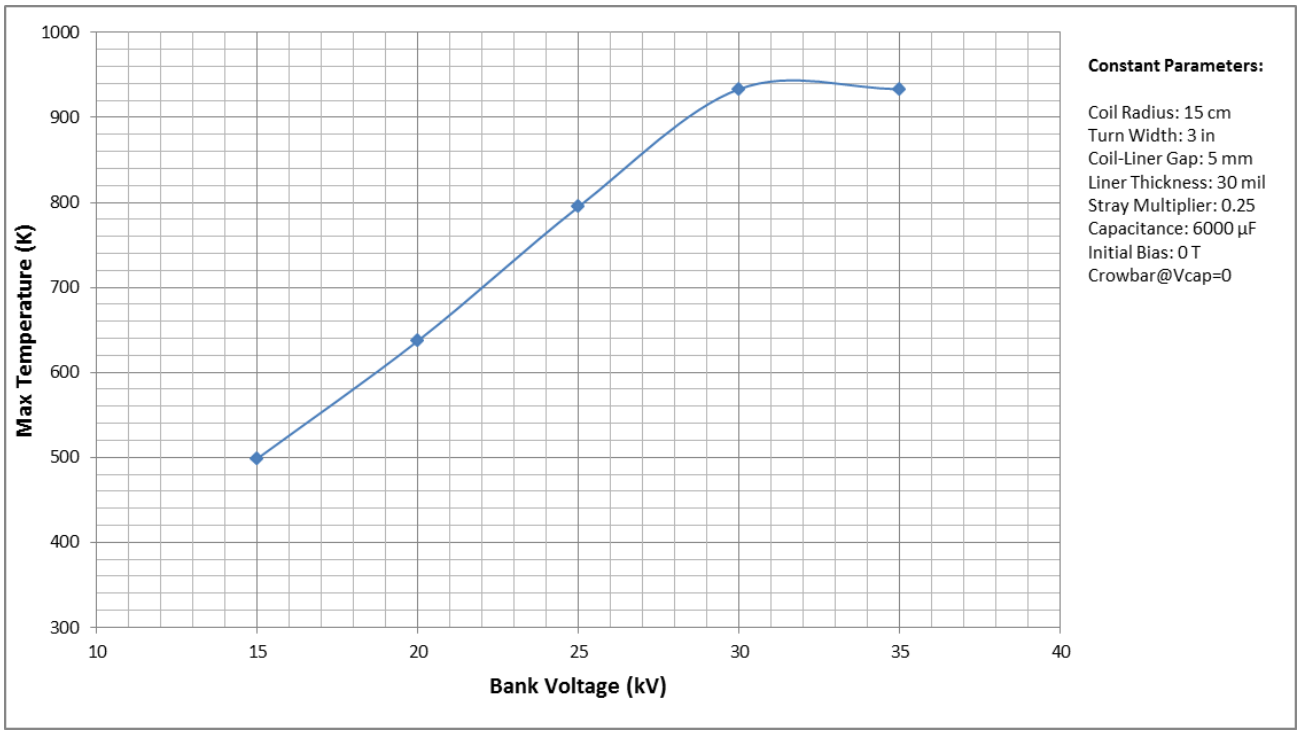

Figure 5e. Plot of the maximum temperature of the liner

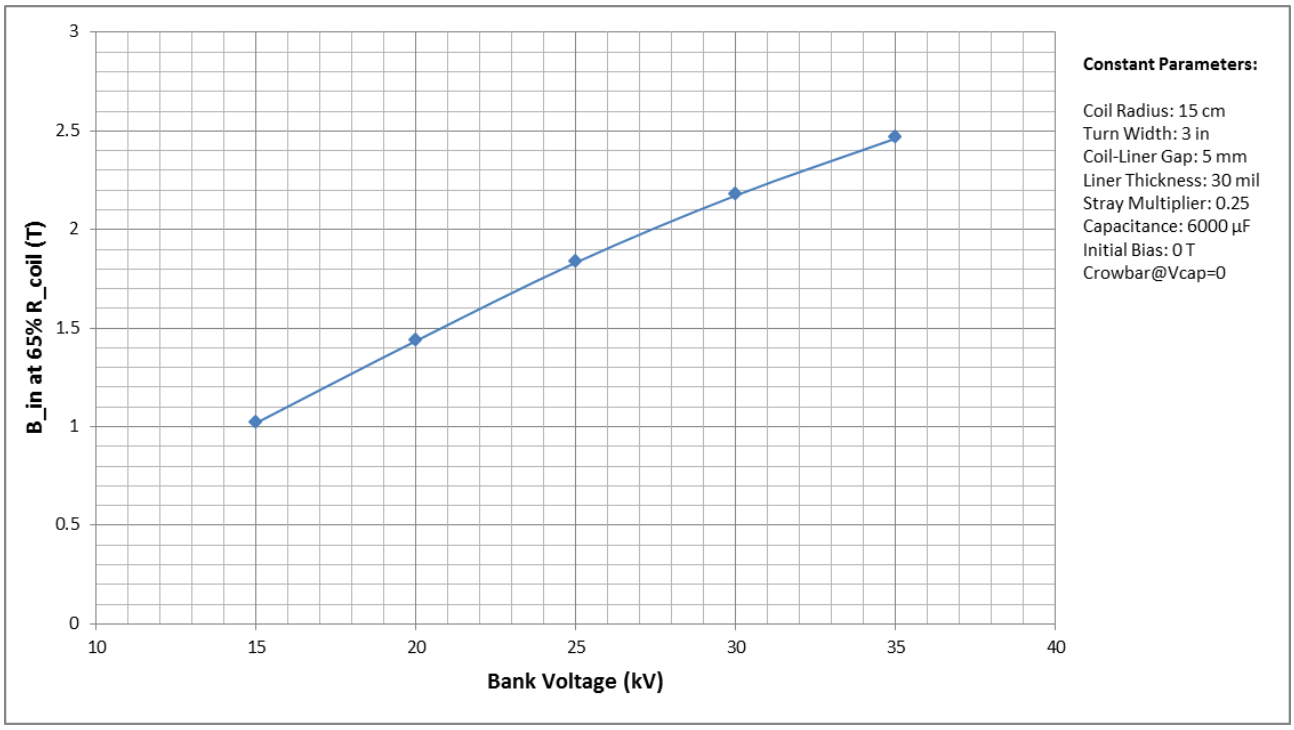

Figure 5f. Plot of the magnetic field strength of liner inner surface at 65% coil radius

Bank Capacitance Variation:

The result of the parametric study of the half-turn coil with Bank Capacitance variation is shown below in Fig. 6a-6f. A smooth spline fit is used between data points. For Bank Capacitance variation, Liner Thickness is fixed at 30 mil, the Stray Multiplier is fixed at 0.25, the Bank Voltage is fixed at 25 kV, and the Initial Bias Field is fixed at 0 T.

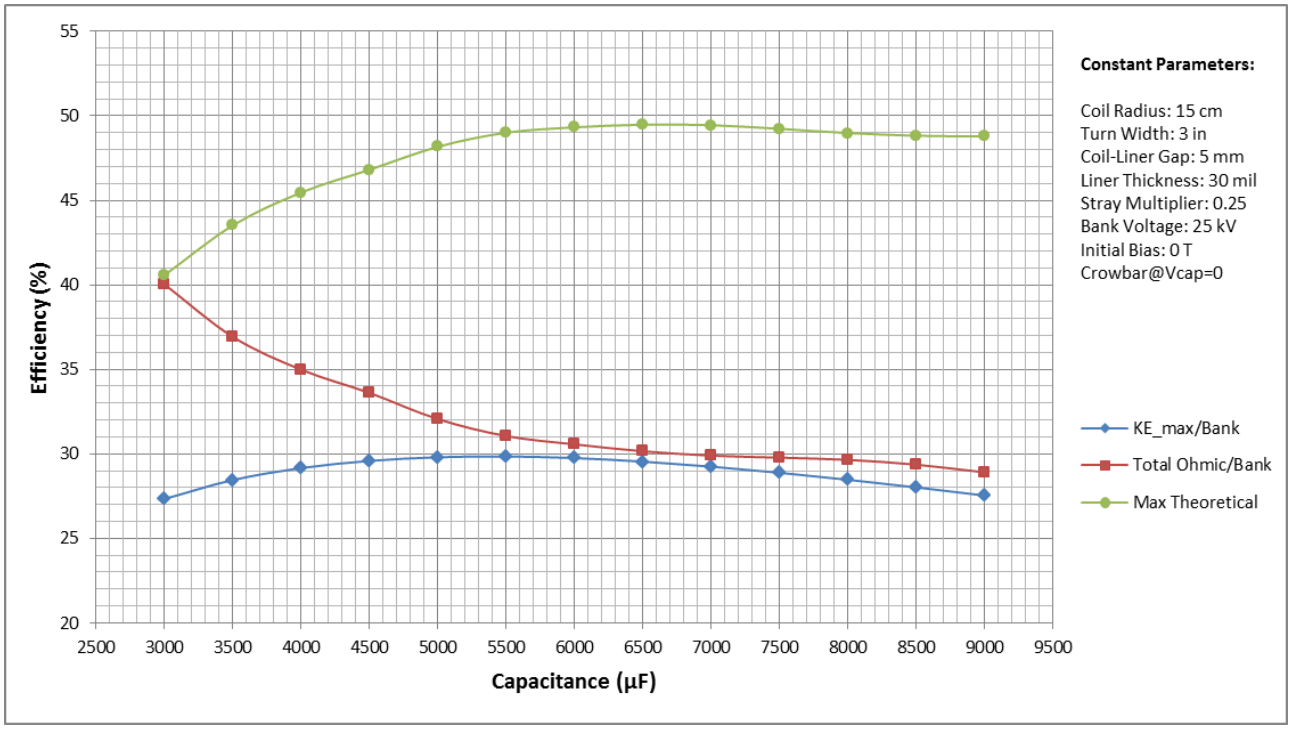

Figure 6a. Plot of Kinetic Energy, Ohmic Loss, and Max Theoretical Efficiencies

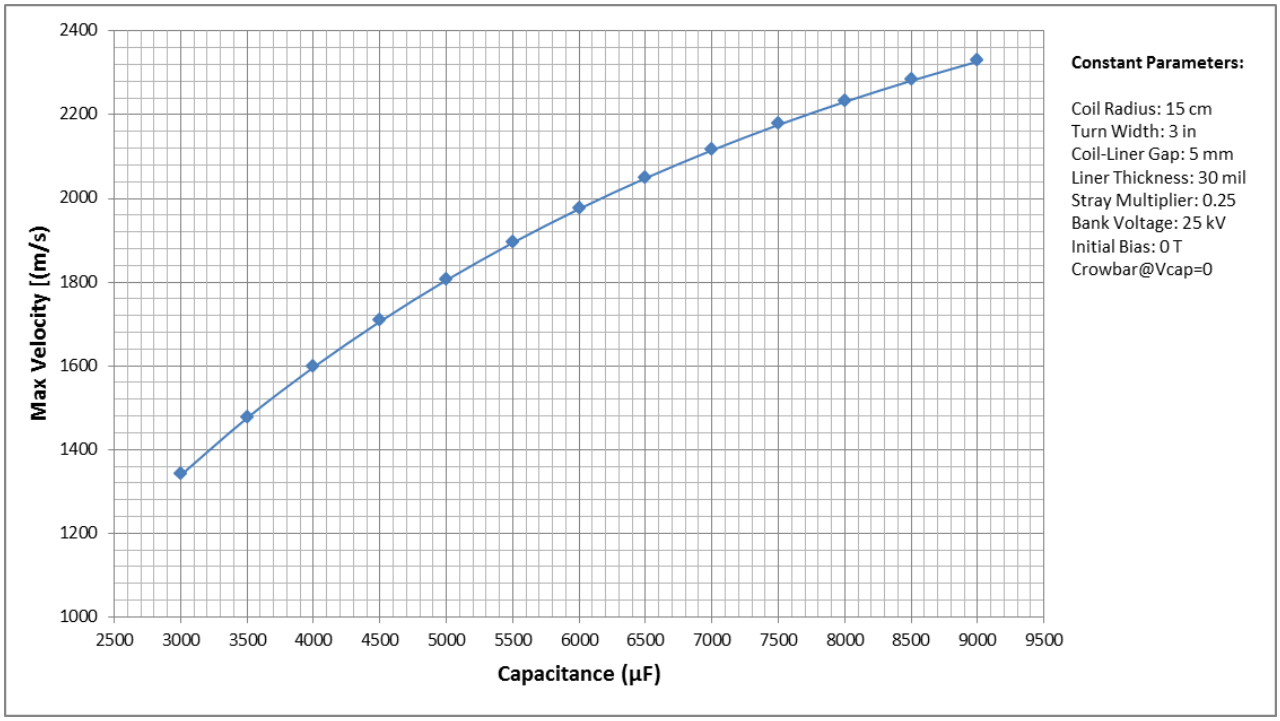

Figure 6b. Plot of Maximum Liner Velocity

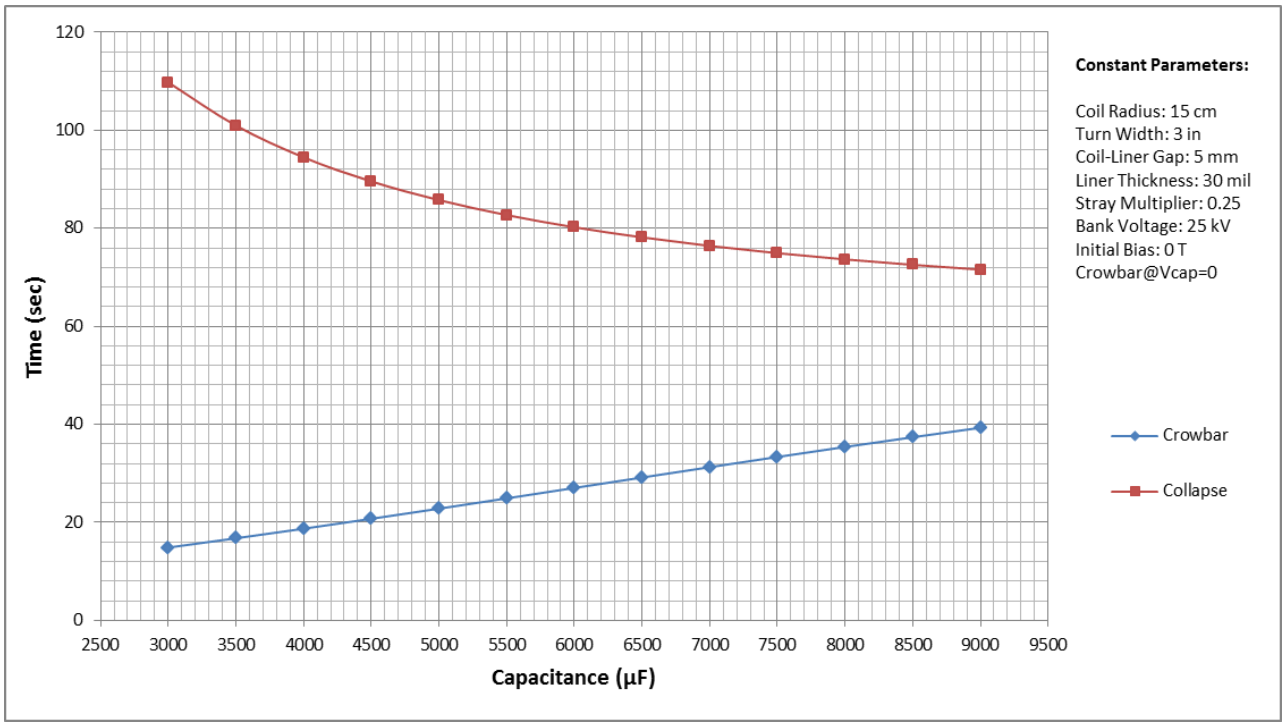

Figure 6c. Plot of Circuit Crowbar and Liner Collapse time

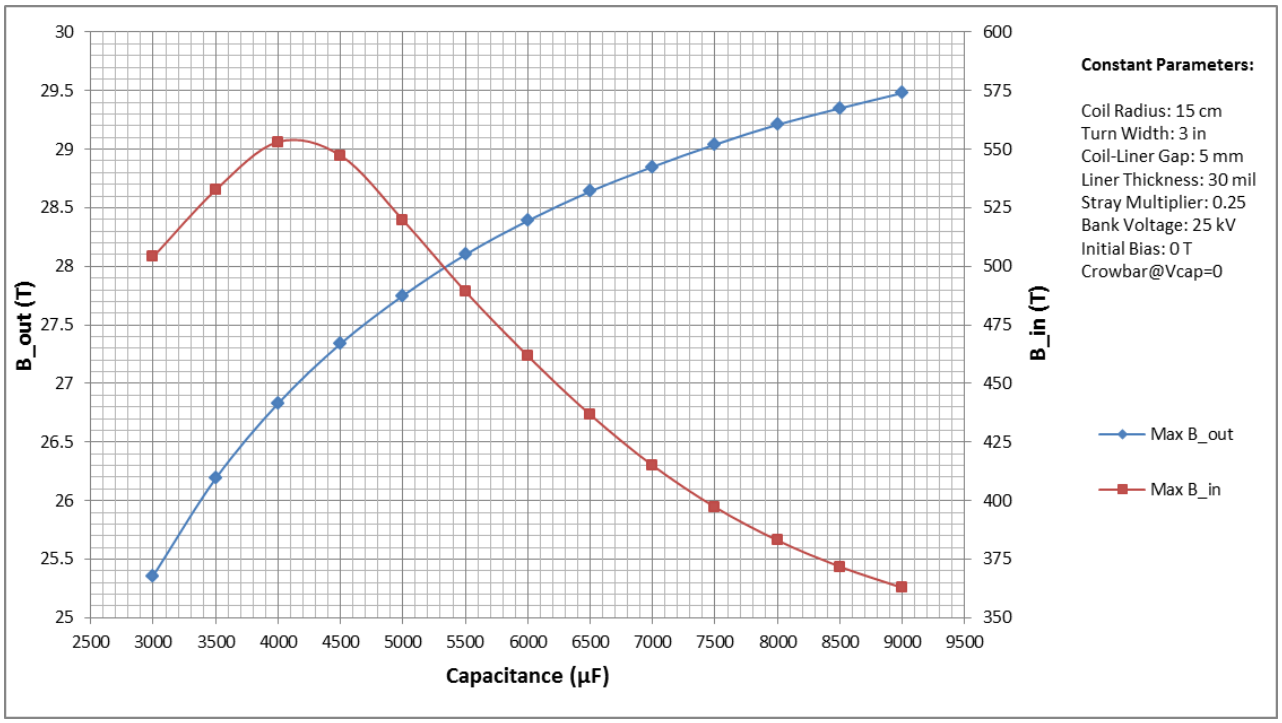

Figurer 6d. Magnetic field strength at inner and outer liner surface

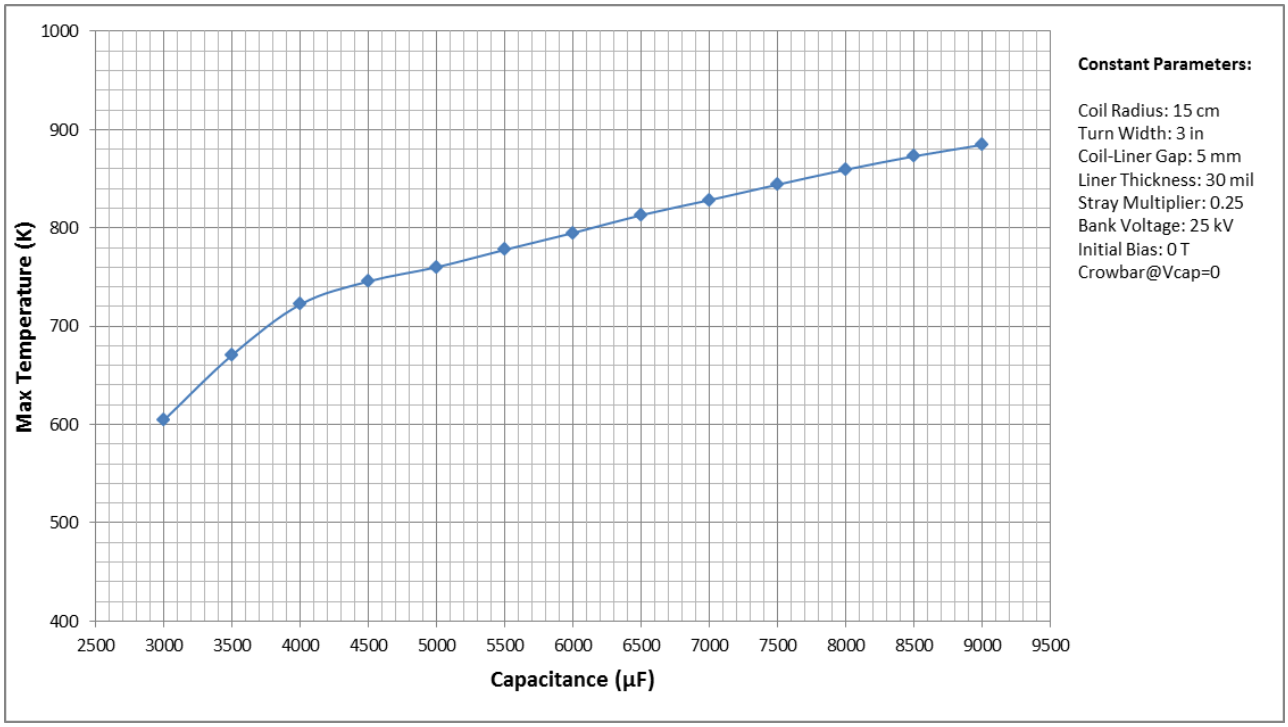

Figure 6e. Plot of the maximum temperature of the liner

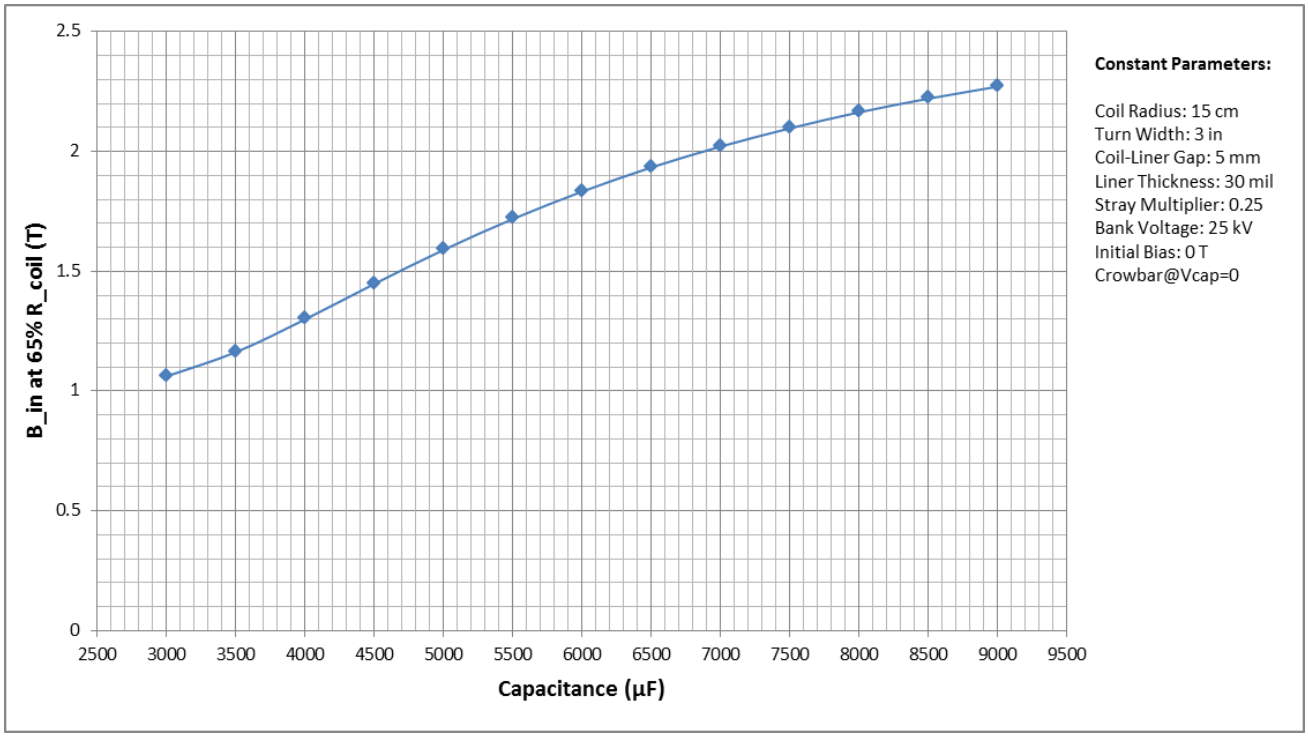

Figure 6f. Plot of the magnetic field strength of liner inner surface at 65% coil radius

Initial Bias Field Strength Variation:

The result of the parametric study of the half-turn coil with Initial Bias Field Strength variation is shown below in Fig. 7a-7f. A smooth spline fit is used between data points. For Bias Field variation, Liner Thickness is fixed at 30 mil, the Stray Multiplier is fixed at 0.25, the Bank Voltage is fixed at 25 kV, and the Bank Capacitance is fixed at 6000 µF.

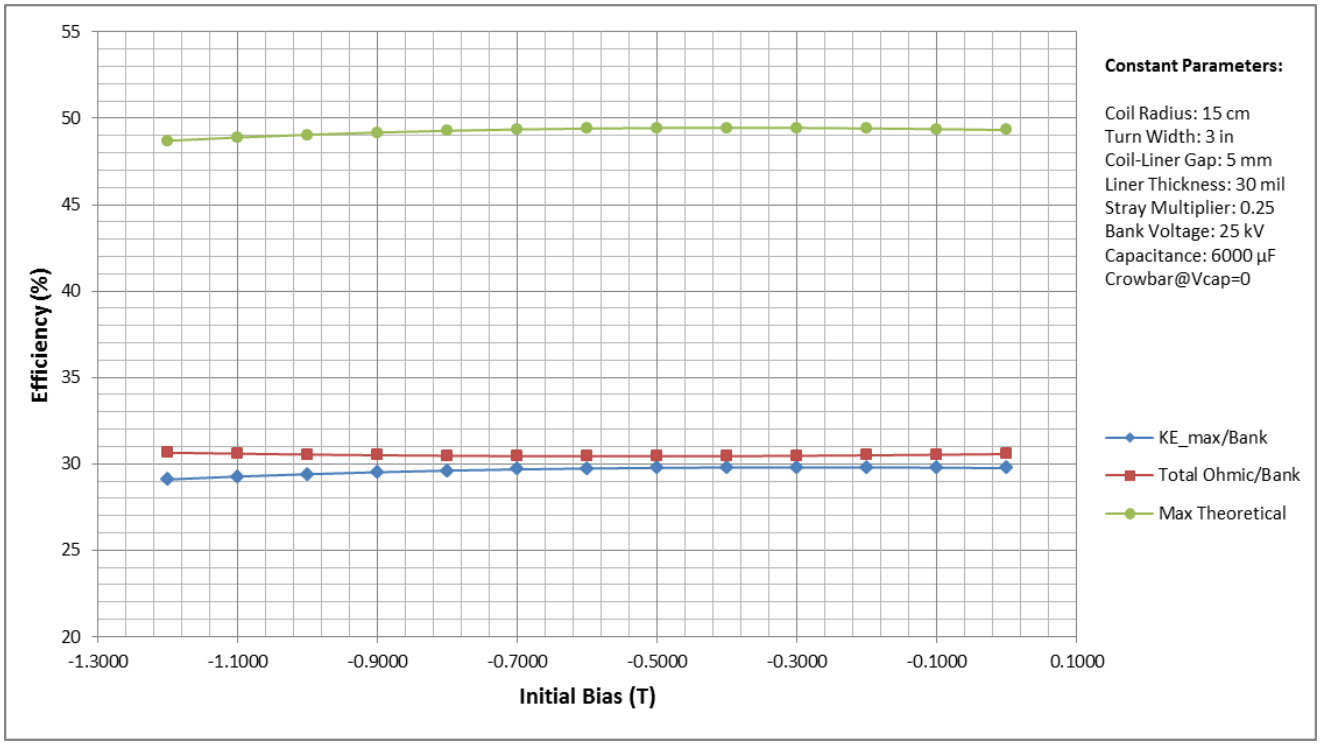

Figure 7a. Plot of Kinetic Energy, Ohmic Loss, and Max Theoretical Efficiencies

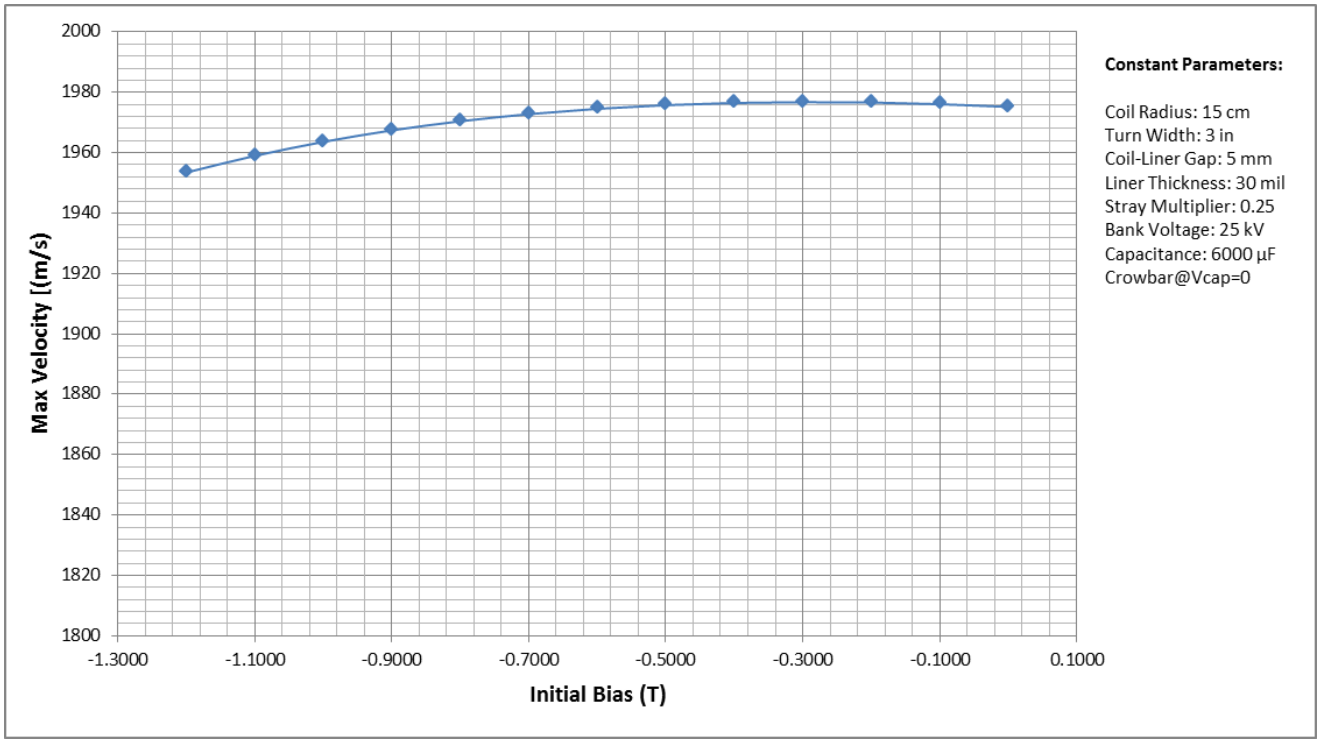

Figure 7b. Plot of Maximum Liner Velocity

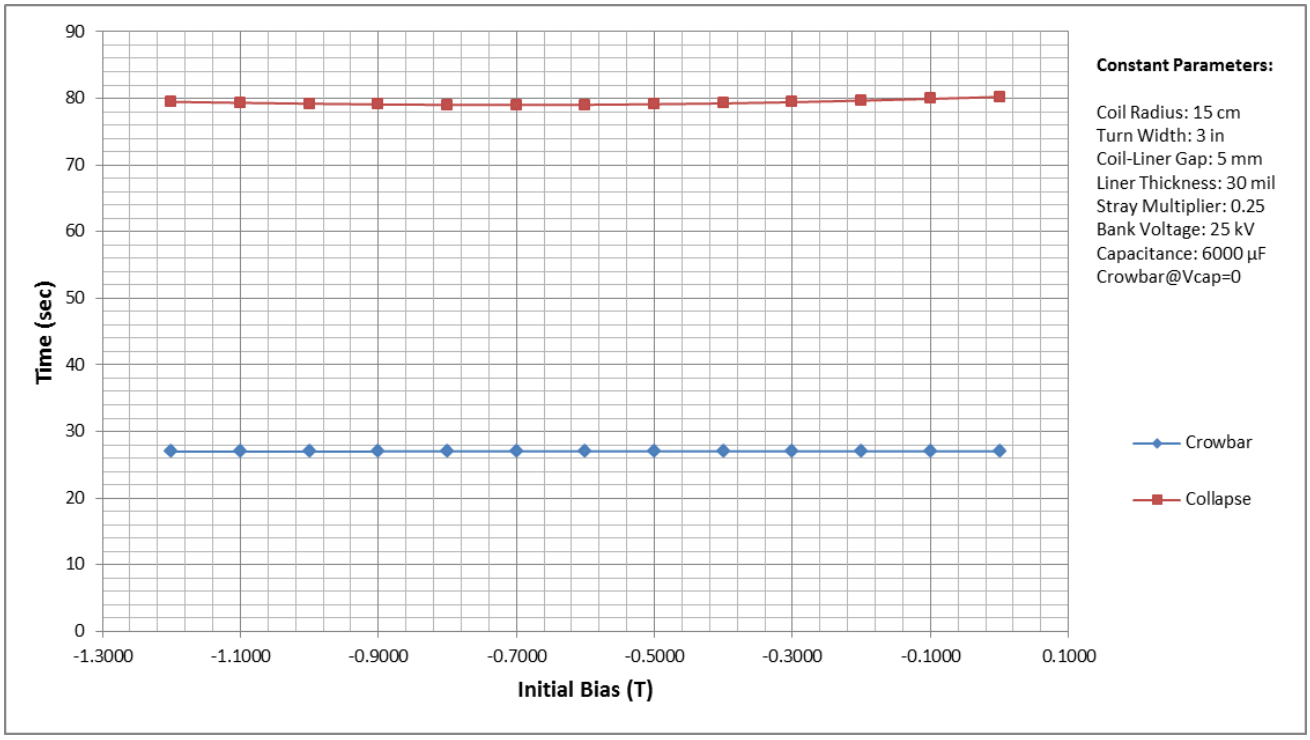

Figure 7c. Plot of Circuit Crowbar and Liner Collapse time

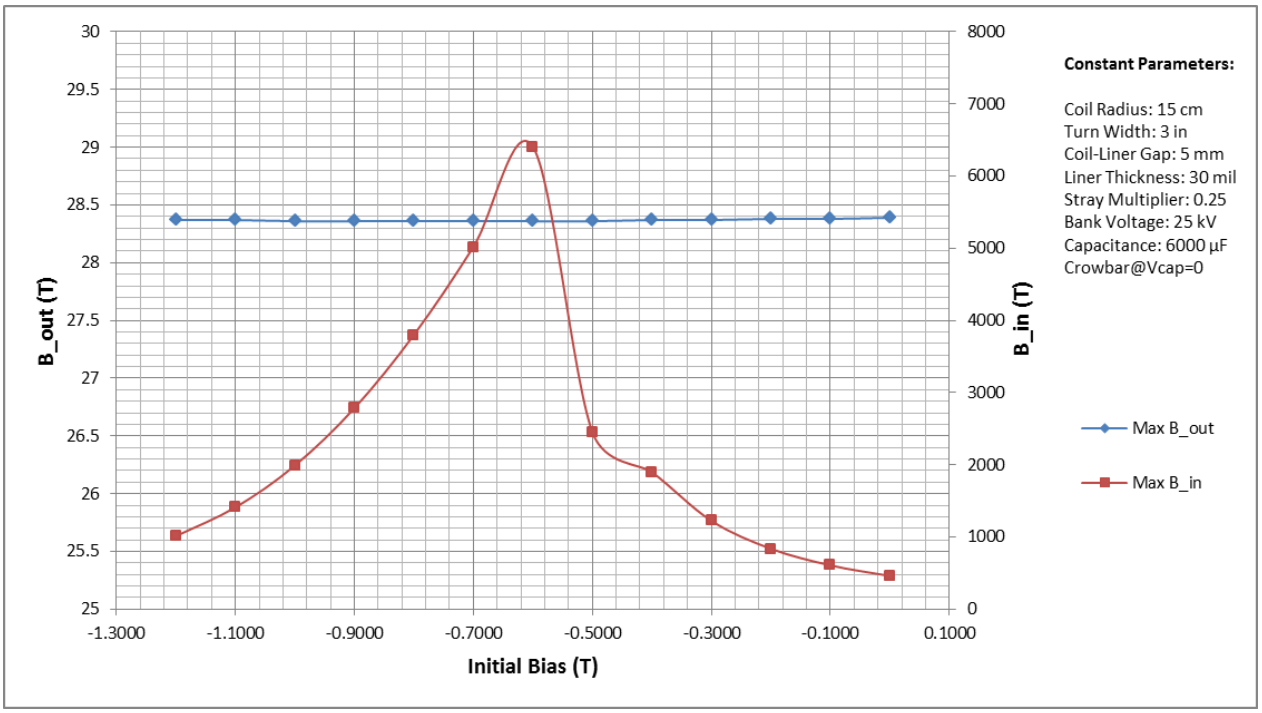

Figure 7d. Magnetic field strength at inner and outer liner surface

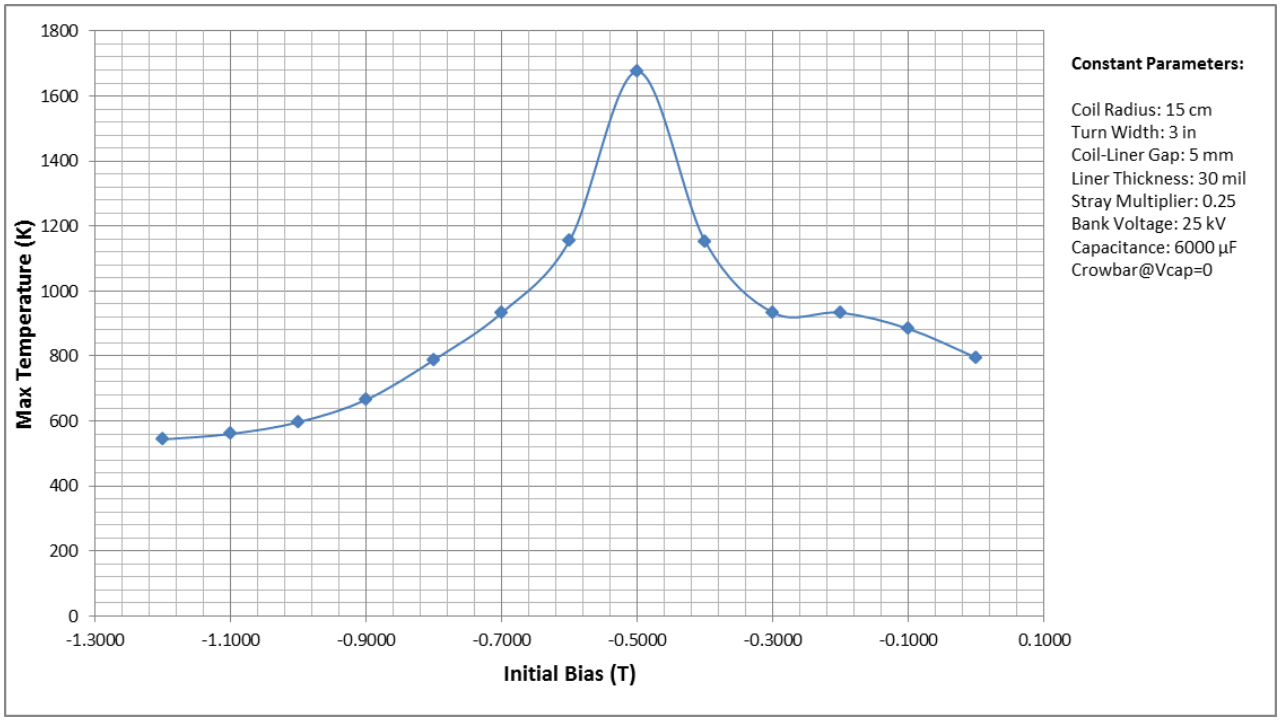

Figure 7e. Plot of the maximum temperature of the liner

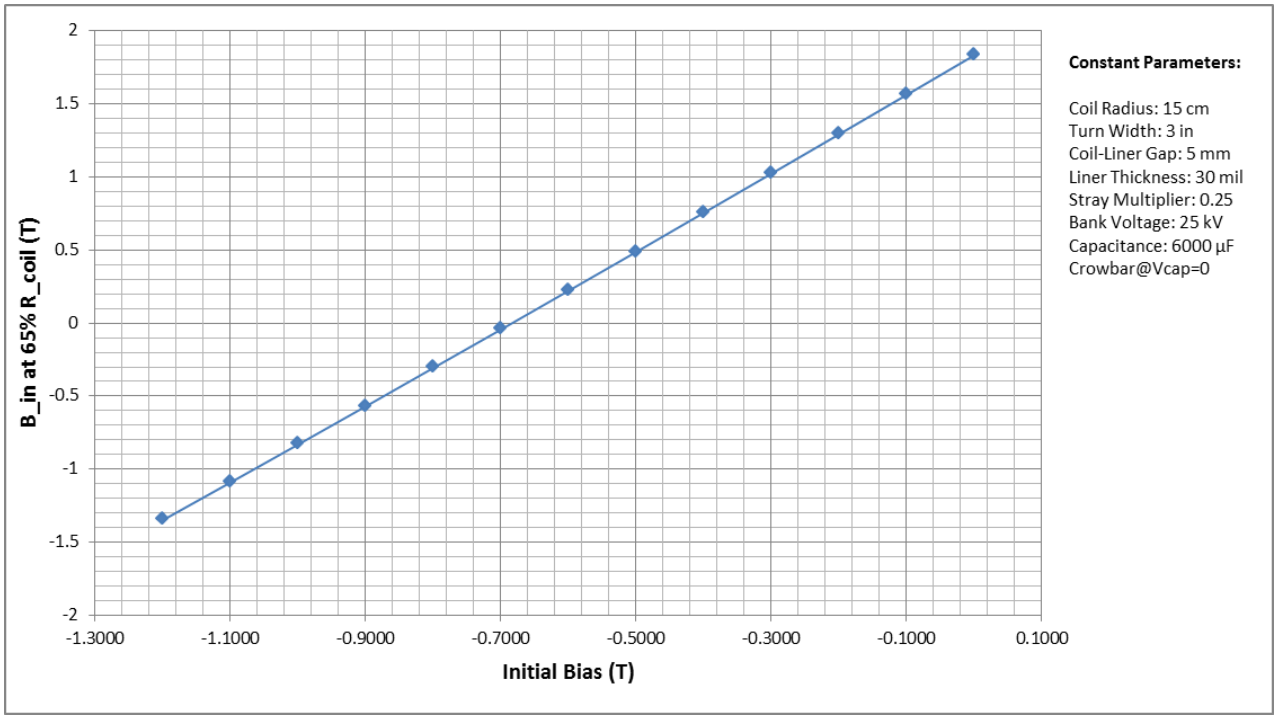

Figure 7f. Plot of the magnetic field strength of liner inner surface at 65% coil radius

Conclusion:

From the analysis, it was seen that near the default FDR experimental configuration, 20 mil to 30 mil thick liner offers the optimal performance in terms of Kinetic Energy Efficiency and Liner Speed requirement. Making the liner any thicker near the default bank energy levels seems to degrade the performance of the Bank energy to kinetic energy conversion, as well as increasing the total Ohmic loss in the circuit due to required longer collapse time. While improving the capacitor bank and increasing the bank voltage showed improvement in the maximum theoretical efficiency of the coil-liner compression, since there exists no energy re-capture mechanism in the experiment, this improvement does not matter for the experimental performance of the coil. For Bank energy to Kinetic Energy conversion, 25 kV to 30 kV showed the best return on investment, while satisfying the requirement in the liner speed. Increasing the bank capacitance did not show much improvement in terms of efficiency, as any capacitance above 5500 μF to 6000 μF showed no improvement. While liner velocity could be improved with increase in capacitance, 6000 μF case already meets the velocity requirement. Initial bias variation also showed little variation in efficiency and liner speed. This suggests that the initial bias can be modified liberally to match the field requirement for FRC injection without much penalty in performance.

One parameter which showed greatest influence in the liner compression performance was stray inductance, and lowering the stray inductance value could significantly improve the performance of the experiment. Cutting the stray inductance in half is desirable from performance standpoint, and if energy re-capture mechanism can be implemented, energy conversion efficiency of roughly 60% can be achieved for Bank energy to kinetic energy conversion.

1D Liner Code Routine

Introduction:

1D Liner Code is a Matlab® code developed to simulate the dynamic liner-compression for the fusion driven rocket experiment. The code assumes symmetric two turn coil with axial dependence averaged out. A radial dependence of the magnetic field strength is captured in the simulation with two geometric parameters derived externally to the code. This section covers the basic theory behind the 1D liner code used for the parametric study as well as a routine set the code uses to compute liner compression. It also covers what inputs are used in the code and brief explanation of how they are incorporated in the code routine.

1D Liner Code External Input:

The 1D Liner uses external data for the lookup table it uses to compute various parameters. Five externally derived data is required: Coil-Liner system inductance and Liner inductance as function of liner outer radius, Field-Flux parameter for both inner and outer region as function of liner inner radius, and material resistivity data as a function of temperature.

Material resistivity data is derived from the data found in literature, and is used only for the liner thermal and resistance calculation. The coil resistance variation due to temperature change is neglected in the code and is assumed to be constant. If no data exists in literature for a specific alloy of metal that is used for the coil-liner system, then the resistivity data is extrapolated based on the pure elemental value based on best engineering judgment. The code assumes resistivity data to be in unit of Ohm-m and temperature to be in unit of K.

Coil-Liner system inductance and liner inductance is determined by running ANSYS Maxwell 3D analysis in the AC steady state configuration at frequency of 20 kHz. Frequency of 20 kHz is chosen due to the fact that the averaged quarter cycle time and the crowbar decay time suggests frequency in the neighborhood of 5 kHz to 40 kHz. In Maxwell 3D, the variation of inductance with frequency from 5 kHz to 40 kHz was shown to be only 1%, which is negligible, considering that the 1D approximation introduces far greater error. For liner inductance, because two liners are assumed to exist in the Coil-Liner system, self-inductance and the mutual inductance of the

coil is computed in Maxwell at various liner outer radius. The effective net liner inductance (L_{net}) is calculated from the equation:

$$L_{net} = \frac{L^2 - M^2}{2L - 2M}$$

where L is the self-inductance of one liner, and M is mutual inductance between the two liners. For both Coil-Liner system inductance and liner inductance data, the code assumes that the inductance is in unit of nH and liner outer radius to be in unit of hundredth percent of coil inner radius.

Field-Flux parameters for both outer and inner region (C_A and C_B respectively) are defined to be

$$B_{out} = C_A \Phi_{out}$$

$$B_{in} = C_B \Phi_{in}$$

where Φ_{out} is flux in the outer region, Φ_{in} is flux in the inner region, B_{out} is the root mean square averaged magnetic field at the outer surface of the liner, and B_{in} is the root mean square averaged magnetic field at the inner surface of the liner. Moqui vacuum field solver is used to compute the Field-Flux parameters at various liner inner radiuses under assumption that the liners are a perfect flux conserver. Due to the fact that Field-Flux parameter for the inner region diverges off to infinity as the liner approaches radius of zero, the liner is assumed to be an infinitely long solenoid once the liner inner radius reaches 1% of the inner coil radius. This is implemented to mitigate the issues interpolating the external data at small radius without introducing large error. For both Field-Flux parameter data, the code assumes the Field-Flux parameter to be in unit of T/Wb and liner inner radius to be in unit of hundredth percent of coil inner radius.

Calculation Routine:

The 1D liner code is separated into three main computational blocks: preprocess, loop solver, and postprocess. In the preprocess block, the user input data is processed and checked to feed it into the loop solver. The data prepared in preprocess is fed into the loop solver block, and the

loop solver continues to solve inside the loop until the end condition is met. Once the end condition is met, the code breaks from the loop solver and postprocesses the data collected in the loop solver and outputs the result. In the 1D Liner Code, first order Euler formulation is used throughout the calculation. While first order Euler method is no computationally efficient, by using small enough time step and Lagrangian time stepping control, the accuracy of the solution is maintained. In following sections, each code steps as well as associated sub-steps are discussed further.

Preprocess Block:

In the preprocess block, the code reads the input data and prepares it to feed it into the loop solver. From the user defined inputs, the code computes initial liner mass and geometry. It then automatically fits and interpolates the data from external input files using built-in automatic smoothing spline fit function in Matlab® (spaps). After fit functions are produced for each of the external input files, the first step values are computed and the loop solver is started.

Loop Solver Block:

The Loop Solver Block consist the bulk of the 1D liner code's computational routine. In the loop solver, following steps are computed in the following order. First, a global circuit system is solved to determine the current flow into the Coil-Liner system at the given time step. Second, the Coil-Liner system is assumed to be independent from the global circuit system and the dynamics of the liner compression is computed and the new lumped global parameter for the Coil-Liner system is computed to feed into the global circuit calculation of the next iteration. Third, Lagrangian time step and magnetic field reversal check is conducted and current time step is repeated as necessary. Fourth, end condition for the calculation loop is checked, and the loop is repeated until the end condition is met. If the end condition is met, the code breaks the loop to send the analyzed data to postprocess block.

Global Circuit Calculation:

In this step, the Coil-Liner system is treated as a black block in the circuit which has known resistance, inductance, and temporal change in inductance (dL/dt). With the circuit property of the other components in the circuit known, the Kirchhoff's circuit laws are applied to the circuit to compute the current flowing in each sections and capacitor voltage. Three circuit types are

supported in the 1D liner code: ringing, crowbar, and timed crowbar. In the ringing case, the circuit is assumed to be simple LRC circuit. In the crowbar case, the circuit is assumed to be same as ringing case, until the capacitor voltage drops below zero. At this point, crowbar switch is assumed to instantaneously close, allowing the current to flow through the crowbar circuit. In the timed crowbar case, same circuit equation is used as the crowbar case, but it uses user defined crowbar time to close the crowbar switch. The circuit convention used in the code is shown below in figure A1.

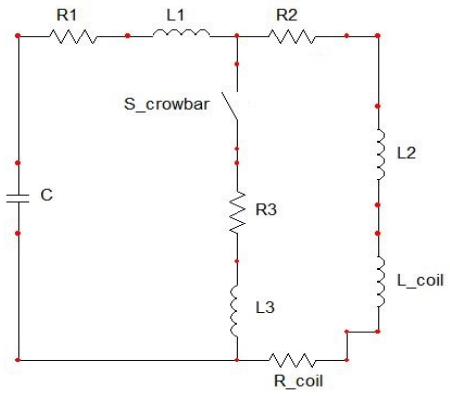

Figure A1. Circuit Schematic for 1D Liner Code

There are three circuit sections in the default circuit configuration used in the 1D liner code. Section 1 is defined to be the section containing Capacitor with capacitance C, Resistor with resistance R_1, and inductor with inductance L_1; Section 2 is defined to be the section containing resistor with resistance R_2, inductor with inductance L_2, and coil-liner system with inductance L_{sys} and resistance R_{sys}; and Section 3 is defined to be the section containing Crowbar switch $S_{Crowbar}$, resistance with resistance R_3, and crowbar inductor with inductance L_3. In the 1D liner code, Current 1 (I_1) and Current 2 (I_2) are defined to be positive in clockwise flow direction as shown in Fig. A1. Current 3 (I_3) is defined to be positive when flowing upward as shown in Fig. A1.

If the circuit configuration is set to ringing case or if the crowbar switch is still open for two crowbar case, the 1D liner code solves following equations for currents and capacitor voltage.

$$I_1^n = \frac{C\ dt\ V_{cap}^{n-1} + C\ I_1^{n-1}\left(L_1 + L_2 + L_{sys}^{n-1}\right)}{(dt)^2 + C\ dt\left(R_1 + R_2 + R_{sys}^{n-1}\right) + C\left(L_1 + L_2 + 2L_{sys}^{n-1} - L_{sys}^{n-2}\right)}$$

$$V_{cap}^n = V_{cap}^{n-1} - \frac{1}{C}\ dt\ I_1^n$$

$$I_1^n = I_2^n\ ;\ I_3^n = 0$$

where V_{cap} is the capacitor bank voltage and dt is time step. Note that superscript is used in the equations to denote the index of the variable. To avoid confusion with exponentials, parentheses are placed around the variable to clarify the case when the superscript is used to denote exponentials. This notation convention is used throughout this section to avoid clutter and shorten the equation.

For the two crowbar cases, once the crowbar switch closes, the 1D liner code solves following equations for currents and capacitor voltage.

$$a_1 = -(C\ R_3\ dt + C\ L_3)$$

$$b_1 = C\ dt\left(R_2 + R_3 + R_{sys}^{n-1}\right) + C\left(L_2 + L_3 + 2L_{sys}^{n-1} - L_{sys}^{n-2}\right)$$

$$c_1 = C\left(L_2 + L_3 + L_{sys}^{n-1}\right) I_2^{n-1} - C\ L_3\ I_1^{n-1}$$

$$a_2 = (dt)^2 + C\ dt\ R_1 + C\ (L_1)$$

$$b_2 = C\ dt\left(R_2 + R_{sys}^{n-1}\right) + C\left(L_2 + 2L_{sys}^{n-1} - L_{sys}^{n-2}\right)$$

$$c_2 = C\ dt\ V_{cap}^{n-1} + C\ L_1\ I_1^{n-1} + C\left(L_2 + L_{sys}^{n-1}\right) I_2^{n-1}$$

$$I_1^n = \frac{b_2\ c_1 - b_1\ c_2}{a_1\ b_2 - a_2\ b_1}$$

$$I_2^n = \frac{a_1\ c_2 - a_2\ c_1}{a_1\ b_2 - a_2\ b_1}$$

$$I_3^n = I_2^n - I_1^n$$

$$V_{cap}^{n} = V_{cap}^{n-1} - \frac{1}{C}\, dt\, I_1^n$$

In the Circuit calculation, only the coil-liner system inductance and resistance is assumed to be function of time and contains time dependent dynamic term appear in the circuit equation. In the equation, Coil-liner system resistance (R_{sys}) is assumed to account not just the static resistance term, but also any other energy loss or conversion mechanism inside the coil-liner system that is not captured in the static resistance term (such as kinetic energy and thermal loss of the liner). Ohmic energy loss as well as dynamic inductive energy is also calculated in this step as

$$E_{Ohm}^{n} = E_{Ohm}^{n-1} + Rdt(I^n)^2$$

$$E_{deltaL}^{n} = E_{deltaL}^{n-1} + \frac{1}{2}(I_2^n)^2\left(L_{sys}^{n-1} - L_{sys}^{n-2}\right)$$

where $E_{Ohm}$is Ohmic Energy loss and E_{deltaL} is dynamic inductance energy of the coil-liner system.

Coil-Liner System Calculation:

In this step Coil-Liner system is treated as an independent system with external current (power) input to calculate the dynamic change in the coil-liner system due to the external input. There are six sub-steps in this step: static liner field calculation, static breed-through calculation, liner thermal calculation, liner dynamic calculation, circuit and geometric parameter calculation, and B-field correction due to dynamic effects.

Static Liner Field Calculation:

In this sub-step, a static liner magnetic field and flux calculation is conducted to calculate the change in the magnetic field and flux in the outer region due to the change in the current through the coil which was computed in the global circuit calculation. In this step, it is assumed that all flux change due to change in current ends up in the outer region of the coil-liner system. In the subsequent calculation, the 1D code assumes the symmetry of the problem and only looks at the single turn of the two turn coil. The net flux that results in the single turn of the coil (Φ_{net}) depends on the coil circuit configuration and is computed from the equation:

$$\Phi_{net}^{n} = \gamma L_{sys}^{n-1} I_2^n$$

where γ is 1 for parallel configuration, 0.5 for series configuration, and 2 for half-turn configuration. From the computed net flux through the single turn of the coil, a flux in the outer region and the magnetic field strength in the outer surface of the liner are computed as:

$$\Phi_{out,temp} = \Phi_{out}^{n-1} + \Phi_{net}^{n} - \Phi_{net}^{n-1}$$

$$B_{out,temp} = \Phi_{out,temp} C_A^{n-1}$$

where $\Phi_{out,temp}$ and $B_{out,temp}$ are temporally variable for flux and magnetic field in the outer region that is fed into the static bread through calculation.

Static Breed-through Calculation:

In this sub-step, magnetic field breed-through in the liner boundary is computed. In the 1D liner code, a diffusive magnetic field process is used to model the magnetic field breed-through across the liner. From diffusive model, it is assumed that the magnetic fields on the boundary of the liner obey the relationship:

$$B(t) = B_0 e^{-t/\tau}$$

where $\tau = \frac{L_{Liner}}{R_{Liner}}$ is the characteristic diffusion time scale, L_{Liner} is the inductance of the liner, R_{Liner} is the resistance of the liner, and B_0 is the initial magnetic field at the reference time.

Since for the breed-through across the liner boundary, gradient in the magnetic field is what drives the diffusive process, using the diffusive model and taking the time derivative, the magnetic field breed-through can be characterized as

$$\Delta B_{bt} = \frac{dt}{\tau} \left| B_{in}^{n-1} - B_{out,temp} \right|$$

where ΔB_{bt} is breed-through magnetic field. For the breed-through calculation across the inner and outer region, a liner can be considered as an infinitesimally thin boundary separating the contact surface of the two regions. Under this assumption, any change in magnetic field in the

inner region will show up in the outer region and vice versa. However, since it is know that magnetic field at the boundary of the liner does not increase or decrease locally in isolated manner, due to magnetic field diffusion in its respective region, flux based approach is used to relate local change in magnetic field to global change in the two regions. To model this, breed-through flux is calculated based on breed-through magnetic field from the diffusion model. Since net flux is conserved, any gain or loss of flux in one region must be compensated by gain or loss of flux in second region. Using the Field-Flux parameter, breed-through flux ($\Delta\Phi_{bt}$) is computed to be:

$$\Delta\Phi_{bt} = \Delta B_{bt}/C_A^{n-1}$$

if the magnetic field on the outer surface is greater than the inner surface, and

$$\Delta\Phi_{bt} = \Delta B_{bt}/C_B^{n-1}$$

if the magnetic field on the inner surface is greater than the outer surface. The final flux in the two regions are calculated to be

$$\Phi_{out}^{n} = \Phi_{out,temp} \pm \Delta\Phi_{bt}$$

$$\Phi_{in}^{n} = \Phi_{in}^{n-1} \mp \Delta\Phi_{bt}$$

The sign in the two equations above is chosen from the assumption that breed-through flux is flowing from the region of higher magnetic field strength to the region of lower magnetic field strength. Finally, the new magnetic field strength at the outer and inner surface of the liner after the breed-through process is calculated to be

$$B_{out,temp} = \Phi_{out}^{n} C_A^{n-1}$$

$$B_{in,temp} = \Phi_{in}^{n} C_B^{n-1}$$

where $B_{out,temp}$ and $B_{in,temp}$ are temporally variable for the magnetic field in the two regions that is fed into the subsequent calculations.

Liner Thermal Calculation:

In this sub-step, the thermal heating of the liner due to joule heating from the induced current in the liner is calculated. In the 1D Liner Code, it is assumed that all of the current is carried uniformly in the inner surface of the liner with the current penetration of two skin depth. The thermal calculation is computed under assumption that heating occurs only in the region where the current is flowing. Conductive thermal transfer in the liner in the radial direction is neglected in the code, due to the fact that thermal diffusion time in the liner is negligible compared with the collapse time of the liner compression. Using the magnetic field boundary condition at the liner surface, the current in the liner inner surface (I_{liner}) is calculated to be

$$I_{liner}^{n} = \frac{w}{\mu_0}\left(B_{out,temp} - B_{in,temp}\right)$$

where w is the width of the single liner. The thermal energy increase in the liner due to the joule heating is calculated to be

$$\Delta U_{therm} = R_{liner}^{n-1}(I_{liner}^{n})^2 dt$$

Because the thermal energy increase in the liner equates to a loss mechanism from the total coil-liner system, the thermal energy increase is characterized in the global circuit system as a thermal resistance R_{therm}. A thermal resistance is defined to be

$$R_{therm}^{n} = \frac{2\Delta U_{therm}}{(I_2^n)^2 dt}$$

and constitutes part of the coil-liner system resistance used in the global circuit calculation.

To calculate the temperature change in the liner due to joule heating, heat capacity is used to compute the increase in the liner temperature due to joule heating. The liner temperature is calculated from the equation

$$T^n = T^{n-1} + \frac{\Delta U_{therm}}{c\, m}$$

where T is liner temperature, c is heat capacity, and m is the mass of the liner in the region where the current is flowing. Once the liner reaches melting or vaporizing temperature, then the thermal energy increase is assumed to go into latent energy, until the stored latent energy is

above the latent energy of fusion or vaporization, where the phase change is assumed to have completed and the temperature starts to increase again.

Liner Dynamic Calculation:

In this sub-step, the dynamics of liner compression is computed by using the magnetic field strength along the liner boundary to compute magnetic pressure and the net force on the liner as a result of magnetic pressure. The magnetic pressure is calculated based on the magnetic field strength computed in the static breed-through calculation sub-step and is calculated from the equation

$$p_{out}^{n} = \frac{\left(B_{out,temp}\right)^2}{2\mu_0}$$

$$p_{in}^{n} = \frac{\left(B_{in,temp}\right)^2}{2\mu_0}$$

where p_{out} and p_{in} are the magnetic pressure acting on the outer and inner surface of the liner respectively. The resulting net force on the liner (F) is then calculated by equation

$$F^n = 2\pi w(p_{out}^{n}\, r_{out}^{n-1} - p_{in}^{n}\, r_{in}^{n-1})$$

where r_{out} is liner outer radius and r_{in} is liner inner radius. The liner acceleration (a) and liner velocity (v) is calculated from Newton's Second Law:

$$a^n = F^n / m_0$$

$$v^n = v^{n-1} + a^n dt$$

where m_0 is total mass of the single liner. In the 1D Liner Code, the liner compression mechanism is assumed to conserve liner width and liner volume, with compression taking place uniformly in the axial and radial direction. Due to the fact increase in the liner velocity increases kinetic energy of the liner, the coil-liner system converts energy stored in the fields to the liner kinetic energy. Thus, from the global circuit standpoint, this increase in the kinetic energy

appears as an increased resistance in the coil liner system. Thus, kinetic resistance is defined to be

$$R_{KE}^{n} = \frac{m_0((v^n)^2 - (v^{n-1})^2)}{(I_2^n)^2 dt}$$

and constitutes part of the coil-liner system resistance used in the global circuit calculation.

Circuit and Geometric Parameter Calculation

In this sub-step, geometric and circuit parameter required for the calculation of the next time step is computed. From the dynamic calculation data, the inner and outer liner radius is computed using basic kinematic equation derived from Newton's Third Law. A fit function based on the externally derived data for Inductance and Field-Flux parameter is used to compute Coil-Liner system inductance, liner inductance, Field-Flux parameter for inner region, and Field-Flux parameter for the outer region for the current liner geometry. The resistivity fit function is used to compute the resistivity of the liner from the current liner temperature. A coil-liner system resistance is computed to be

$$R_{sys}^{n} = R_{coil} + R_{therm}^{n} + R_{KE}^{n}$$

The liner resistance is computed based on the current liner resistivity (η_{liner}) from equation

$$R_{liner}^{n} = \frac{\pi \eta_{liner}^{n} (r_{in}^{n} + \delta)}{w\delta}$$

where $\delta = \sqrt{\eta_{liner}^{n} / (\pi f \mu_0 \mu_r)}$ is the skin depth distance based on the circuit frequency f.circuit frequency is calculated after the reversal of magnetic field gradient across outer and inner liner surface. If the skin depth is larger than the liner thickness or if the magnetic field gradient has not reversed, then the current liner thickness is used instead.

B-field Dynamic Correction

In this final sub-step, the magnetic field strength on the inner and outer liner surface is re-calculated due to the change in the liner geometry due to dynamic liner compression. Using the new liner geometry, Field-Flux parameter and the inner and outer flux value is used to compute

the final magnetic field strength in the outer and the inner liner radius (B_{out}^{n} and B_{in}^{n}, respectively).

Lagrangian Time Step and Field Reversal Check:

In this step, Lagrangian time step condition and magnetic field gradient reversal is checked. After the corrected magnetic field strength is calculated, the change in inner magnetic field strength in the current time step is computed to check that it is below the user defined maximum allowed change in the inner magnetic field strength. The default maximum is set to be 0.1 T. If the code detects that the change in the inner magnetic field in the current time step is greater than the allowed maximum it decreases the time step by user defined refinement factor and reset the time step to resolve the same time step with refined time step. The default time step refinement factor is set to be 50%.

Once the Lagrangian time step condition is cleared, the code checks the reversal in the magnetic field gradient across the outer and inner liner surface. If the code detects that the magnetic field in the inner liner surface is greater than that of the outer liner surface, the code calculates characteristic circuit frequency of the compression. The characteristic frequency of the compression is defined to be

$$f = \frac{v^n}{r_{out}^n + r_{in}^n}$$

and is used for the calculation of the skin depth distance of the liner.

End Condition Check:

In this step, the 1D Liner Code checks for end condition to break the code from the loop. If the liner inner radius becomes less than 1 μm, then the liner is considered to have fully collapsed, and the code breaks. If the liner comes to a stop and reverses its direction, then the liner is considered to have bounced back, and the code breaks. If the liner reaches maximum allowed temperature, the analysis is terminated with an error. The maximum allowed temperature is defined in the code to be the maximum temperature at which the external resistivity data exists. If the code detects that the liner is above the vaporization temperature, the analysis is terminated with an error. If the code detects NaN in its parameter, then it also terminates with error. Until

the end condition is met, the code continues to the next step. Once the end condition is met, the code breaks from the loop and sends the computed result to the postprocess block.

Postprocess Block:

In the postprocess block, the energy calculation for the coil-liner compression is finished from the data outputted from the Loop Solver. The Run information and main output performance parameters are outputted to the Matlab® console and is recorded to a text file. The result from the Loop Solver is also plotted as a time history plot and is recorded as a Matlab® figure file. The code terminates once all of the time history plots are generated and saved.

REPORT DOCUMENTATION PAGE

Form Approved
OMB No. 0704-0188

1. REPORT DATE *(DD-MM-YYYY)*	2. REPORT TYPE	3. DATES COVERED *(From - To)*
08/06/2015	Final	9/10/2012 - 3/10/2015

4. TITLE AND SUBTITLE
The Fusion Driven Rocket: Nuclear Propulsion through Direct Conversion of Fusion Energy

5a. CONTRACT NUMBER

5b. GRANT NUMBER
NNX12AQ61G

5c. PROGRAM ELEMENT NUMBER

6. AUTHOR(S)
John Slough, Anthony Pancotti, and Akihisa Shimazu

5d. PROJECT NUMBER

5e. TASK NUMBER

5f. WORK UNIT NUMBER

7. PERFORMING ORGANIZATION NAME(S) AND ADDRESS(ES)
MSNW LLC
8551 154th Avenue NE
Redmond, WA 98052

8. PERFORMING ORGANIZATION REPORT NUMBER
FDR - Final

9. SPONSORING/MONITORING AGENCY NAME(S) AND ADDRESS(ES)
NASA/Headquarters
300 E Street Southwest
Washington, DC 20546

10. SPONSOR/MONITOR'S ACRONYM(S)
NASA HQ

11. SPONSOR/MONITOR'S REPORT NUMBER(S)

12. DISTRIBUTION/AVAILABILITY STATEMENT
A - Approved for Public Release

13. SUPPLEMENTARY NOTES
NA

14. ABSTRACT
This two year effort focused on achieving three key criteria for the Fusion Driven Rocket to move forward for technological development: (1) the physics of the FDR must be understood and validated, (2) the design and technology development for the FDR required for its implementation in space must be fully characterized, and (3) an in-depth analysis of the rocket design and spacecraft integration as well as mission architectures enabled by the FDR need to be performed. All criteria were successfully completed and the results are detailed in this report.

15. SUBJECT TERMS
Fusion Driven Rocket, plasma propulsion, rocket design, mission analysis

16. SECURITY CLASSIFICATION OF:			17. LIMITATION OF ABSTRACT	18. NUMBER OF PAGES	19a. NAME OF RESPONSIBLE PERSON
a. REPORT	b. ABSTRACT	c. THIS PAGE			John Slough
U	U	U	UU	115	19b. TELEPHONE NUMBER *(Include area code)* (525) 867-8900